Electronic structure and magnetism of selected materials

by Chiuzbăian Gheorghe Sorin

Thesis
presented to the
Department of Physics
Osnabrück University

Osnabrück
May, 2003

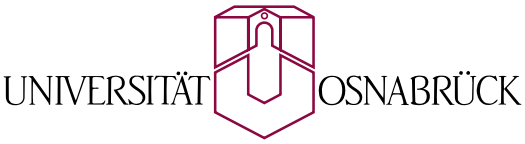

Thesis advisor:
apl. Prof. Dr. Manfred Neumann

Contents

Introduction **1**

1 Electron spectroscopies with X–ray excitation **5**
1.1 X-ray photoelectron spectroscopy 5
1.1.1 Physical principles of the technique 6
1.1.1.1 Theory of photoelectron spectroscopy 8
1.1.1.2 Photoelectron spectroscopy models 9
1.1.2 Data analysis 10
1.1.2.1 Valence band region 10
1.1.2.2 Core–level lines 11
1.1.2.3 Chemical shifts 12
1.1.2.4 Spin–orbit coupling 13
1.1.2.5 Satellites 14
1.1.2.6 Core–level line shapes 15
1.1.2.7 3s multiplet splitting 16
1.1.2.8 Secondary spectra (background) 19
1.1.2.9 Auger lines 20
1.1.3 Instrumentation 21
1.1.4 Quantitative analysis 24
1.2 X-ray absorption/emission spectroscopy 25
1.2.1 Physical principles 25
1.2.2 Theoretical aspects 26
1.2.3 Instrumentation 27

2 Molecular magnetism **29**

3 Transition metal dicyanamide compounds $M[N(CN)_2]_2$ with M = Mn, Fe, Ni, Cu **33**
3.1 Studies on the electronic structure 35
3.1.1 Specific experimental details 35
3.1.2 N and C 1s regions – Calibration 36
3.1.3 Transition metal core–level lines – Screening effects. 38
3.1.4 Modelling the transition metal 3s multiplet line 44
3.1.5 Valence band studies 49
3.2 Discussion on the electronic structure 54
3.3 Analysis of the magnetic superexchange interaction 60

3.4 Conclusions 69

4 Six–membered 'ferric wheel' molecule 71
4.1 Studies on the electronic structure 73
4.1.1 Sample and specific experimental details 73
4.1.2 XPS 1s core–level spectra of C, N and O Calibration 73
4.1.3 Iron XPS core–level lines 74
4.1.4 Valence band region 76
4.2 Computational results 77
4.3 Discussions 79
4.4 Conclusions 80

5 $LaNi_{5-x}Me_x$ (Me = Cu, Al) intermetallic compounds 81
5.1 State of the art 82
5.2 Samples details 83
5.3 Experimental and computational details 86
5.4 Experimental results 87
5.4.1 Magnetic data 87
5.4.2 XPS results 90
5.5 Computational results 95
5.6 Discussions 100
5.7 Conclusions 106

6 Conclusions and outlook 109

Acknowledgements 113

Bibliography 115

Curriculum Vitae 131

Introduction

The fine details of the relationship between the electronic structure and the magnetic properties of matter represent a state of the art challenge in the solid state physics. The link is evident even from a didactic approach: electrons are the 'carriers' of spin magnetic moments and their movement around nucleus gives rise to orbital momentum i.e. orbital contribution to the magnetic moments. From a more sophisticated point of view, the information on the electronic structure turns up to be essential for the understanding of magnetic behavior. Several comprehensive instances can be mentioned. The magnitude of Pauli–type paramagnetic susceptibility is given by the electronic density of states at the Fermi level. In transition metal insulators the interaction between the spin–moments on 3d ions are possible through the superexchange pathes given by the non–magnetic orbitals of the ligand atoms. The electrons in conduction bands act as 'mediator' of magnetic interaction between the 4f magnetic moments in the rare–earth intermetallics: the conduction electrons are polarized by the rare–earth moments and their states are essential for this kind of interaction.

These are two general ways to extract information about the electronic structure: the experimental and the computational approaches. In principle one should get access to the same aspects regardless of the nature of investigation but the collected data are usually complementary. Experimental spectral features may be understood with computational aid as well as experiments have the power to resolve the correctness of electronic structure calculations. Hence it is obvious that joint experimental–theoretical studies are actually always desirable.

From a magnetic point of view the solids can be generally divided in two categories. The first includes the materials which do not exhibit any spontaneous magnetization in the absence of an external field. These are generally the diamagnets, the materials with completely filled electronic shells and the Pauli paramagnets. The second group is characterized by the spontaneous alignment of the magnetic moments. These are the ferromagnets, the antiferromagnetic and ferrimagnetic materials and so forth. All these compounds posses a common feature: they include atoms with partially filled d or f shells.

In this thesis the joint experimental and theoretical studies on challenging materials belonging to both of the above mentioned groups are presented.

The molecule–based solids $M[N(CN)_2]_2$, where M is a transition metal, have insulating properties and are intriguing examples of metal–organic compounds. Among their interesting properties, the most attractive may be considered to be the ferro–antiferromagnetic crossover. Although the compounds are isostructural, the compositions with Mn and Fe reveal an parallel alignment of the magnetic moments,

while those with Co and Ni were shown to have antiferromagnetic properties. The 'magnetic relevant' information on the electronic structure rely on the exchange interactions orbitals interact and give rise to magnetic interaction patterns. The same aspects were focused when investigating the 'ferric–wheel' molecule Li $\subset$ Fe_6L_6Cl with L = $[N(CH_2CH_2O)_3]$. In contrast to the first mentioned materials the overall magnetic interaction does not resemble the whole solid but only the properties of a small cluster containing six Fe(III) ions.

The choice of these materials was supported by the increasing attention received nowadays by molecular magnets and, more generally, by metal–organic magnetic compounds. Beside their perspective for novel applications, the electronic structure and magnetism of these materials are a current challenge in spite of the progresses accomplished during the recent years.

The last class of materials presented in this work are the ternary $LaNi_{5-x}Me_x$ intermetallic compounds with Me = Cu, Al. They are derived from the well–known $LaNi_5$ parent compound. For these materials the focus on magnetic phenomena is moved towards the Fermi level. Moreover the band effects play a central role when dealing with their magnetic behavior. The selection of these materials was motivated by the partial lack of knowledge concerning their magnetic properties and by our expectations to support the conclusions draft on magnetism by the information on electronic states.

X–ray photoelectron spectroscopy was employed as main experimental method. For the study of the dicyanamide materials and of the 'ferric–wheel' the X–ray emission spectroscopy was used due to its unique power to resolve elemental contributions in the valence band region. Moreover the theoretical results on the electronic structure is listed and included in the final conclusions. For the intermetallic compounds magnetic measurements as well as a complementary theoretical description of the electronic structure are presented.

The thesis is structured as following:

- Chapter 1 introduces the reader in the details and features of the employed experimental techniques. This part is meant to give a rather complete but descriptive introduction to any experimentalist which is not familiarized with this kind of measurements. The cited references account for the state of the art development in this field and can serve as valuable further literature.

- In Chapter 2 the scientific beauty and appeal of the molecular magnetism is underlined. This field, although not a new one, is characterized nowadays by steady revival thanks to the recent developments. A brief historical development and outlook are also presented.

- An example of molecule–based solid is presented in Chapter 3. The presentation of this study focusing on transition metal dicyanamide compounds is divided into presentation and discussion of experimental results, comparison with theoretical calculations of the electronic properties, discussions on the electronic structure and the magnetic properties based on the achieved information. A particular attention was paid to the modelling of obtained results which means their presentation in a comprehensive simple model. This option is nowadays

almost a request since the field of molecular magnetism is an good example of interdisciplinary link between physics and chemistry i.e. the common language is an essential issue. Moreover, a simple but, so far as possible, complete model is a useful tool in the understanding of phenomena beyond the frontiers of specific studies.

- The experimental efforts focused on the understanding of magnetic behavior of a 'ferric–wheel' molecule are listed along with computational results in Chapter 4. It comprises of a presentation of experimental data followed by some conclusions gained from electronic structure calculations and finally discussions.

- In the last part (Chapter 5) the focus moves on a completely different class of materials but the central idea remains. The experimental results on the electronic structure are joint to the information on magnetic properties and theoretical calculations on the electronic structure. Finally, the link between magnetic properties and electronic structure is emphasized in the section dedicated to discussions. This part fully reflects the reliable output of a joint experiment–theory study of the electronic properties and magnetic behavior.

- The main conclusions of this work are summarized in Chapter 6.

Chapter 1

Electron spectroscopies with X–ray excitation

The experimental methods used in this work to investigate the electronic structure are reviewed in this chapter. The aim is to give a state of the art brief review on the employed techniques including theoretical and practical details. The issues which turned up to be relevant in the presented studies are emphasized.

1.1 X-ray photoelectron spectroscopy

Regarded today as a powerful surface spectroscopic technique, the *photoelectron spectroscopy* (PES) strikes its roots over more than a century ago. In 1887 W. Hallwachs and H. Hertz discovered the external photoelectric effect [1, 2] and in the following years refined experiments by J. J. Thomson led to the discovery of the electron, thus elucidating the nature of photo–emitted particles [3]. In 1905 A. Einstein postulated the quantum hypothesis for electromagnetic radiation[1] and explained the systematics involved in experimental results [4]. By the early sixties C. N. Berglund and W. E. Spiecer extended the theoretical approach and presented the first model of photoemission [5]. In the same period a group conducted by K. Siegbahn in Sweden reported substantially improvements on the energy resolution and sensitivity of so–called β–spectrometers. They used X–rays ($h\nu \simeq 1500$ eV) and managed to improve the determination of electron binding energies in atoms. Chemical shifts of about 1 eV became detectable [6–8]. The new technique was accordingly named *Electron Spectroscopy for Chemical Analysis*[2] (ESCA). The seventies marked the full recognition of technique's potential as a valuable tool for the surface analysis. Accurate data on the mean free path of the slow electrons were obtained and *ultra–high vacuum* (UHV) instruments became commercially available. More on the historical development of the photoelectron spectroscopy can be found in [9].

[1] A. Einstein was awarded with The Nobel Prize in Physics in 1921 "for his services to Theoretical Physics, and especially for his discovery of the law of the photoelectric effect" (see www.nobel.se for a full description).

[2] K. Siegbahn was awarded with The Nobel Prize in Physics in 1981 "for his contribution to the development of high–resolution electron spectroscopy" (see www.nobel.se).

1.1.1 Physical principles of the technique

A PES experiment is schematically presented in Figure 1.1. Incident photons are absorbed in a sample and their energy may be transferred to the electrons. If the energy of photons is high enough the sample may be excited above the ionization threshold which is accomplished by photoemission of electrons. Their kinetic energy is measured and the initial state energy of the electron before excitation can be traced back. Depending on the energy of incident radiation, the experimental techniques

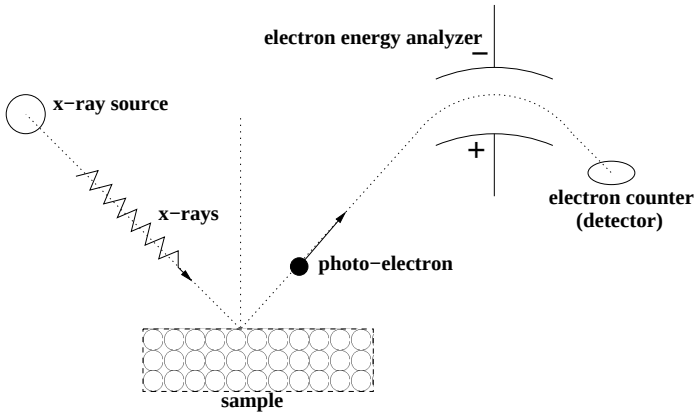

Figure 1.1: Schematically representation of a PES experiment.

are labelled as: *Ultra–Violet Photoelectron Spectroscopy* or UPS ($h\nu < 100$ eV), *Soft X–ray Photoelectron Spectroscopy* or SXPS (100 eV $<$ hν $<$ 1000 eV) and *X–ray Photoelectron Spectroscopy* or XPS ($h\nu > 1000$ *eV*).

In practical XPS, the most used incident X–rays are Al K_α (1486.6 eV) and Mg K_α (1253.6 eV). The photons have limited penetrating power in a solid on the order of 1–10 micrometers. However the escape depth of the emitted electrons is limited to some 50 Å. This characteristic makes XPS to an attractive surface science tool.

Accordingly to Einstein's theory of photoemission effect and taking into account the general case of electrons situated on different bounded levels, the kinetic energy E_{kin} of the ejected electrons is given by:

$$E_{kin} = h\nu - E_B - \Phi \tag{1.1}$$

with E_B the binding energy of the atomic orbital from which the electron originates and Φ the work function. The last term is a material specific parameter. The reference of the binding energy corresponds by definition to the Fermi level for solid samples. In case of gas phase studies zero binding energy is assigned to the vacuum level. For conductive materials the work function is dictated by the spectrometer as illustrated in Figure 1.2. Sample and spectrometer are connected in a close circuit so that the Fermi energies are at the same level. The spectrometer plays the role of an electron reservoir. Accordingly Φ must be replaced in Equation (1.1) by the work function of the spectrometer Φ_{spec} [10]. In most of the cases, Φ_{spec} is however unknown. This difficulty can be overcame by using a proper reference level.

In case of semiconducting and insulating samples, the assigning of the zero binding energy may be even more complicated and the calibration of zero binding energy

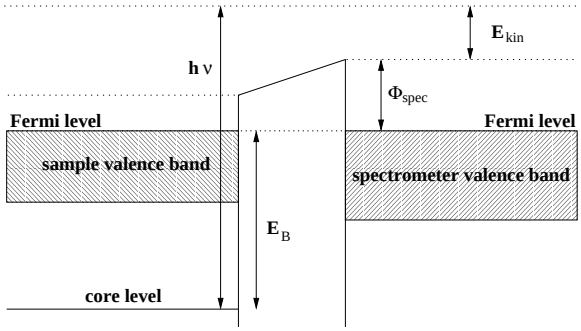

Figure 1.2: Energy level diagram for a XPS experiment with a conductive sample.

is performed with reference to some known line of an element in the sample with known valence state.

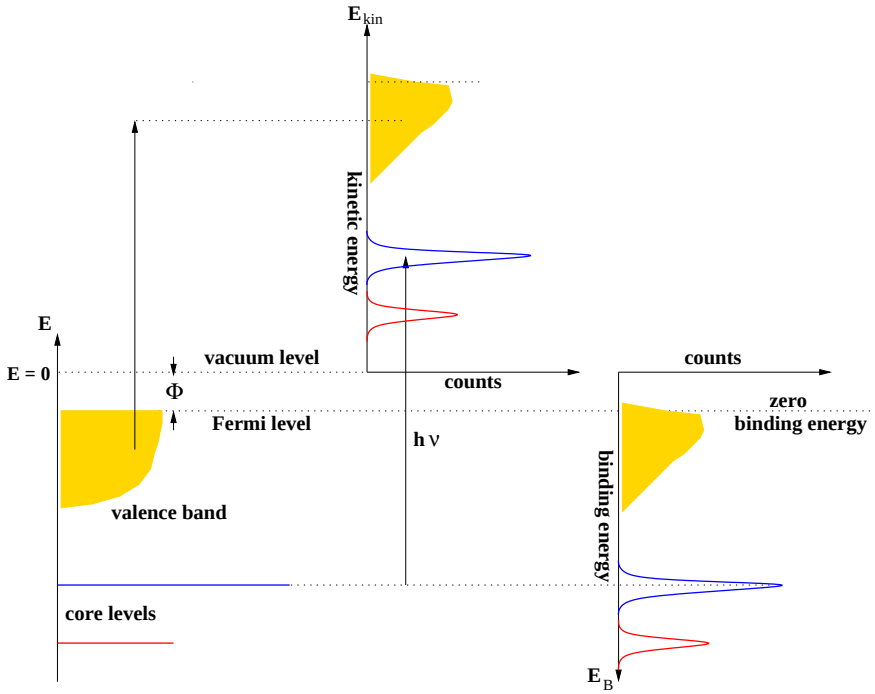

Figure 1.3: Schematic representation of energy levels in a solid (left) and the corresponding XPS spectra (center) having E_{kin} as natural abscissa. The right part illustrates the commonly used binding energy abscissa.

The XPS spectrum illustrates the number of electrons (recorded with the detector) versus their kinetic energy (measured by using the electron analyzer). For practical purposes it is generally preferred to use the binding energy as abscissa (as presented in Figure 1.3 after [11]). This is convenient since the kinetic energy depends on the energy of the incident radiation and the binding energies are alone material specific.

1.1.1.1 Theory of photoelectron spectroscopy

A rigorous theoretical description of the photoelectron spectroscopy implies a full quantum–mechanical approach. In this section important aspects underlying XPS are sketched focusing on the main approximations and models.

Let us consider a system containing N electrons which is described by the wave function $\Psi_{in}(N)$ and the energy $E_{in}(N)$. Absorption of a photon with the energy $h\nu$ causes the excitation into a final state described by $\Psi^k_{fin}(N)$ and $E^k_{fin}(N)$ [12]:

$$\overset{\text{initial state}}{\Psi_{in}(N);\ E_{in}(N)} \xrightarrow{h\nu} \overset{\text{final state}}{\Psi^k_{fin}(N);\ E^k_{fin}(N)} \tag{1.2}$$

where k labels the electron orbital from which the photoelectron has been removed. The transition probability (which dictates the photocurrent intensity) obeys the Fermi's golden rule [13]:

$$w = \frac{2\pi}{\hbar}|\langle\Psi_{in}(N)|\mathcal{H}|\Psi^k_{fin}(N)\rangle|^2\delta(E^k_{fin}(N) - E_{in}(N) - h\nu) \tag{1.3}$$

where the δ function ensures the energy conservation during transition and $\mathcal{H}$ is the interaction operator. The Equation 1.3 is satisfied when the perturbation $\mathcal{H}$ applied to the system is small. The interaction operator can be written as:

$$\mathcal{H} = \frac{e}{2m_e c}(\mathcal{A}\boldsymbol{p} + \boldsymbol{p}\mathcal{A}) - e\varphi + \frac{e^2}{2m_e c^2}\mathcal{A}\mathcal{A} \tag{1.4}$$

Here e and m_e denote the electron charge and mass, c is the light speed, $\mathcal{A}$ and φ are the vector potential operator and respectively the scalar potential of the exciting electromagnetic field and $\boldsymbol{p}$ is the momentum operator of the electron. A simplified form of the interaction hamiltonian can be obtained by assuming that the two–phonon processes can be neglected (the term $\mathcal{A}\mathcal{A}$), that the electromagnetic field can be described in the dipole approximation and choosing $\varphi = 0$ [14]:

$$\mathcal{H} = \frac{e}{m_e c}\mathcal{A}_0\boldsymbol{p} \tag{1.5}$$

where $\mathcal{A}_0$ is the constant amplitude of electromagnetic wave. The dipole approximation is valid if the radiation wave–length $\gg$ atomic distances, which is correct for the visible and ultraviolet regions of the electromagnetic spectrum. Mathematically the vector potential operator can be then written as $\mathcal{A}(\boldsymbol{r}, t) = \mathcal{A}_0 e^{(\boldsymbol{kr}-\omega t)}$. The approximation interaction hamiltonian for the structure of final state is more subtle [14, 15].

For high energy spectroscopy it can be assumed that the outgoing electron is emitted so fast that it is sufficiently weak coupled to the $(N-1)$ electron ion left behind. This is the so–called *sudden–approximation* which is actually valid in the keV region of energies. For lower energy regions its applicability has certain restrictions [16, 17]. The final state can be split up in two configurations:

$$\overset{\text{initial state}}{\Psi_{in}(N);\ E_{in}(N)} \xrightarrow{h\nu} \overset{\text{final state ion}}{\Psi^k_{fin}(N-1);\ E^k_{fin}(N-1)} + \overset{\text{photoelectron}}{\xi^k(1);\ E^k_{kin}} \tag{1.6}$$

where $\xi^k(1)$ is the wave function of the photoelectron.

The energy conservation during photoemission simply yields:

$$E_{in}(N) + h\nu = E^k_{fin}(N-1) + E^k_{kin} + \Phi \tag{1.7}$$

Here Φ is the work function. According to equation (1.1) the binding energy with respect to the Fermi level may be defined as:

$$E^k_B = E^k_{fin}(N-1) - E_{in}(N) \tag{1.8}$$

Koopmans assumed that the above binding energy difference can be calculated from Hartree–Fock wave functions for the initial as well as for the final state [18]. The binding energy is then given by the negative one–electron energy of the orbital from which the electron has been expelled by the photoemission process:

$$E^k_B \simeq -\varepsilon_k \tag{1.9}$$

This approach assumes that the remaining orbitals are the same in the final state as they were in the initial state (*frozen–orbital approximation*) and leaves out the fact that after the ejection of an electron the orbitals will readjust to the new situation in order to minimize the total energy. This is the intra–atomic relaxation. In fact the relaxation also has an extra-atomic part connected with the charge flow from the crystal to the ion where the hole was created. Therefore the binding energy is more accurately written as:

$$E^k_B \simeq -\varepsilon_k - \delta\varepsilon_{relax} \tag{1.10}$$

where $\delta\varepsilon_{relax}$ is a positive relaxation correction. A even more rigorous analysis must take into account relativistic and correlation effects which are neglected in the Hartree–Fock scheme. Usually both increase the electron binding energy.

1.1.1.2 Photoelectron spectroscopy models

Three–step model In frame of this model the complicated photoelectron process is broken up into three independent events [5]:

(I) absorption of a photon and photo–excitation of an electron as described above;

(II) transport of the electron to the surface;

Some of the photoelectrons reach the surface of the solid after suffering scattering processes, the dominant scattering mechanism being the electron–electron interaction. For low energies electron–phonon interaction dominates [19]. One of the most important parameter which describes these processes is the *inelastic mean free path* λ. It is defined as the mean distance between two successive inelastic impacts of the electron on its way through the crystal. Assuming that the mean free path λ is isotropic, several calculation were performed and an *universal dependence curve* of the mean free path was drawn [19–21].

More recent results based on Bethe's equation [22] came up with [23]:

$$\lambda(E) = \frac{E}{E^2_{plas}\beta ln(\gamma E)} \tag{1.11}$$

where λ will be deduced in (Å), E is the electron energy given in (eV), β and γ are parameters. E_{plas} is the plasmon energy of the free electron gas in (eV) and it can be calculated with $E_{plas} = 28.8\sqrt{N_\nu \rho / M}$ where N_ν is the number of valence electrons per molecule, ρ is the density and M is the molecular mass. An extended approach based on a modified Bethe equation delivers even better results [24–29]. For practical purposes the reduced formula $\lambda \propto E^p$, where p ranges from 0.6 to 0.8, can be used since it delivers reasonable results of the mean free path for electron energies in 100–1000 eV range [30].

(III) escape of the electron into vacuum;

The escaping electrons are those for which the component of the kinetic energy normal to the surface is enough to overcome the surface potential barrier. The other electrons are totally reflected back.

One–step model Apart from its didactic simplicity, the three–step model fails to offer a practical computational tool for the simulation of photoelectron lines. State of the art is the employing of one–step theoretical approaches in which the whole photoelectron process is regarded as a single one. The first of this kind was a compact and mathematically elegant solution to the previous three-step model [31] but was followed by fully dynamical [32] and relativistic one–step theories [14]. When specific crystal potentials are given as input data one–step models deliver theoretical simulations of the XPS spectra [33].

1.1.2 Data analysis

The recording of a wide scan is generally the first step in the sample characterization. The survey spectrum allows to identify the chemical components in the sample and to define acquisition windows. The lines of interest are afterwards recorded with higher resolution. An XPS spectra can be divided into:
–*primary spectrum*: given by electrons which leave the solid without inelastic scattering processes, and
–*secondary spectrum* or background: arising from photo–electrons which have already lost a percentage of their kinetic energy through inelastic scattering processes on the way to the surface.

1.1.2.1 Valence band region

Depending on the size of energy gap between valence and conduction band, solids are characterized at zero temperature as insulators and conductors [34]. XPS measures transitions between occupied (bounded) and empty (non–bounded) states. With *valence band* (VB) are denoted the occupied states within 0–20 eV binding energy. These states are of well–known importance for the properties of solids. In principle, it should be possible to determine the band structure of the solid via direct transitions (i.e. these occur without participation of other excitations). However, this is not generally the case. Still XPS is a very powerful tool in proving more knowledge about the occupied states in the valence band region.

The valence band spectrum resembles the one–electron density of states curve, but due to certain facts they are not identical: the spectrum represents the DOS distribution in an excited state, several screenings of the created hole (many–body effects), emission of electrons with different quantum numbers (i.e. different sub-shell cross–sections) or from different atomic species (i.e. different atomic cross–sections) as well as the instrumental broadening being responsible for further modifications.

One way to interpret the XPS VB spectra is the comparison with theoretical calculations of the densities of states (DOS). The recorded spectra can be simulated when such calculations are available and thus the contribution of each sub–shell can be described. Another alternative is to employ different excitations energies. The relative intensities of the various valence electrons peaks can drastically change when varying the energy of the used radiation because the relative photo–ionization cross sections change versus the incident photon energy. For example, by comparing the UPS and XPS valence band spectra of a M_xO oxide, one can get information about the partial contributions of the metal and oxygen states in the valence band. Another modern alternative is the interpretation of XPS VB in connection with other spectroscopic techniques like X–ray emission spectroscopy. In such joint VB studies certain features of the spectra can be directly assigned to the elemental components.

1.1.2.2 Core–level lines

Photoelectrons, which originate from core levels, give rise to the most intensive lines in the XPS spectra. The position of the core–level lines is like a fingerprint for each element and thus the chemical identification of the components in the investigated specimen can be easily performed. Generally two or more elements will be detected on the surface. The relative intensities of their lines is governed by: occupancy of the sub–shell, stoichiometry, atomic cross–section σ.

The values of σ can be derived from X–ray mass absorption coefficients or can be directly calculated [35–37]. The data used in this work were taken from reference [38]. Since the occupancy of the atomic sub–shells is known, XPS can be used as a non–destructive chemical analysis tool.

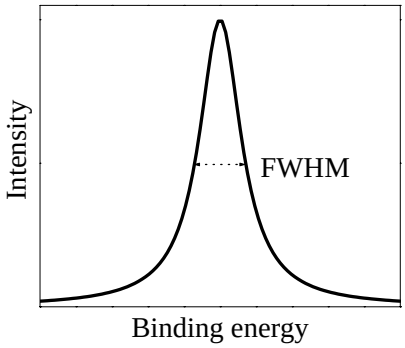

Figure 1.4: Illustration of a core–level line.

The peak width, defined as the full width at half maximum intensity (FWHM) (as represented in Figure 1.4), is a convolution of three distinct contributions [39]:

the natural inherent width of the core–level γ_n, the width of the photon source γ_p and the analyzer resolution γ_a. Thus the overall FWHM will be given by:

$$\gamma = \sqrt{\gamma_n^2 + \gamma_p^2 + \gamma_a^2} \tag{1.12}$$

The first contribution is dictated via uncertainty principle $\Delta E \Delta t \geq \hbar$ by the core–hole lifetimes τ:

$$\gamma_n = \frac{h}{\tau} \tag{1.13}$$

where h is the Planck constant. The lifetimes depend on the relaxation processes which follow the photoemission. The narrowest core–levels have lifetimes in the range $10^{-14} - 10^{-15}$ s whilst the broader have lifetimes close or slightly less than 10^{-15} s.

1.1.2.3 Chemical shifts

Shifts in the binding energy of peaks following changes of the chemical environment of the same atom are classified as *chemical shifts*. For example, there is a change in the binding energy of the Li 1s lines recorded for Li metal and LiO_2 (after [11]). In metal there is a screening of the 1s level given by the 2s conduction electrons (delocalized wave functions). Thus 1s electrons 'feel' in metal a somewhat weaker Couloumb interaction with the nucleus than that in oxide. Consequently the 1s electrons in LiO_2 are more bounded than in Li metal (see Figure 1.5).

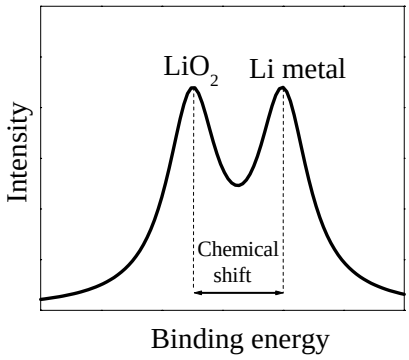

Figure 1.5: Qualitative representation of Li 1s line in LiO_2 and Li metal.

Since the value of chemical shift reaches the order of a few eV the oxidation state of each atom can be in principle traced back.

The value and direction of chemical shifts can be described using the so–called *charge–potential model* [40, 41]. The interactions between an inner electron on one atom, the nucleus and core electrons are considered as between point charges. The chemical shift relative to a reference state due to interaction with atoms within the first neighborhood ΔE_I is given by:

$$\Delta E_I \simeq l + k_i q_A + \sum_{B \neq A} \frac{q_B}{R_{AB}} \tag{1.14}$$

where k_i is a constant equal to the Coulumb repulsion integral between a core shell i and valence electrons, q_A is the charge of atom A and l is a constant determined by the reference level. k and l are regarded as adjustable parameters. The final term $\sum_{B \neq A} \frac{q_B}{R_{AB}}$ also called *Madelung–potential* sums the potential at atom A due to the surrounding atoms B. Besides its simplicity, the major advantage of the potential model is the possibility to use it to obtain atomic charges.

These considerations leave out the many–body effects i.e. relaxation effects. They are valid only when regarding the initial state[3]. The recorded chemical shift actually reflects the final state relaxation events [42]:

$$\Delta E \simeq \Delta E_I - \Delta E_R \tag{1.15}$$

where ΔE_R is a relaxation shift. Its value can be neglected under certain circumstances. In fact the above formulas are rather used to understand the chemical shift than to drop conclusions with respect to the valence state and chemical surrounding of atoms in a solid. This information is extracted by comparing the measurements with reference spectra which can be found in literature, even the efforts concerning a deeper theoretical description of the chemical shift have not been abandoned [43].

1.1.2.4 Spin–orbit coupling

In terms of a $j-j$ coupling scheme between angular and spin moments in an atom, for each orbital with nonzero angular quantum number l ($l > 0$), two energy levels are possible for electrons: the first with total quantum number $j = l + s$ and the second with $j = l - s$ (where s is the spin quantum number).

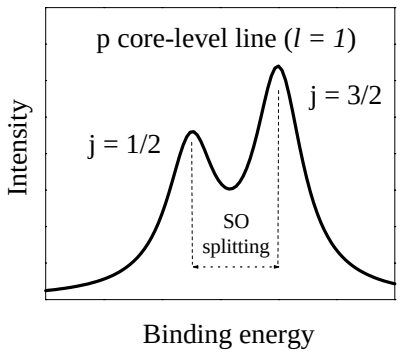

Figure 1.6: Schematically drawing of the spin–orbit (SO) splitting.

This spin–orbit splitting is present in XPS spectra, two peaks being observable, each for one j value (see Figure (1.16)). Taking into account that for a given j value there are $(2j+1)$ allowed states for electrons and that $s = 1/2$, the ratio of relative intensities can be easily calculated:

$$\frac{I_{j=l-s}}{I_{j=l+s}} = \frac{2(l-\frac{1}{2})+1}{2(l+\frac{1}{2})+1} = \frac{l}{l+1} \tag{1.16}$$

[3]This is the reason for the use of I in equation (1.14)

High–resolution core–level spectroscopy studies show small deviations from this branching–ratio due to different cross sections for the $j = l + s$ and $j = l - s$ lines and photo–diffraction effects.

1.1.2.5 Satellites

In the photoemission process the photon kicks out one electron so quickly that the remaining electrons do not have time to readjust. Thus the $(N-1)$ electron system is left in a non–relaxed state Ψ_{fin}. This excited state has a certain overlap with the stationary states Ψ_n and according to the sudden approximation we obtain the probabilities $< \Psi_n \mid \Psi_{fin} >$ to end up in Ψ_n states [44]. This means that the XPS spectrum consists from the *main line* (corresponding to the lowest excited state) and a number of extra lines (so–called *satellites*) representing the higher excited states after photoemission, as represented in Figure 1.7.

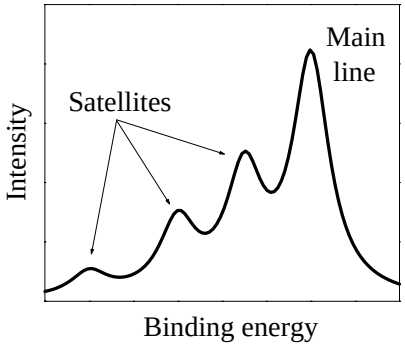

Figure 1.7: Illustration of a line with satellites.

In principle, there are two sources of satellites: an extrinsic part due to the *extra–atomic* events and an intrinsic part due to the *intra–atomic* relaxations.

For insulating compounds a reorganization of electronic structure in form of a charge transfer occurs after the creation of a core hole [45–50]. The corresponding features in the spectra are denoted as *charge transfer satellites*. They belong to the extrinsic category mentioned above.

The mechanism responsible for charge transfer in the final state is schematically represented in Figure (1.8) in case of a transition metal oxide and in terms of a molecular orbital description (after [51]). Due to the creation of a 3s core level hole, the Couloumb interaction pushes down the valence states in order to screen the hole. An electron will be transferred from ligand to metal valence states and thus the total energy of the $(N-1)$ electron system will be minimized. The donor ligand shell is 2p of O^{2-} in case of NiO or 3p of Cl^{-} for $CuCl_2$. The charge transfer will be then written as:

$$3s^2 3d^n L \longrightarrow 3s^1 3d^{n+1} \underline{L} \tag{1.17}$$

where n denotes the number of electrons in the 3d sub–shell, L is the ligand and by $\underline{L}$ is represented the loss of one electron on the ligand valence sub-shell.

In the particular case of the Cu 2p spectra of cooper dihalides, four lines are present in the spectra, namely: $2p_{3/2}3d^{10}\underline{L}$, $2p_{3/2}3d^{9}L$, $2p_{1/2}3d^{10}\underline{L}$, $2p_{1/2}3d^{9}L$. Each

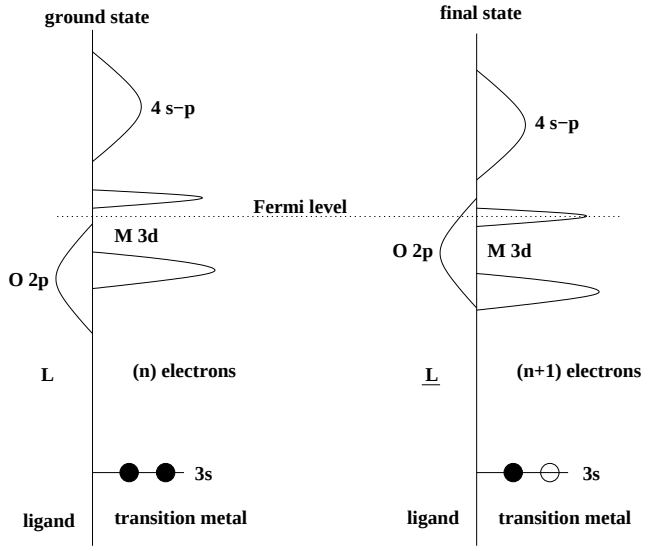

Figure 1.8: Charge transfer relaxation process in a transition metal oxide.

corresponds to a distinct final state of the $(N-1)$ electron system.

In the case of conducting samples the relaxation leads to quantified excitations in the conduction electron system, namely to creation of plasmons. Accordingly, the extrinsic features are denoted as *plasmon satellites*.

The reorganization of electronic structure after the creation of a core hole could also lead to a excess of energy which is not available to the primarily excited photoelectron. Thus two–electron processes can occur in case of conducting samples. The corresponding structures in the spectra are denoted as *shake satellites*. The hole appears to increase the nuclear charge and this perturbation is the cause of valence electrons reorganization. It may involve the excitation of one of them to a higher energy level. If an electron is excited to a higher bounded state then the corresponding satellite is called *shake–up satellite*. If the excitation occurs into free continuum states, leaving a double ionized atom with holes both in the core level and valence shell, the effect is denoted as a *shake-off satellite* from [52]). Discrete shake-off satellites are rarely discerned in the solid [39].

1.1.2.6 Core–level line shapes

In Equation 1.13 it was assumed that all the contributions to the final line are of the same shape i.e. they are described by the same function. This is actually not the case. The contributions due to photon source and analyzer are symmetric with respect to the maxima and can be relatively good described by a gaussian function:

$$f_G(\epsilon) = exp\left(-ln2\frac{4\epsilon^2}{\gamma_i^2}\right) \tag{1.18}$$

where $\epsilon = E - E_0$ is the distance relative to the maxima of the curve and $\gamma_i^2 = \gamma_p^2 + \gamma_a^2$ is the FWHM due to experimental setup.

The intrinsic part of the XPS peak due to the core–level life time is described by a Lorentz function:

$$f_L(\epsilon) = \left(1 + \frac{4\epsilon^2}{\gamma_n^2}\right)^{-1} \tag{1.19}$$

The overall line shape of core lines are obtained by convoluting the above two functions in a resulting so–called Voigt profile:

$$f(\epsilon) = f_L \otimes f_G = \int_{-\infty}^{+\infty} f_L(\epsilon') f_G(\epsilon - \epsilon') d\epsilon' \tag{1.20}$$

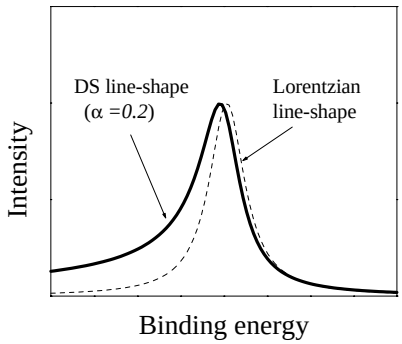

Figure 1.9: Comparison between a Doniach–Šunjić line shape and a Lorentz line shape. The shift of the maxima was artificially increased in order to point out its existence.

In case of conductive samples the intrinsic part of the XPS line is however more complicated than given in Equation 1.19. On the base of Mahan's hypothesis [53] and using calculations first carried out by Nozières and De Dominicis [54], Doniach and Šunjić [55] have shown that in metals the core level lines have a characteristic asymmetrical shape.

$$f_{DS}(\epsilon, \alpha) = \frac{\Gamma(1-\alpha)}{(\epsilon^2 + (\gamma_n/2)^2)^{(1-\alpha)/2}} \cos\left\{\frac{\pi\alpha}{2} + (1-\alpha)\arctan\left(\frac{2\epsilon}{\gamma_n}\right)\right\} \tag{1.21}$$

where Γ is the gamma function, $\Gamma(z) = \int_0^\infty t^{z-1}e^{-t}dt$, and α is an asymmetry parameter (see Figure 1.9). Its values can range between 0.1 and about 0.25 [56]. Hence for conducting samples $f_L(\epsilon)$ must be replaced in Equation 1.20 by $f_{DS}(\epsilon, \alpha)$. It is also worth to notice that in case of non–conducting samples the asymmetry factor is equal to zero and $f_{DS}(\epsilon, 0) = f_L(\epsilon)$. The asymmetry of the intrinsic XPS lines of conducting samples can be explained by taking into account the nonzero density of states at Fermi level.

1.1.2.7 3s multiplet splitting

The multiplet splitting of the 3s line for 3d transition metals with a local magnetic moment (i.e. unpaired electrons in the valence levels) was first observed about three

decades ago [57–60]. In the simplest model this splitting originates from the intra–atomic exchange coupling between the photo–hole and the unpaired 3d electrons in the final state of the system. As an example let us consider the case of the 3s level in a Mn^{2+} ion. Accordingly to Hund's rule for the ground state, the five 3d electrons are all unpaired and with parallel spins. A further unpaired electron is present on the core–level after ejection of a 3s electron. If the spin of this electron is parallel to that of the 3d electrons (high–spin final state HS with total spin $S + \frac{1}{2}$) then exchange interaction will result in a lower energy than for the case of anti-parallel spin configuration (low–spin final state LS, total spin $S - \frac{1}{2}$). The core–level line will be a doublet as illustrated in Figure 1.10.

According to *Van Vleck*'s theorem [61] the magnitude of the splitting ΔE will reflect the net spin in the valence band:

$$\Delta E = \frac{1}{2l+1}(2S+1)G^2(3s,3d) \tag{1.22}$$

with $G^2(3s,3d)$ the $3s-3d$ Slater exchange integral and $l=2$ the orbital quantum number. The intensity ratio for the two peaks is proportional in this model to the ratio of the angular momentum multiplicity:

$$\frac{I(S+\frac{1}{2})}{I(S-\frac{1}{2})} = \frac{2(S+\frac{1}{2})+1}{2(S-\frac{1}{2})+1} = \frac{S+1}{S} \tag{1.23}$$

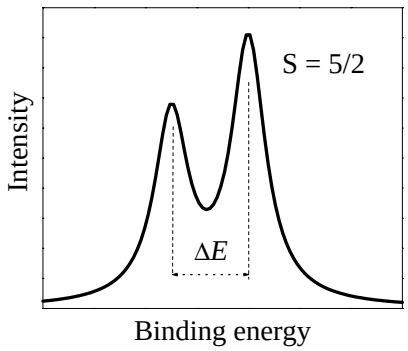

Figure 1.10: Illustration of a 3s multiplet splitting.

Even the above formulas suggests an "easy" diagnostic tool for local magnetic moments [62, 63], for 3d transition metal compounds the predicted separation[4] between the HS–LS doublet was found to be about two times larger than the observed one. An extensive collection of data on Fe 3s splitting revealed that for iron compounds the splitting and intensity ratio also do not directly reflect the local magnetic moment [64]. This findings revealed another key factor: *near–degeneracy* of the $3s^1 3p^6 3d^n$ and $3s^2 3p^4 3d^{n+1}$ configurations induces significant modification to the final states [65, 66]. This intra-atomic effect accounts for a reduction of the splitting by about a factor

[4]The calculations employed Hartree–Fock theory and were based on the one–electron approximation.

of two over the value given by exchange coupling only and mainly influences the low spin final states.

The above scheme works fine for transition metal ions with less than 6 d–electrons (like Mn^{2+}) but fails to describe the late transition metal compounds. This observation was explained by including an inter–atomic effect: the photo–hole is screened in the final state and a ligand to metal ion charge–transfer must be accounted. The exchange interaction is determined in a $3s^1 3d^{n+1}$ configuration rather than in the expected $3s^1 3d^n$ [67]. To what extend the screening effects should be regarded when interpreting a 3s multiplet splitting was the central point of several studies [68–72]. It was proposed that the 3s splitting reflect the local magnetic moment in the ground state only when charge–transfer satellites in the 2p core–level spectra is negligible. Spin–resolved photoemission studies allowed a better view on the magnitude of exchange–interaction effects [73–77]. State of the art in the theoretical treatment of the 3s multiplet splitting is the resolving of the proper Anderson hamiltonian in the impurity approximation [78, 79].

Nowadays there is a general agreement that three mechanisms govern the primary contribution to the 3s multiplet splitting in transition metals and their compounds:

Atomic effects (intra–atomic mechanisms):

1. Magnetic exchange splitting between the 3s and 3d shells

– Its contribution is given by Equations (1.22) and (1.23).

2. Configuration interaction (near–degeneracy) of the $3s^1 3p^6 3d^n$ and $3s^2 3p^4 3d^{n+1}$ final states configurations

– It reduces the HS–LS splitting by about a factor of 2 over the value given by Equations (1.22).

– It mainly influences the low–spin states.

– It accounts for the presence of the spectra structures at 20–30 eV towards the higher binding energy.

Solid–state effects (inter–atomic mechanisms):

3. Charge–transfer effects between the 3d metal ion and the ligand atom $3s^1 3d^n \rightarrow 3s^1 3d^{n+1}\underline{L}$ (where $\underline{L}$ represents a hole on the ligand)

– It is accounted by introducing a corresponding number of charge–transfer configurations both in the initial and the final state of the photoemission process. For example, the ground state will be written as a contribution from $|3s^2 d^n\rangle$ and $|3s^2 d^{n+1}\underline{L}\rangle$ states while the final state is given from both $|3s^1 d^n\rangle$ and $|3s^1 d^{n+1}\underline{L}\rangle$ states. With increasing atomic number of the 3d ion or decreasing electronegativity of the ligand, the energy requested for the $3d^n \rightarrow 3d^{n+1}\underline{L}$ electron transfer becomes smaller and this mechanism becomes more likely. In case of simple metal oxides, the charge transfer effects are dominating the NiO spectra whereas for MnO the screening effects are reduced by a relative high energy requested to overcome the charge transfer barrier. FeO and CoO represent intermediate cases where the interplay between exchange interaction and screening effects must be accounted.

The interpretation of 3s core–level spectra should be consistent with that of the 2p spectra. The 3s splitting is still a good measure of the local moment of the ground state only when the charge–transfer satellite in the 2p core level spectra is small.

1.1.2.8 Secondary spectra (background)

As previously mentioned, only the photoelectrons which travel to the surface without suffering inelastic scattering processes 'carry' direct information on the electronic structure. The others give rise to plasmon satellites (see previous section) or generate the background. In order to deliver quantitative information from the XPS spectra, the background subtraction must be performed. By all means, this is not a trivial problem. Shirley was the first to deal with this problem and he proposed a practical model [80]. However its results are in most of the cases unsatisfactory.

In a series of papers Tougaard *et al.* concentrated on this issue [81–86]. It was shown that for homogenous solids the proper photoelectron spectra $F(E)$ could be obtained from the measured spectra $j(E)$ by using:

$$F(E) = j(E) - \lambda(E) \int_{E}^{\infty} K(E, E' - E) j(E') dE' \tag{1.24}$$

where $K(E, E' - E)$ is a loss function which describes the probability of losing energy $T = E' - E$ during a mean free path travel for an electron with energy E. Obviously, the second term in Eq. (1.24) gives the background correction. A universal loss function $\lambda(E)K(E, T)$ which should describe all pure materials was proposed:

$$\lambda(E)K(E, T) = \frac{B(T)}{[C + T^2]^2} \tag{1.25}$$

where B and C are two constants. By comparison with experimental data, it was shown that the background correction for pure Ag, Au and Cu can be described using the following values: $B = 2866$ eV^2 and $C = 1643$ eV^2. In the case of alloys this universal loss function delivers a general good fit with experiment. Further validity test however indicated that from a rigorous point of view Tougaard's function must be regarded only as a good and improvable approximation [87–89]. The accuracy of the delivered results is however sufficient for the most of XPS spectra.

An accurate background can be obtained only from EELS (Electron Energy Loss Spectroscopy) experiments. In an EELS experiment electrons with kinetic energy E_0 are sent on the sample. A certain part of them will be reflected but the rest enter the surface and interact with the solid. Due to scattering processes the electrons lose energy E_0 and leave the solid with the kinetic energy $E_S = E_0 - E_L$. The outgoing electrons are energy resolved recorded [90]. In other words such an experiment simulates the kinetic energy loss of the XPS electrons.

1.1.2.9 Auger lines

After photo–emission the core hole will be filled with an electron decaying from a higher occupied level. This recovery of the atom from a higher energy state may be accomplished by the photo–ejection of another electron (see Figure 1.11). This two–electron process takes place on a 10^{-14} seconds time scala and is known as an Auger process [91]. The kinetic energy of Auger electrons is independent from the energy of incident radiation in the first photo–emission process, being only dependent on the internal de–excitation of the atom. For this reason an Auger process is denoted like: (XYZ) where X labels the core–hole shell, Y stands for shell from which the electron decay starts and Z indicates the shell from where the Auger electron is emitted. With this convention the Auger process presented in Figure 1.11 is labelled as KL_IL_{III} and the kinetic energy of Auger electrons is approximatively given by :

$$E(\mathrm{KL_IL_{III}})_{kin} \simeq E(\mathrm{K}) - E(\mathrm{L_I}) - E(\mathrm{L_{III}}) - \Phi \tag{1.26}$$

In Equation (1.26) the changes suffered by all atomic levels after the creation of the first K hole as well as various succeeding relaxation effects were ignored.

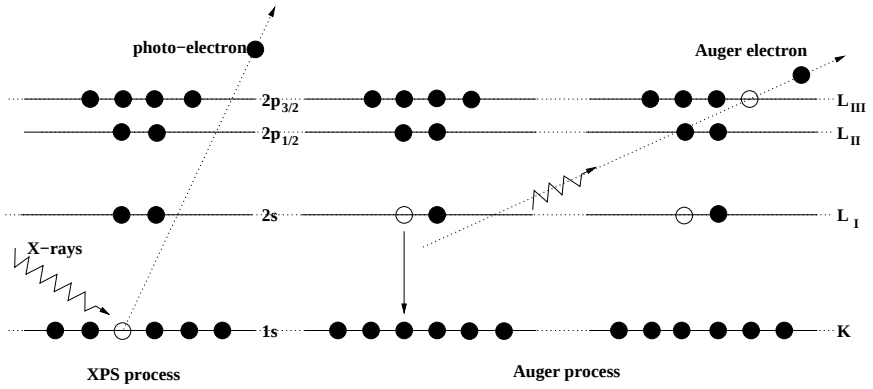

Figure 1.11: Example of an Auger process. The central and right part represent in fact a single process.

The Auger electrons are also detected and distinct lines are in the spectrum. The positions of these lines are catalogued along with the photoelectron peaks. One can discern on the nature of a Auger line by performing XPS measurements with two different incident radiation energies: $h\nu_1$ and $h\nu_2$. Since the binding abscissa is deduced by including the energy of incident radiation (see Eq. 1.1) the Auger lines will appear in the two XPS spectra at binding energy which will differ with $\mid h\nu_1 - h\nu_2 \mid$. The XPS lines will appear at the same binding energies independent of the energy of incident radiation

1.1.3 Instrumentation

All XPS experiments presented in this work were performed using a commercially available spectrometer PHI Model 5600 Multi–Technique System produced by the Perkin Elmer Corporation. Regarding the functional roles of its components the spectrometer is built up from: main and preparation chamber, 'quick–entry' system, electronic control units and a control computer. The measurements run in the main chamber, schematically represented in Figure 1.12, which is more or less just a more sophisticated version of Figure 1.1. The principal features of the main chamber components are listed and discussed.

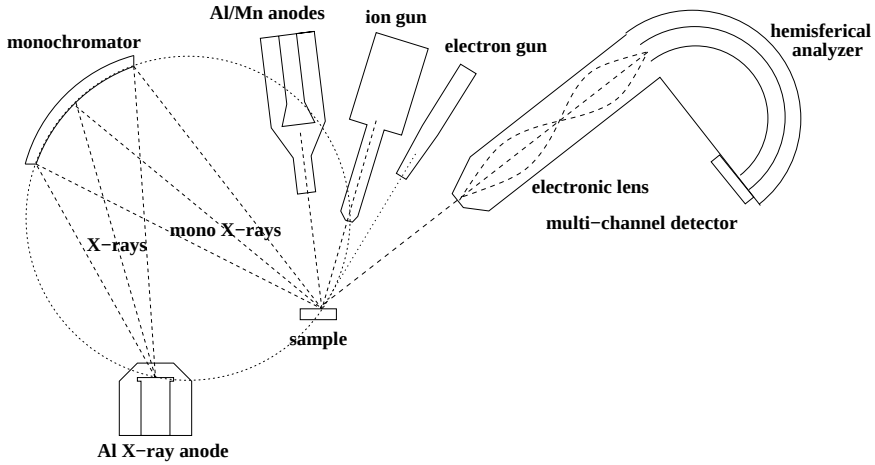

Figure 1.12: Scheme of the XPS spectrometer.

Vacuum conditions Ultra–high vacuum (UHV) conditions are requested when performing XPS measurements so that all components of the main chamber are kept under UHV during experiments. There are two important reasons to do so. The photoelectrons must reach the analyzer without being scattered by gas molecules and this is accomplished when the basic vacuum lies in the $10^{-5}-10^{-5}$ torr range. However under such a pressure the surface of the sample is quickly contaminated. Since XPS is very surface sensitive a base pressure of about 10^{-10} torr must be ensured in order to be able to perform measurements over several hours without taking care of the surface contamination. UHV conditions are reached by employing a combination of appropriate vacuum pumps: turbomolecular, sputter and sublimation pumps. In order to accelerate the rate at which gas molecules resident on the inner walls leave the main chamber the temperature of the whole system must be once increased to about $150°C - 150°C$ for several hours. This is the so–called back–out procedure. During the recording of the spectra presented in this work the base pressure in the main chamber was maintained in $5 \times 10^{-9} - 1 \times 10^{-10}$ torr region.

X–ray sources X–rays are produced by bombardment of an anode at high positive potential with electrons from a hot filament at earth potential (Bremsstrahlung). The spectrometer is equipped with Al anode for measurements with monochromatic

radiation and a dual Al/Mg anode. The characteristic energy of the anodes and their half–widths are: 1486.6 eV and 0.85 eV for Al K_α radiation as well as 1253.6 eV and 0.7 eV for Mg K_α radiation[5]. The dual Al/Mg anode is positioned in 'magic angle' of 54.7° to the analyzer. For this value the so-called 'orbital angular symmetry factor' $L = 1 + \beta(3\sin^2\theta/2 - 1)/2$, where β is a constant for a given sub–shell and X–ray photon and θ is the source–sample–analyzer angle, becomes equal to 1. It should be mentioned that L enters the final expression of line's intensity.

Monochromator The Al K_α characteristic radiation is filtered through a mono–chromator. Its function is based on the well–known Bragg diffraction relation: $n\lambda = 2d\sin\theta$ with λ the wavelength of X–rays, d the crystal spacing, θ the Bragg angle and n is the diffraction order. An accurate quartz crystal is used since for the first order diffraction of Al K_α radiation ($\lambda = 8.34$ Å) and $d = 4.255$ Å spacing of the (100) planes, the Bragg relation issues a convenient 23° Al anode–crystal–sample angle. The source, monochromator crystal and sample are placed on a 0.5 m Rowland circle. The monocromator reduces to about 0.3 eV the half–width and eliminates the satellites of characteristic Al K_α radiation, focalizes the radiation to a spot of 0.9 mm on the sample due to its toroidal shape, improves the signal–to–background ratio but reduces the intensity due to power dissipated in the diffraction. All the XPS spectra listed in this work were recorded using monochromatic radiation from an Al anode with 12 kV accelerating potential and 250 W power in the working regime. The crystal–sample–analyzer angle is fixed to 90°.

Analyzer The kinetic energy of the photo–electrons is filtered using an 11 inches hemispherical condenser. It consists of two concentrically assembled hemispheres of inner radii R_1 and outer radii R_2, a deflecting potential -V being applied between the two (see Figure 1.13). The median equipotential surface is ideally a hemisphere of radius $R_0 = (R_1+R_2)/2$ and the entrance and exit slits are centered on it. The photo–electrons are first focalized with an electronic lens system and enter then the analyzer through an entrance slit w which can be set to 4, 2, 0.5 or 0.15 mm. Additionally, in order to ensure a constant absolute resolution over the whole energy range, the kinetic energies are usually retarded to a given pass–energy E_p [92]. It must be mentioned that a low pass–energy implies both a improvement of the resolving power as well as a reduction of the source volume i.e. a lower overall intensity of the XPS signal. When recording XPS spectra the "constant analyzer transmission" (CAT) mode is used, which means that only electrons with the energy $E_p \pm \Delta E$ may travel in the analyzer (with ΔE is denoted the absolute energy resolution). The relative resolution of analyzer is then given by the approximate expression [92]:

$$\frac{\Delta E}{E_0} = \frac{w}{2R_0} + \frac{\alpha^2}{4} \tag{1.27}$$

where E_0 is the kinetic energy of the peak position and α is the entrance angle (see Figure 1.13). Since it is desirable to work with large entrance angles it is used to

[5] K_α indicates that the radiation is due to the decay of an L electron in a hole situated on the K shell.

choose α in such a way that $\alpha^2 \approx w/2R_0$ and Eq. 1.28 becomes:

$$\frac{\Delta E}{E_0} \approx 0.63\frac{w}{R_0} \tag{1.28}$$

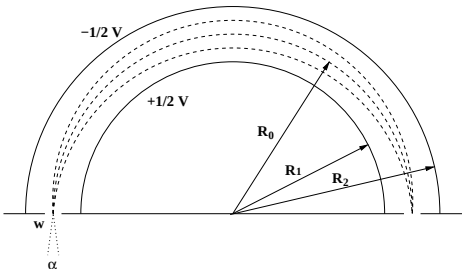

Figure 1.13: Scheme of the Concentric Hemispherical Analyzer (CHA).

For a $R_0 = 11$ inches analyzer and a $w = 2$ mm entrance slit, the absolute resolution of the analyzer is about 0.45% of the pass energy since in the CAT mode E_0 corresponds to the pass–energy.

For the detection of the electrons a multi channel detector with 16 channel plates is employed.

Ion gun When sputter–etching of the samples is desired, a ion gun with argon can be used. The ions can be accelerated to 4.5 kV maximal potential with a 3 μA available ion–current over a 10 mm $\times$ 10 mm scannable surface and a 100 μm focus. However due to the know–how available in our group, the sputtering was not used. The reason for this is the fact that even low accelerating potentials may induce drastic changes in surface geometry and/or stoichiometry [93].

Electron gun The spectrometer can be used to perform EELS measurements and is thus equipped with an electron gun. Its features are: 50 V – 10 kV accelerating potential at a 5–8 nA sample current and 0.25 eV half–width of the signal. The electron gun was not used in this work.

Neutralizer In case of insulating samples, superficial local charges can occur on the surface, leading to a serious perturbation of the measurement. To prevent this, a low–energy electron gun can be used to compensate the charging. The accelerating potential can be chosen between 0 and 10 V at a maximal current of 25 μA. The use of neutralizer is not at all trivial, both stable and low–width lines being aimed [94, 95].

As previously mentioned the spectrometer is also equipped with a preparation chamber. Its roles are to allow the introduction of the sample from normal atmospheric pressure in the main chamber, to cleave the solid samples in order to obtain non–contaminated surfaces, to prepare the samples by heat and/or gas atmospheres. In frame of this work the preparation chamber was used to cleave the samples in high–vacuum conditions, usually around $7 \cdot 10^{-8}$ torr. After cleaving the samples

were immediately moved into the main chamber. A quick–entry system is also available allowing a rapid, convenient and direct introduction of samples into the main chamber.

1.1.4 Quantitative analysis

Calculation of XPS intensities is based on the fact that the cross–sections of a core–level are independent with respect to the valence state of the element. By taking into account a spectrometer with a small entrance aperture and a uniformly illuminated sample [10], the intensity of the XPS line is given by:

$$I(E) = \underbrace{\sigma N \lambda(E) \cos(\phi) J L(\theta)}_{sample+geometry} \underbrace{H(E) D(E) T(E)}_{analyzer} \tag{1.29}$$

In Equation 1.29 σ is the cross–section of the level as already discussed in section 1.1.2.2 and $\lambda(E)$ is the escape-depth of photo–electrons as mentioned in section 1.1.1.1; J is the flux of primary photons on the surface and N is the density of atoms in the sample. ϕ denotes the angle between the surface normal and the direction of electron detection and θ is the source–sample–analyzer angle. $L(\theta)$ is the so–called orbital angular symmetry factor and is given by: $L(\theta) = 1+\beta(3\sin^2\theta/2-1)/2$, where β is a constant for a given sub–shell and X–ray photon.

This first part due to geometry of spectrometer and sample may intuitive be understood like: photons with a J flux illuminate the sample; the depth resolution in the sample is given by $\lambda(E)\cos(\phi)$, important being also the number of atoms in the detection volume (invoked by the density of atoms N) and their ionization probability σ.

The last three factors in Equation 1.29, usually denoted as the response function, are dictated by the analyzer. For modern spectrometers the factor describing the influence of analyzer fields on the number of registered electrons $H(E)$ has been more or less eliminated. $D(E)$ denotes the detector efficiency or ratio between the electrons exiting the analyzer and counts recorded by computer; it is in fact the response of the electron multiplier and channel plate detector. $T(E)$ is the spectrometer transmission function. Its values are specific for each machine and usually belong to the "producer secrets" i.e. it is not made public. Just a few years ago at the National Physical Laboratory in United Kingdom a "metrology spectrometer" was developed allowing determination of response function by employing true specific reference spectra [96].

It is a normal procedure to eliminate the proportionalities in Eq. 1.29 by referencing all the quantification on a relative basis i.e. by choosing one particular peak and referring all the measurements to it. For the core–level line of an element A and the reference line of element X recorded under similar conditions:

$$\frac{I(E_A)}{I(E_X)} = \frac{\sigma(h\nu, A) N_A \lambda(E_A) L(\theta, A) T(E_A)}{\sigma(h\nu, X) N_X \lambda(E_X) L(\theta, X) T(E_X)} \tag{1.30}$$

with $D(E_A)/D(E_X) = 1$ since the lines are supposed to have been recorded in CAT mode i.e. constant pass–energy. Usually fluorine 1s line is used as reference. Eq. 1.30 may be rewritten as:

$$\frac{I(E_A)}{I(E_X)} = \frac{s_A}{s_X} \frac{N_A}{N_X} \tag{1.31}$$

where s_A and s_X are the sensitivity factors for elements A and X. The software delivered with the spectrometer already contains experimental sensitivity factors which allow the user the calculations of atomic concentrations [97]. However one should be careful when using experimental sensitivity factors since they do not include the dependence of experimental factors like entrance slit or pass energy.

1.2 X-ray absorption/emission spectroscopy

1.2.1 Physical principles

A deeper insight of the electronic structure can be achieved by employing absorbtion and/or emission spectroscopies. Depending on their energy, X–rays induce various processes when interacting with the matter. As illustrated in Figure 1.3 when the energy of the incident radiation is high enough, an electron will be photo–ejected from the sample. This is the 'photon in–electron out' process corresponding to XPS.

In case the energy of incident X–rays is decreased the interaction may result in absorption of a photon and excitation of an electron to a higher bounded unoccupied state (Figure 1.14). Moreover, using tunable synchrotron radiation one can induce desired absorptions i.e. from a given core–level on the first unoccupied states above the Fermi level; this is the principle of *X–ray Absorption Spectroscopy* (XAS). Since core–level energies are unique the absorption edges will appear at certain energies of incident X–rays thus making XAS a valuable element sensitive tool for the investigation of unoccupied states.

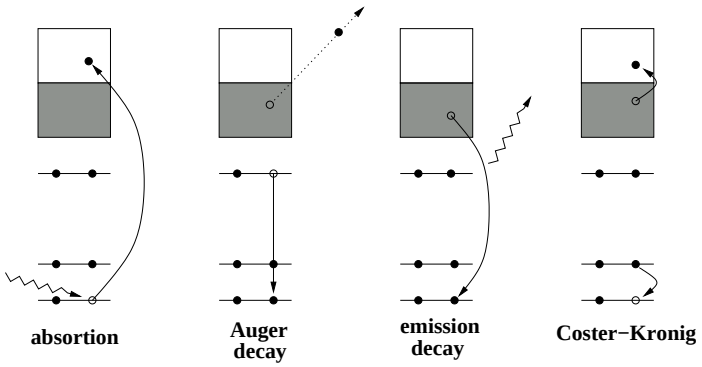

Figure 1.14: Interaction of X–rays with the matter.

After absorption the system will be left in an excited state with a core–hole and it can reach the ground stated on several channels. First, it is possible that an Auger process will take place (Figures 1.14 and 1.11) leading to the ejection of an electron. It is also possible that the photon generated in the core–hole filling step will leave the solid without suffering scattering processes i.e. fluorescence or emission processes and its energy can be recorded. By tuning the detector on the energy difference between the valence band and the core–level with a hole, only these decays will be recorded i.e. an element specific spectroscopy of the occupied states. Together with the excitation it is a 'photon in–photon out' method called *X–ray Emission Spectroscopy* (XES).

There is also a certain probability that the system will undergo the ground state through an intermediate step called *Coster–Kronig* transition (Figure 1.14).

There are certain remarks to be made with respect to XAS/XES. Since the penetration and escape depth of photons in a solid is on the order of 1000 Å, both spectroscopic methods probe such depths. This means that their surface sensitivity is reduced and one should carefully compare information obtained on this way with XPS results. Second, alike XPS, both XAS and XES are element sensitive, a powerful feature when investigating compounds. Third, one can employ XAS/XES without ultra high vacuum conditions since outgoing photons are not considerably scattered in gases and the surface sensitivity is reduced.

1.2.2 Theoretical aspects

As already mentioned, the absorption implies the excitation of a system in ground state Ψ_{in} to a final state Ψ_{fin} and the transition probability can be described analogue to an XPS process by the Fermi Golden Rule [98]:

$$w \propto \langle \Psi_{fin} | \widehat{er} | \Psi_{in} \rangle \delta(E_{fin} - E_{in} - h\nu) \tag{1.32}$$

where $(\widehat{er})$ is the dipole matrix elements coupling initial and final state. The final state can be described as the initial state with a core hole $(\underline{c})$ and a continuum electron on (ϵ): $\Psi_{fin} = \underline{c}\epsilon\Psi_{in}$ and thus the transition probability becomes:

$$w \propto \langle \Psi_{in}\underline{c}\epsilon | \widehat{er} | \Psi_{in} \rangle \delta(E_{fin} - E_{in} - h\nu) \tag{1.33}$$

Assuming that the matrix element can be rewritten as contributions from one–electron elements and removing all the electrons which are inactive in the transition, the series of δ functions resembles the density of states ρ.

$$w \propto |\langle \epsilon | \widehat{er} | c \rangle|^2 \cdot \rho \tag{1.34}$$

The intensity of XAS line is proportional to the transition probability. The dipole matrix elements dictate the following selection rules:

$$\Delta L = \pm 1 \ \Delta S = 0 \tag{1.35}$$

The probability for quadrupole transitions is about hundred times weaker so that they are generally neglected.

In case of XES the corresponding theory is even more complicated since the starting point of the emission process is an excited state [99, 100]. The variation of emission features versus energy of incident X–rays was reported thus giving rise to "branches" of emission spectroscopy: RXES or *Resonant X–ray Emission Spectroscopy* when the emitted photons have the energy around value of the incident radiation and NXES or *Normal X–ray Emission Spectroscopy* otherwise. The resonant response can be due to *Resonant Elastic X–ray Scattering* (REXS) or *Resonant Inelastic X–ray Scattering* (RIXS). The first (REXS) is due to a diffuse elastic scattering and the outgoing photons have exactly the energy of incident radiation. It is worth to notice that in the particular case of RIXS with conservation of the impulse, mapping of the band structure of some solids is possible.

The possible emission lines are presented in Figure 1.15, where the selection rules are given by the same dipole permitted transitions as in the case of absorption.

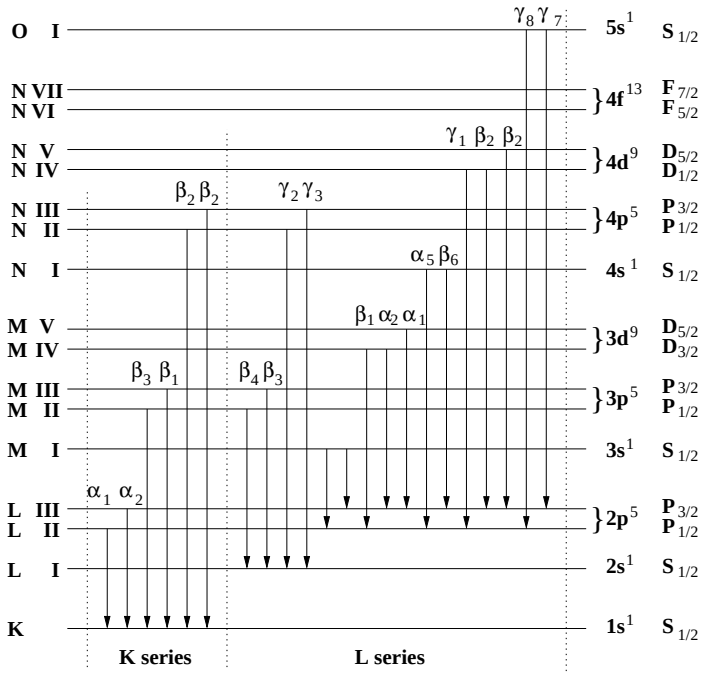

Figure 1.15: Possible emission transitions of the K and L series.

1.2.3 Instrumentation

The prerequisite for good XAS/XES results is a high brilliance and flux radiation source, which can be obtained only at modern synchrotrons. X–rays are generated when electrons travelling with velocities close to light speed, are forced to change the direction of their velocities. Bending magnets, wrigglers or undulators are placed at certain points of the synchrotron polygon, the so–called synchrotron ring. The most advanced radiation source is the undulator (Figure 1.16) which generates a periodic magnetic structure. The distance between magnetic poles and field strengths are chosen in a convenient way in order to generate coherent light at different bending stages which interferes with itself.

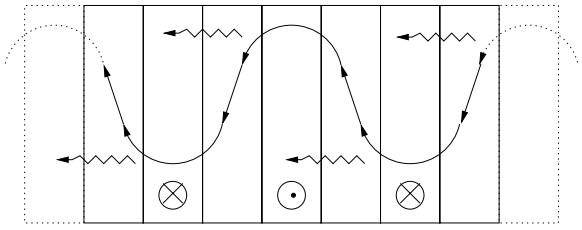

Figure 1.16: Principle of undulator.

All the XAS/XES results presented in this work were recorded at the Beamline 8.0.1 at Advanced Light Source. The beamline operates between 65 to 1400 eV at 1.5 GeV electron beam energy using the first, the third and the fifth order harmonic of 89 poles undulator with a 5.0 cm period. The generated radiation is then monochromatized with three interchangeable spherical gratings (Figure 1.17 after [101]). With

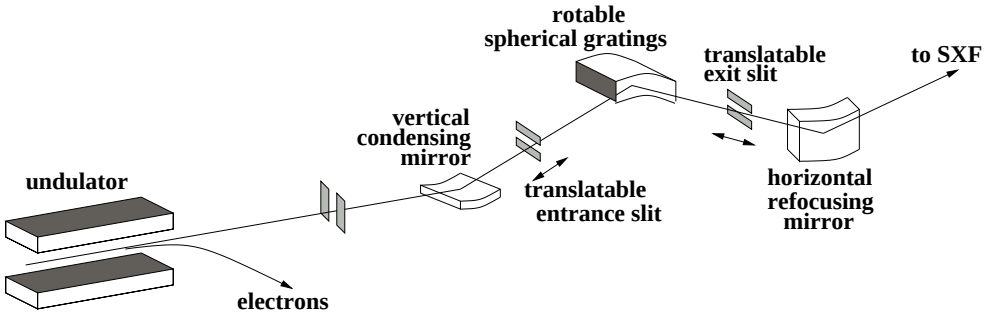

Figure 1.17: Layout of Beamline 8.0.1. at the Advanced Light Source in Berkeley

the entrance and exit slit of the monochromator chamber the spectral resolution can be selected. Spectral resolutions $E/\Delta E$ above 6000 at a $10^{12} - 10^{13}$ photons/s flux have been achieved.

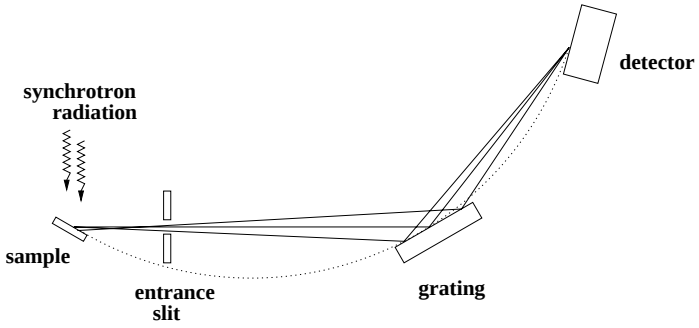

Figure 1.18: Scheme of the SXF endstation.

The *Soft X–ray Fluorescence* SXF endstation owned by the Tulane University and the University of Tennessee used for measurements is schematically presented in Figure 1.18 (after [102]) . It has a fixed (50– or 100 μm) entrance slit and the detection of fluorescence photons is performed in a Rowland geometry with four interchangeable gratings (600 and 1500 lines/mm and radii of 5 and 10 m). A multichannel plate are detector is employed as counter. The spectral resolution of the end station ranges between 400 and 1900 depending on grating and slit width.

Chapter 2

Molecular magnetism

Smaller and better is nowadays the core advertising slogan for almost all the new electronic products and the trend to miniaturization [103] is not only a scientific challenge but the key of financial survival for all companies on the market of electronic products. Small is both beautiful and practical. Nanotechnologies became synonym to the technological progress. The expectation that someday single molecules or molecular aggregates of nanometer dimensions will serve as active units of electronic circuits or bits for magnetic storage, is stronger than ever. Physics, chemistry and biology overlapped and got new interdisciplinary trends. So far the most successful branch seems to the molecular electronics [104] which can already report the widely spread liquid crystal displays or functional but not yet commercially available molecular contacts.

The trend to miniaturization has also risen a real interest of scientific community with respect to the molecular approach to the nanoscale magnetism, higher storage densities being the challenge in this field[1]. Thus, even the fundamental understanding of the magnetism has undergone wide progresses in the last decades the field is more actual than ever [105–108]. The main issue can be formulated relatively simple: molecules with a net total spin should play the role of magnetic domains and increase today's storage densities of 70 Gb/in^2 [109] (perspective 200 Gb/in^2 [110] or 300 Gb/in^2 [111]) to about 40 T/in^2 i.e. an increase of about 500 times. Even molecular materials are very promising over conventional metal–based magnets, fundamental problems are still to be solved.

One of the central problems is that of the magnetic interaction. The basic issue was to find feasible conditions in order to obtain metal–organic ferromagnets. This task was not an easy one. Usually 3d transition metal ions are employed as magnetic centers while diamagnetic organic radicals or atoms are used are magnetic bridges. In most of the molecules the magnetic exchange results from super–exchange interaction of the spins (magnetic ions) via diamagnetic ligands so that the antiferromagnetic interaction prevails. It drives the system into a zero total spin ground state. An important step forward was made in 1987 when the metal–organic compound

[1]One should note that the holograms are also treated as a perspective alternative to traditional storage media.

$Fe[(Me_5C_5)_2][TCNE]$, Me = methyl, TCNE = tetracynoethylen, was shown to exhibit magnetic hysteresis below 4.8 K [112, 113]. It was the first ferromagnetic metal–organic compound. A few years later the first pure organic ferromagnetic compound was synthesized [114]. But this field received a large impact since the polynuclear complexes $[Mn_{12}(CH_3COO)_{16}O_{12}(H_2O)_4] \cdot 2CH_3COOH \cdot 4H_2O$ were shown to exhibit magnetic hysteresis with a pure molecular origin (i.e. it is not the result of long–range magnetic interaction but a one extended to only a few atoms) [115, 116]. The magnetic coupling is negative but the manganese ions have different valences, thus resulting into a non–zero net spin molecule. Ever since the coordination chemistry has brought forth a whole new class of such synthesized magnetic molecules in which are embedded interacting magnetic ions [117]. Nowadays such magnetic molecules are denoted as nano–magnets. The core of these molecules, a cluster of magnetic ions, is surrounded by a large complex of nonmagnetic organic ligands which shields the cluster from the moments of neighboring molecules. The intermolecular interaction is negligible and measurements on a bulk sample only reflect the intramolecular magnetic coupling. All these remarkable progresses as well as the high expertise gathered with respect to the magnetic interactions of other metal–organic structures have brought a relevant contribution to the basic understanding of magnetism [118, 119].

There are several concrete aspects which make the molecular approach to the magnetism at the nanoscale to be very appealing.

- Unlike the conventional magnetic particles, the number of atoms and their arrangement (shape, size and orientation) in molecule is exactly the same so that accurate approaches of their properties can be carried out. Such clusters also serve as ideal spin systems for theoretical models.

- The intra–atomic magnetic interactions can be modified in a controlled way using the flexibility of the synthetic chemistry (ligand substitution or by variation of magnetic ion species determining the magnitude of the individual spins) [120, 121].

- Molecular magnets exhibit a number of unusual phenomena of scientific interest: pure quantum tunneling relaxation of the magnetization [122] or spin crossover transitions which can be optically switched (Light-Induced Excited Spin State Trapping or LIEEST) [123].

- Nano–sized molecular magnets are offering potential perspectives for future application in data storage, quantum computing [108] or display technology [124], in medicine [125] or biotechnology [126].

However several basic features are still responsible for the up to date lack of practical applications in the main interest field of magnetic storage media. One of the most important is the strength of magnetic coupling. Due to its low values ($J \approx 10$ K) room–temperature appliances are nowadays only expectations. Secondly, the tunneling of magnetization, even it is an attractive basic–research issue , implies stabilization difficulties of the molecules on a substrate [127]. Last but not least, even all these difficulties could be overcame, some other technological aspects like read and write heads for such small domains would still block the way to a rush development

of practical devices. Concluding, even the understanding of molecular magnetism has undergone a rapid progress, a significant work is still to be done in order to reach the level of practical applications.

Our approach to the above mentioned issues is the experimental study of the electronic structure by means of X–ray spectroscopic investigations. Together with joint theoretical studies this serves to elucidate the factors that govern the interaction between the spin carriers. Properties like overlap and orthogonality of the magnetic orbitals, spin delocalization and polarization effects are relevant. Alike in the case of magnetism of conventional materials, studies of the electronic and magnetic structure involving X–ray spectroscopic techniques could resolve a wide range of issues.

Chapter 3

Transition metal dicyanamide compounds $M[N(CN)_2]_2$ with M = Mn, Fe, Ni, Cu

Molecule–based solids with the general formula $M[N(CN)_2]_2$ (M = Mn, Fe, Ni, Co, Cu) have been subject of constant research efforts in the last decade, their appeal being motivated by several physical and chemical particularities. First synthesized in the late seventies for M = Ni [128], these compounds were later shown to be isostructural and to exhibit both overall ferromagnetic and antiferromagnetic coupling between the metal ions [129–138]. The transition metal (TM) ions with a general M^{2+} formal valence state are surrounded by $[N(CN)_2]_2^-$ dicyanamide groups. It was reported that the compounds having six or fewer 3d electrons (M = Mn, Fe) present a canted antiferromagnetic order at low temperatures while those with seven or more electrons on the 3d shell (M = Co, Ni) show a ferromagnetic interaction [129, 135]. The composition with copper behaves as a paramagnet [130]. The coercive field for $Fe[N(CN)_2]_2$ of 17800 Oe is the largest for any metal–organic compounds and even exceeds those of well known permanent magnet alloys like $SmCo_5$ or $Nd_2Fe_14B_2$ [129].

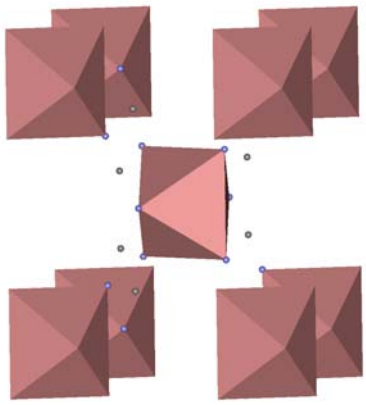

Figure 3.1: Crystallographic structure of $M[N(CN)_2]_2$ compounds. The MN_6 octahedral distorted units are emphasized.

Compound	$Mn[N(CN)_2]_2$	$Fe[N(CN)_2]_2$	$Co[N(CN)_2]_2$	$Ni[N(CN)_2]_2$	$Cu[N(CN)_2]_2$
Space group	*Pnnm*	*Pnnm*	*Pnnm*	*Pnnm*	*Pnnm*
Interatomic distances and angles at:					
	4.6 K	1.6 K	1.6 K	1.6 K	–
M–M	6.0657(1)	5.9670(1)	5.9158(1)	5.8634(1)	–
M–N(2)–C	119.2(1)	119.6(1)	120.6(1)	121.0(1)	–
N(2)–C–N(1)	175.2(3)	175.5(2)	175.1(2)	174.6(2)	–
C(2)–N(1)–M	158.5(2)	158.9(1)	159.6(1)	159.5(1)	–
α	140.4(1)	141.7(1)	142.3(1)	142.6(1)	–
M–N(1)	2.189(1)	2.126(1)	2.093(1)	2.053(1)	–
M–N(2)	2.291(2)	2.206(1)	2.156(2)	2.129(2)	–
Δ	1.047	1.038	1.030	1.037	–
β	25.2(2)	26.4(2)	27.5(2)	27.6(2)	–
Magnetic ordering type					
	canted AFM	canted AFM	collinear FM	collinear FM	para
	($2\phi \approx 10°$)				–
Ordering temperature					
	16 K	–	9 K	21 K	–
Local magnetic moments of 3d–ions					
	4.61 μ_B	4.23 μ_B	2.67 μ_B	2.21 μ_B	1.05 μ_B

Table 3.1: Reported crystallographic and magnetic data for $M[N(CN)_2]_2$, M = Mn, Fe, Ni, Co, Cu (from [135] and the references therein). Δ is given by $\Delta = [M - N(2)]/[M - N(1)]$ and describes the octahedral distortion. The nitrogen atoms situated on the distortion axis are labelled as N(2) while those in the equatorial plane of the rhombus–shaped units (see Figure 3.1) are denoted with N(1). β is the tilt angle of the equatorial plane of the MN_6 bipyramides with respect to the *ac* plane. α is the $M - C - M$ angle.

The crystallographic properties of these compounds are nowadays well characterized. Each metal ion is surrounded by six nitrogen atoms (see Figure 3.1) in a distorted (axially elongated) octahedral geometry. The rutile–like structure consists of rhombus–shaped units which adopt a chain alignment parallel to the *c* axis. The elongation axis of the bipyramides is contained in the *ab* plane. Two kinds of non–equivalent nitrogen atoms form the distorted octahedral surrounding of M^{2+} centers: four belong to the $-C \equiv N$ ends of the dicyanamide group while the other two are positioned on the elongation axis and represent the central nitrogen in $N \equiv C - N - C \equiv N$. The compound with Cu undergoes a Jahn–Teller effect and the Cu^{2+}–N (amide) distances are greater than the Cu^{2+}–N (nitrile) lengths [130]. Because of the tilting of the elongated octahedra in the crystallographic *ab* plane, two symmetry related M^{2+} ions can be distinguished in the unit cell (Figure 3.2), one positioned in the corner $(0, 0, 0)$ and the other in the center $(1/2, 1/2, 1/2)$.

Replacing of the metal ion induces changes of the magnetic and crystallographic properties i.e. bond distances and angles are changed (see Table 3.1 and [130]). Since the ion–ion distances range between about $5.8 - 6.1$ Å [135], direct magnetic exchange between magnetic moments can be utterly neglected and the magnetic interaction is due to organic superexchange pathways between metal ions. In other words there

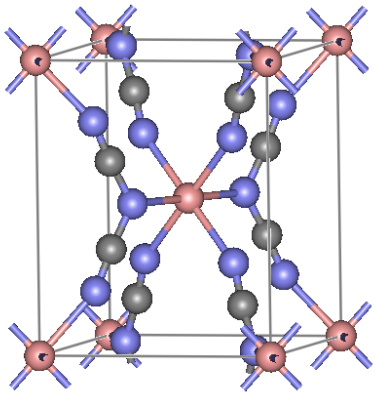

Figure 3.2: Unit cell of $M[N(CN)_2]_2$ compounds.

is an interplay between the magnetic features, nature of the transition metal ion and structural properties. The understanding of this relationship is essential for the design of metal–organic compounds with desired physical properties [139, 140]. The importance of this issue is underlined by the quite rare cases when ferromagnetic alignment occurs in metal–organic compounds. The key–details may get a consistent understanding with the study of this isostructural series owing both FM and AFM behaviors.

Any answer to the questions related to the factors which trigger the crossover from the canted AFM to the FM magnetic ordering must rely on consistent information of the electronic structure because both changes of magnetic and structural properties are reflected in the distribution of orbitals, changes in overlaps and other electronic properties.

The aim of this study is to go beyond the generic explanation of the magnetic exchange interactions, to investigate the electronic structure of these compounds and to employ the achieved information to describe magnetic interactions.

The spectroscopic investigations were performed on samples kindly supplied by Carmen R. Kmety[1] and their synthesis was described in the literature [131, 133–135, 137].

3.1 Studies on the electronic structure

3.1.1 Specific experimental details

For XPS investigations pellets of pressed poly–crystalline powder were cleaved in the preparation chamber under a basis pressure of about 5×10^{-7} mbar and then quickly moved into the main chamber. Due to the insulating character of the samples, charging on the surface was compensated during measurements by employing a low–energy electron gun. Its parameters (electron energy and flux) were chosen in a convenient way in order to ensure stable positions of the intensive core–level lines

[1] Actual address: Department of Physics, The Ohio State University, Columbus, Ohio 43210–1106, United States of America

(N 1s and C 1s) as well as a minimal full width at half minimum. Moreover since tiny changes of surface's quality may influence its overall conducting properties thus requesting slightly modified parameters for the neutralizer profile–like measurements were performed. This kind of spectra recording is also recommended since metal–organic compounds are far from being chemically as stable as conventional crystalline samples. The presented spectra resulted as a careful sum of partial sweeps. This procedure allows the exclusion of partial spectra in case some changes of the observed features were noticed and prevents the inclusion of information which may mislead the final interpretation. Survey spectra were recorded before, during and at the end of measurement cycles in order to achieve a steady check of surface quality. Generally no changes or artefact features were noticed during the measurements.

3.1.2 N and C 1s regions – Calibration

When dealing with XPS spectra of non–conducting samples, one common problem is the calibration. In the case of dicyanamide materials presented here the reference line was chosen to the N 1s line in the cyanide C≡N group. The existence of the triple bond between carbon and nitrogen atoms in the cyanide radical was experimentally evidenced by infrared spectroscopy [131].

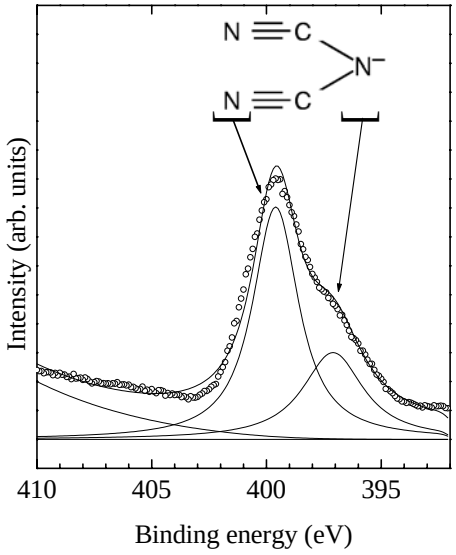

Figure 3.3: XPS 1s core–level line of nitrogen in $Ni[N(CN)_2]_2$. In the upper part the cyanamide ion is represented, indicating the two non–equivalent nitrogen positions.

The particular case of $Ni[N(CN)_2]_2$ is presented in Figure 3.3. A fit was performed by using Lorentz shapes for the peaks and a Tougaard–type form of the background. The Lorentz peaks were convoluted with a 0.6 eV Gauss line which accounts for the apparatus broadening. A 2 : 1 area ratio as indicated by the chemical formula was imposed as restrictive condition. The calibration was performed by assigning the N 1s line in the C≡N group to 399.57 eV [141]. The XPS line corresponding to the central nitrogen atom of the dicyanamide group is situated at lower binding energy as expected from its formal valence state.

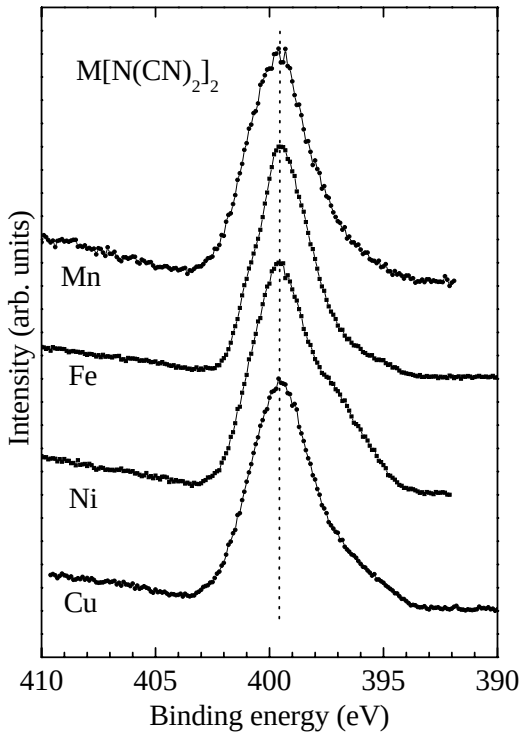

Figure 3.4: XPS 1s core–level lines of nitrogen in $M[N(CN)_2]_2$.

The N 1s lines for all the investigated compounds are presented in Figure 3.4. The experimental points were fitted using the procedure described above and generally only two peaks with having a 2 : 1 area ratio were enough in order to describe the spectra. Because of the strong overlap between the two component line, the deduced binding energy of the second intensive N 1s peak (397.3−398.0 eV) should be regarded only as a very good estimation.

The relatively high width of the presented lines may be explained by taking into account the nature of the investigated samples. One of the reasons is certainly related to their crystallinity: poly–crystalline samples usually issue wider XPS lines than monocrystals. Secondly the cleaved surface of poly–crystalline materials may be not flat enough in order to ensure an optimal charging compensation. This aspect is illustrated in Figure 3.5. XPS active regions of the surface where the low–energy electron beam is shadowed by irregularities could be responsible for low–intensity diffuse features situated at higher binding energy with respect to the main line. For $Fe[N(CN)_2]_2$ and $Mn[N(CN)_2]_2$ these structures converge and the result is a shoulder of the N 1s. Its presence however do not affect the analysis since the area of some additional third peak accounting for the shoulder is below 5% the sum of two material specific N peaks.

The above considerations suggest that both recording and analysis of XPS spectra in case of such compounds is far from being trivial. Specific experimental solutions as well as a flexible analysis are pre–requisites for a correct approach.

The XPS C 1s lines for all the investigated $M[N(CN)_2]_2$ materials are shown in Figure 3.6. Generally two peaks can be stood out in the spectra. The most intensive

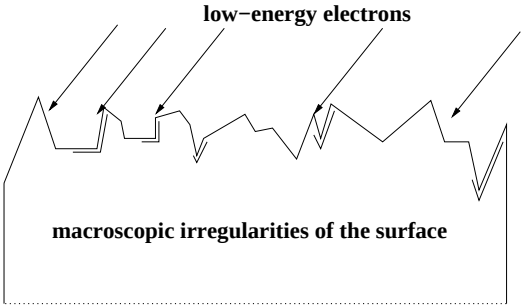

Figure 3.5: Partial charge compensation in case of XPS measurements on rough surfaces. The incident X–rays are in a plane perpendicular to the picture. Regions with deficient charge compensation are marked with double line.

at about 287.7 − 288.0 eV binding energy corresponds to C in dicyanamide radicals. Its positions do not change between two different compounds because the first atomic neighborhood of carbon does not change during the series. The angles and distances in the $N-C\equiv N$ bound change and they can induce slight charge shifts on C position, thus resulting in modified XPS binding energies. It is worth to mention that C 1s peak in other $C^*-C\equiv N$ groups was reported at 286.73 eV in poly(acrylonitrile) and 286.74 eV in poly(methacrylonitrile) [141]. The peak positioned at about 285.5 eV may be due to adsorbed carbon on the fresh cleaved surface during measurements and/or due to a contamination which results from the solvents used during sample preparation. The existence of two non–equivalent carbon positions in the sample is excluded.

3.1.3 Transition metal core–level lines – Screening effects.

As illustrated in the introductory chapter, the XPS core–level lines of 3d metals comprise information on the valence state, local magnetic properties and local electronic structure. These attributes make them of high interest. The XPS transition metal 2p and 3s core–level lines recorded for $M[N(CN)_2]_2$ compounds are listed in Figures 3.7 and 3.8.

Before turning to analysis of these results, it is useful to see to what extent these experimental data may be compared to the XPS spectra of transition metal oxides. Such a comparison is appealing since the core–level lines of simple or complex oxides are nowadays more or less well understood[2]. As mentioned in the sections 1.1.2.5 and 1.1.2.7 the structure of 2p and 3s lines depends on various factors which can be divided in intra– and extra–atomic features. As the self–explanatory denomination, the first are specific for the ionic species and may be compared between similar ions in two different compounds. The extra–atomic features are instead characteristic of for particular material and depend on the local geometry or the first atomic neighborhood of the 3d–metal. This last aspect becomes evident for the configuration–interaction cluster approach to the Anderson hamiltonian [78, 79, 142, 143]. Screened final–states,

[2]In Osnabrück a long track of scientific results has been achieved during the last decade in this field and high–resolution spectra of simple and complex TM oxides are available.

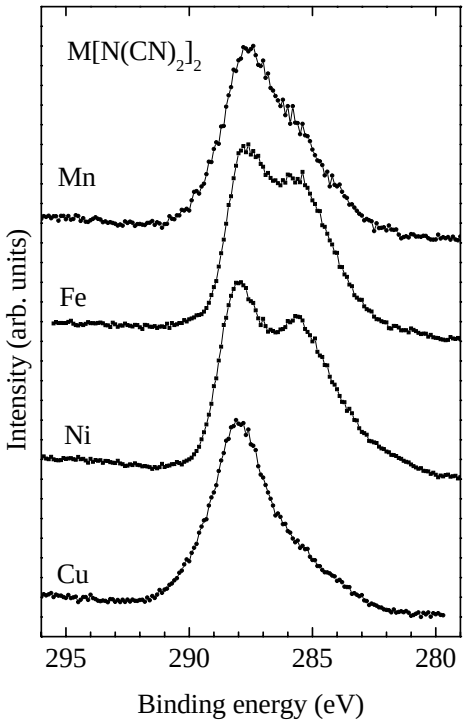

Figure 3.6: XPS 1s core–level lines of carbon in $M[N(CN)_2]_2$.

where an electron is transferred from a ligand atom in order to screen the created core–hole, might play an important role in the shape of the spectra.

For transition metal oxides the interplay between final state effects and exchange interaction or spin–orbit coupling may be estimated in frame of Zaanen–Sawatzky–Allen diagram [144]: it classifies the transition metal compounds with respect to their ligand to metal charge transfer energy, the d–d Mott–Hubbard repulsion and bandwidths of metal and ligand states. Such an approach cannot account for fine structures in the spectra but delivers a reliable base of discussions. According to these reasons the comparison of XPS transition metal core–level spectra coming from different classes of materials must be carefully defined. Actually one should be capable to discern the contribution of extra–atomic effect and then to compare the specific TM features.

The most striking feature of the Mn 2p spectra (Figure 3.7, MnO spectrum from [51]) is the lack of significant charge–transfer features. This is similar to the case of MnO [51, 142] where the charge–transfer effects only play a secondary role[3]. The Mn 3s spectra (Figure 3.8) is marked by the same feature: the spectra can be fitted with only two symmetric lines. Additionally the splitting between the two peaks resembles the value specific for MnO – Figure 3.9 (MnO 3s spectrum from [51]). The magnetic moment on manganese is 4.65 μ_B in $Mn[N(CN)_2]_2$ [133] and 4.45–4.79 μ_B in MnO [145, 146].

[3]The comparison to another divalent manganese compound was not randomly selected. As it will be shown later, Mn^{2+} in $Mn[N(CN)_2]_2$ is not only a formal valence state but also reflects the electronic structure configuration.

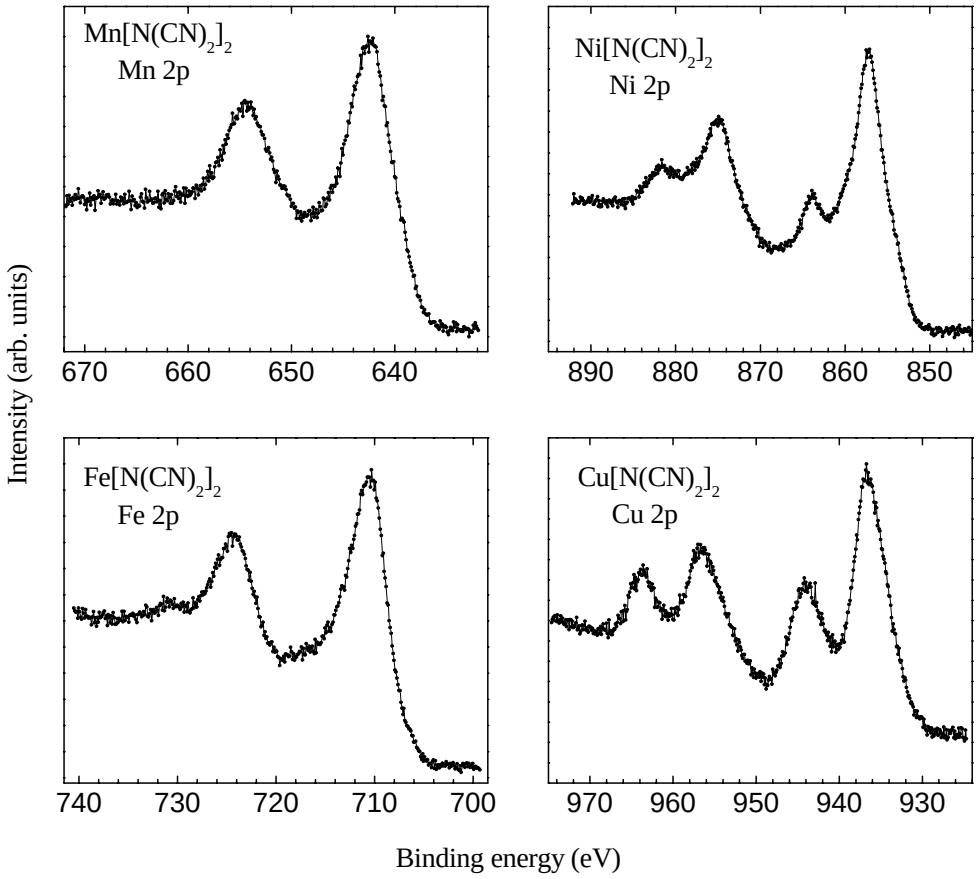

Figure 3.7: XPS transition metal 2p core–level lines of $M[N(CN)_2]_2$ compounds.

Thus it is reasonable to propose that in the Mn core–level lines of the investigated dicyanamide material no significant charge–transfer features are present, the Mn 3s splitting being a good measure of the local magnetic moment. Eventual small screening features may be enveloped by the relatively broad lines. The comparison with MnO suggests a $3d^5$ configuration in concordance to the magnetic measurements [133]. The binding energy of the Mn $2p_{3/2}$ line (642.4 eV) is higher than the one of Mn $2p_{3/2}$ in MnO (640.1–641.1 eV [51]) and closed to that of Mn $2p_{3/2}$ in $MnCl_2$ (about 642 eV [147]) thus indicating a more ionic character of manganese in the dicyanmide compound. The two peaks in Mn 2p spectrum are then assigned to spin–orbit coupling components in non–screened final state $2p^53d^5L$. In a similar way the two peaks in the Mn 3s spectrum are assigned to the high–spin HS (^7S) and low–spin LS (^5S) final states without charge–transfer $3s^13d^5L$.

The following question arises: is it physically reasonable to make the above designations? As it will be shown in the next section and can it be deduced from the $3d^5$ electronic configuration, the Mn 3d states dominate the top of the valence band. Unoccupied 3d states are present above the insulating gap, probably in the lower unoccupied molecular orbital. Assuming frozen states for the ligand (like illustrated in Figure 1.8), the screening relaxation in the final state implies the empty states of

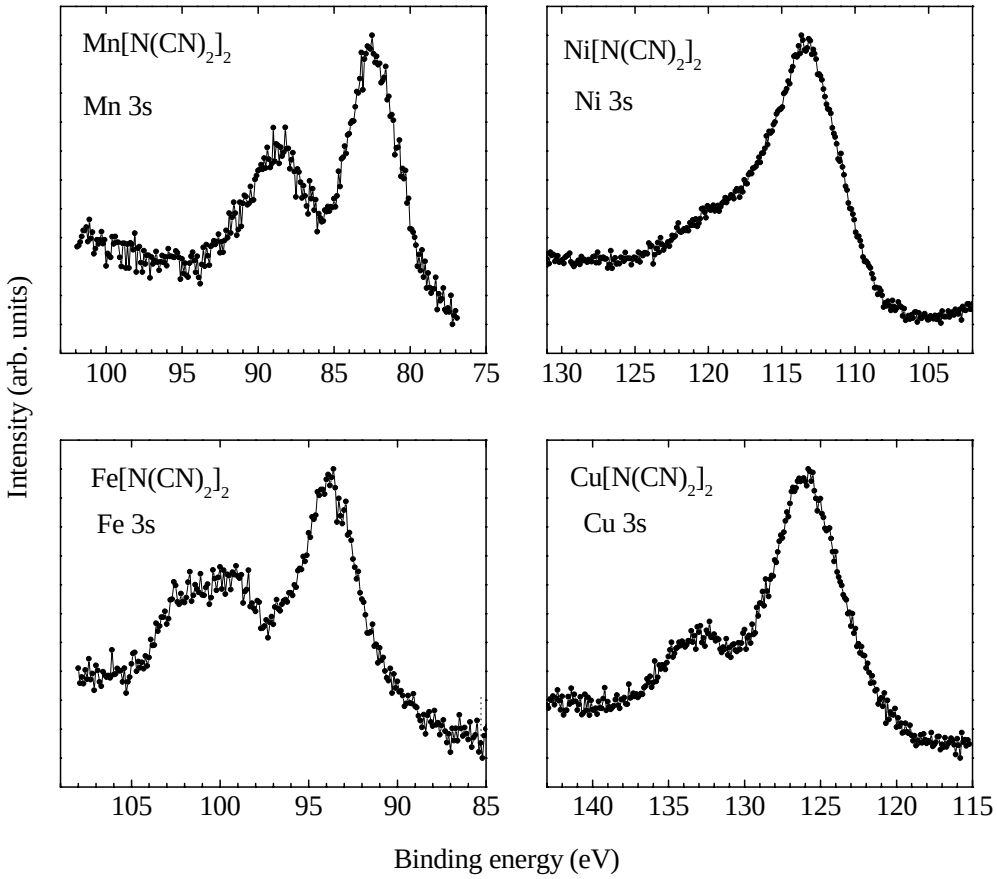

Figure 3.8: XPS transition metal 3s core–level lines of $M[N(CN)_2]_2$ compounds.

the metal ion will be shifted below the ligand occupied states. For a $3d^5$ configuration this is less probable as for a $3d^6$ or $3d^7$ one. For the late transition metal oxides the energy requested for the charge transfer process decreases with increasing number of 3d electrons [148]. With these considerations the correctness of the above assignments is granted.

The XPS 2p core–level spectrum of iron (Figure 3.7) shows some small but visible peak around 730.7 eV below the $2p_{1/2}$ component. This indicates that charge–transfer effects are present and must be included in the analysis. For the $2p_{3/2}$ component the charge–transfer feature is present as a asymmetry of the line's shape. Similar remarks can be made for the case of the Fe 3s spectrum (Figure 3.8). Some third peak at about 102.1 eV has a intensity which cannot be described in the frame of the 3s multiplet splitting theory and corresponds most probably a impurity line[4]. It is worth to mention that the distance between the first and the second peak in the Fe 3s spectrum $Fe[N(CN)_2]_2$ and FeO spectra is almost the same for both iron compounds – Figure 3.11.

[4]The foreign contribution can be assigned to some silicon impurity content resulted from the chemical synthesis process. If so, the C to Si atomic concentration ration is higher than 1000 to 1 which resembles a tiny, hardly detectable silicon amount.

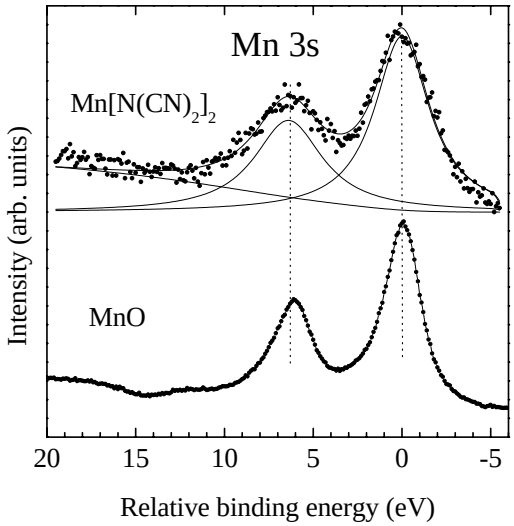

Figure 3.9: Multiplet splitting of manganese 3s line in $Mn[N(CN)_2]_2$ (upper panel) and for comparison in MnO (lower panel, from [51]).

The absolute binding energy of Fe $2p_{3/2}$ line (710.1 eV) in $Fe[N(CN)_2]_2$ is higher than the value measured for FeO (709.2–709.5 eV [147]). This result reveals a higher degree of ionic character compared to the corresponding oxide.

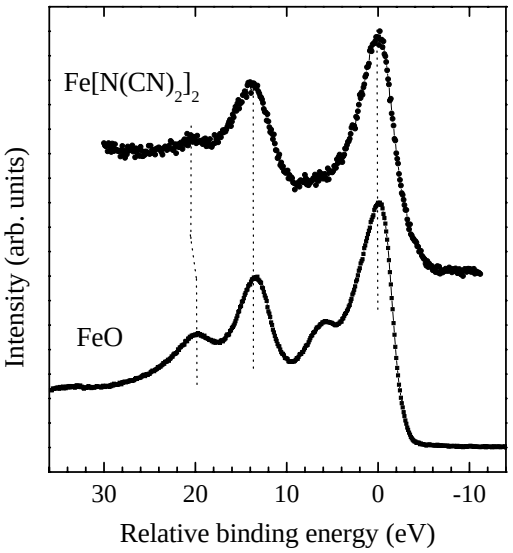

Figure 3.10: XPS 2p spectra of iron in $Fe[N(CN)_2]_2$ and FeO (from [51]).

Taking into account the analysis presented in [78, 79, 142, 148] and assuming only reduced charge–transfer features, one can assign the two most intensive peaks at 93.8 and 99.2 eV to the HS and respectively LS final state without screening (see Figure 3.11, FeO spectrum from [148])). The magnetic moment on iron in FeO is 3.32–3.36 μ_B [145, 146] and 4.23 μ_B in $Fe[N(CN)_2]_2$. The last value is closer to 4.9 μ_B expected from the spin contribution of a Fe^{2+} ion.

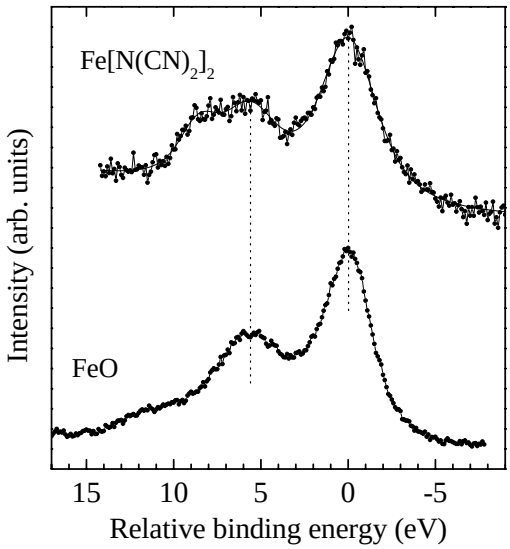

Figure 3.11: XPS 3s spectra of iron in $Fe[N(CN)_2]_2$ and FeO (from [51]).

In case of the compositions with Ni and Cu the charge–transfer features of both 2p and 3s spectra are even more pronounced. The Ni $2p_{3/2}$ is given by a doublet at 857.3 and 863.9 eV. In NiO the lowest and most intensive component of the $2p_{3/2}$ line was found at 854.1 eV [51]. Once again, this suggest a higher degree of ionic character for the manganese bounds when compared to the corresponding oxide. The intensities of two virtual peaks fitting the Ni 3s spectra would be far from the value expected for a $3d^8$ configuration (3 : 2, see section 1.1.2.7) thus motivating some other configuration of peaks under the experimental curve. The situation is similar for the Cu 3s spectrum. The components of Cu $2p_{3/2}$ are positioned at 936.5 and respectively 944.1 eV. For CuO the most intensive peak is located at 932.5 eV [51]. These considerations lead to the conclusion that the 'visual' multiplet splitting exhibited in these 3s spectra do not directly reflect the value of local magnetic moment. Still, since charge–transfer effects occur in case of $Cu[N(CN)_2]_2$ the d–orbital occupation must be lower than $3d^{10}$.

	$Mn[N(CN)_2]_2$	$Fe[N(CN)_2]_2$	$Co[N(CN)_2]_2$	$Ni[N(CN)_2]_2$	$Cu[N(CN)_2]_2$
XPS line					
N 1s	398.0	398.3	398.5	397.2	397.8
	399.6	399.6	399.6	399.6	399.6
C 1s	287.7	287.7	287.4	288.0	288.0
M $2p_{3/2}$	642.4	710.1	782.2	857.2	936.5

Table 3.2: XPS binding energies (eV) for the $M[N(CN)_2]_2$ dicyanamide compounds.

Concluding, for compounds with Mn and Fe the screening effects were found to be low enough so that the 3s multiplet splitting reflect the local magnetic moment. For compositions with Ni and Cu the final–state effects are considerably high and the shape of the 3s splitting is more complicated.

3.1.4 Modelling the transition metal 3s multiplet line

A deeper insight on the structure of 3s TM spectra and the extent screening effects have to be taken into account can be achieved by employing an appropriate model for the multiplet splitting for insulating materials. Such approaches are presented in [78, 79, 142, 148] and were employed to describe simple TM oxides. In order to define the involved physical values as well as the restrictions of the models, the corresponding physical aspects are summary presented and commented below.

The 3s multiplet spectrum is primarily a sum of magnetic exchange derived spin configurations (HS states $^{2S+2}\Gamma$ and LS states $^{2S}\Gamma$). Further, since a charge transfer from ligand to metal ion accounts for the screening of the final states 3s core–hole, HS and LS states without or with charge transfer must be considered (HS states: $|3s^1 3d^n L;^{2S+2}\Gamma\rangle$ and $|3s^1 3d^{n+1}\underline{L};^{2S+2}\Gamma\rangle$, LS states: $|3s^1 3d^n L;^{2S}\Gamma\rangle$ and $|3s^1 3d^{n+1}\underline{L};^{2S}\Gamma\rangle$. For purely ionic compounds, a cluster approximation Hamiltonian approach can be employed to describe the transitions from initial to these final states [149], which is applicable to octahedral surroundings of the TM ion. The initial state Ψ_{in} and final states $\Psi_{fin,i}$ are written as linear contribution of state without and with charge transfer: $\Psi_{\mathrm{in}} = \alpha_0|3d^n\rangle + \alpha_1|3d^{n+1}\underline{L}\rangle + \alpha_2|3d^{n+2}\underline{L}^2\rangle$ with $\alpha_0^2 + \alpha_1^2 + \alpha_2^2 = 1$, $\Psi_{\mathrm{fin,i}} = \alpha_0^{\mathrm{i}}|3s^1 3d^n\rangle + \alpha_1^{\mathrm{i}}|3s^1 3d^{n+1}\underline{L}\rangle + \alpha_2^{\mathrm{i}}|3s^1 3d^{n+2}\underline{L}^2\rangle$ with $\alpha_0^{\mathrm{i}} + \alpha_1^{\mathrm{i}} + \alpha_2^{\mathrm{i}} = 1$. The matrix elements of the Hamiltonian for the initial states are:

$$\mathcal{H} = \begin{pmatrix} 0 & \sqrt{2}T & 0 \\ \sqrt{2}T & \Delta & \Delta \\ 0 & \sqrt{2}T & 2\Delta + U_{dd} \end{pmatrix} \tag{3.1}$$

where

$$\langle 3d^{n+1}\underline{L}|\mathcal{H}|3d^{n+1}\underline{L}\rangle = \Delta \tag{3.2}$$

is the charge–transfer energy,

$$\langle 3d^{n}\underline{L}|\mathcal{H}|3d^{n+1}\underline{L}\rangle = \sqrt{2}T \tag{3.3}$$

$$\langle 3d^{n+1}\underline{L}|\mathcal{H}|3d^{n+2}\underline{L}^2\rangle = \sqrt{2}T \tag{3.4}$$

is the transfer integral and U_{dd} is the effective d–d Coulomb interaction or Mott–Hubbard energy. For the final states the matrix elements of the Hamiltonian can be written for HS and LS configurations trough diagonal E_c terms which are related to the exchange energy given by equation 1.23. The $\mathcal{H}_{HS}$ are then written as:

$$\mathcal{H}_{HS} = \begin{pmatrix} E_c(L;^{2S+2}\Gamma) & \sqrt{2}T & 0 \\ \sqrt{2}T & E_c(\underline{L};^{2S+2}\Gamma) + (\Delta - Q_{sd}) & \Delta \\ 0 & \sqrt{2}T & 2(\Delta - Q_{sd}) + U_{dd} \end{pmatrix} \tag{3.5}$$

where Q_{3d} is the 3s–3d Coulomb interaction. For simplicity the occupancy of 3d sub–shell was not included in notation. Analogous:

$$\mathcal{H}_{HS} = \begin{pmatrix} E_c(L;^{2S}\Gamma) & \sqrt{2}T & 0 \\ \sqrt{2}T & E_c(\underline{L};^{2S}\Gamma) + (\Delta - Q_{sd}) & \Delta \\ 0 & \sqrt{2}T & 2(\Delta - Q_{sd}) + U_{dd} \end{pmatrix} \tag{3.6}$$

For convenience the HS energies can be defined as reference:

$$E_c(\mathrm{L};^{2S+2}\,\Gamma) = E_c(\underline{\mathrm{L}};^{2S+2}\,\Gamma) = 0 \tag{3.7}$$

and the LS diagonal energies result as:

$$\langle 3d^n|\mathcal{H}_{HS}|3d^n\rangle - \langle 3d^n|\mathcal{H}_{LS}|3d^n\rangle = E_c(\mathrm{L};^{2S}\,\Gamma) \tag{3.8}$$

$$\langle 3d^{n+1}\underline{\mathrm{L}}|\mathcal{H}_{HS}|3d^{n+1}\underline{\mathrm{L}}\rangle - \langle 3d^{n+1}\underline{\mathrm{L}}|\mathcal{H}_{LS}|3d^{n+1}\underline{\mathrm{L}}\rangle = E_c(\underline{\mathrm{L}};^{2S}\,\Gamma) \tag{3.9}$$

It should be noticed that the values of exchange splitting are reduced to about a half by the configuration interaction in the final state (see Section 1.1.2.7). In the sudden approximation the spectrum is then given by [149]:

$$\rho(\xi_k) = \sum_{i=1}^{3} |\langle \Psi_{fin,i}|\underline{c}\Psi_{in}\rangle|^2 \delta(\hbar\omega + \delta - \xi_k - E_i) \tag{3.10}$$

where E_i represents the final–states energies, ξ_k the kinetic energy of the photoelectron, $|\underline{c}\Psi_{in}\rangle$ represents the frozen state obtained by annihilation of a core–electron in the ground state (see also Section 1.1.1.1).

Several approaches were developed for TM simple oxides starting from the above considerations. In [78] an empirical reduction of the energy splitting due to final state configurations was assumed and a fit was performed starting from calculated values of Δ and U_{dd}. Later same authors published a more sophisticated model where some of the matrix elements were prior calculated in a cluster Hartree–Fock approach [79]. It is questionable to what extent such a simulation is better than its previous form [5]. Moreover the constrains between the model parameters seem to be not included. This makes the numerical results less deterministic even if they are correct. An elegant model approach has been developed in Osnabrück [148]: it considers the constrains between the peak positions and intensities resulting from a proper parameterization of initial and final states and ignores the double–hole ligand states contributions. This is more than reasonable since the $3s^1 3d^{n+2}\underline{\mathrm{L}}^2$ contributions are very low.

In order to apply any of the above models to TM 3s spectra of dicyanamide materials a particular numerical procedure is required since the extra–atomic specific values employed for oxides cannot be used. This is a common feature of all the listed procedures. The reason for this is the nitrogen octahedral surrounding of metal ions which makes it difficult to find the proper starting point for the fit procedure.

A proper numerical approach was developed in this work. The fit consists from two steps: first the proper starting point is found in the limits of physical constrains by means of a Monte–Carlo approach; secondly the values of the parameters are refined in an adapted non–linear Levenberg–Marquardt method [150]. The Monte–Carlo procedure was run with at least 300.000 points in the parameter space. For all the peaks a Lorenz–Gauss product form was used with a free mixing parameter:

$$f(\epsilon) = I_0 \left\{ 1 + m \left[\frac{\epsilon}{(\gamma/2)} \right]^2 \right\}^{-1} \cdot \exp\left\{ -(1-m)\ln 2 \left[\frac{\epsilon}{(\gamma/2)} \right]^2 \right\} \tag{3.11}$$

[5] There is a real possibility to reach deviated results since different types of overlap integrals resembling the same cluster are calculated outside the fitting procedure.

where m is the Lorenzian–Gaussian mixing ratio and the rest of parameters are defined as in section 1.1.2.6. This symmetric line–shape has the advantage to give a good analytical description of the physical parameters. The figure of merit function that measures the agreement between data and model was chosen in a normalized metric distance form [151]:

$$\chi = \frac{1}{\sqrt{2}} \sqrt{\sum_{i=1}^{n} \left(\frac{y_i}{|y|} - \frac{F(y_i)}{|F|} \right)^2} \tag{3.12}$$

where y_i are the experimental points and F is the model function. For $|y|$:

$$|y| = \sqrt{\sum_{i=1}^{n} y_i^2} \tag{3.13}$$

The choice of this form is motivated by the nature of experimental points: in a XPS spectrum a higher number of counts reflects a better spectrum i.e. a lower detection error. The reduction of exchange energy over the value of free ion was accounted for final states with or without charge–transfer with two fit parameters. In order to take into account the $3s^1 3p^6 3d^n$ – $3s^2 3p^4 3d^{n+1}$ and $3s^1 3p^6 3d^{n+1}$ – $3s^2 3p^4 3d^{n+2}$ configuration interactions, the coefficients k^n and respectively k^{n+1} were used as fit parameters [148]. The numerical code was first tested on the spectra of simple oxides of TM and the results were in concordance to the data available in the literature. The input data are: the experimental points and the lower and upper limit chosen for the model parameters.

The results of the fit are presented in Figure 3.12 and the values of model relevant parameters are listed in Table 3.3.

	Δ (eV)	Q_{sd} (eV)	T (eV)	ΔE(HS–LS) (eV)
$Mn[N(CN)_2]_2$	11.5	4.4	1.7	6.3(5)
$Fe[N(CN)_2]_2$	7.8	5.2	2.4	5.4(6)
$Ni[N(CN)_2]_2$	3.1	6.0	2.8	2.8(4)
$Cu[N(CN)_2]_2$	2.1	6.3	2.9	1.5(7)

Table 3.3: Parameter values obtained from the model analysis of the 3s multiplet splitting.

In case of the $Mn[N(CN)_2]_2$ 3s XPS spectrum it becomes clear that the HS and LS states without screening are prevalent. The contributions of $|3s^1 3d^{n+1}\underline{L}\rangle$ states are very low due to a large ligand to metal charge–transfer energy Δ and the measured splitting is due to exchange interaction only. The percentage composition for the intensities of the peaks situated at 82.4 and 88.7 eV are $95\%|3s^1 3d^5 L;\ ^7S\rangle$ + $5\%|3s^1 3d^6\underline{L};\ ^7S\rangle$ and $97\%|3s^1 3d^5 L;\ ^5S\rangle$ + $3\%|3s^1 3d^6\underline{L};\ ^5S\rangle$. The value of the parameter Q_{sd} was found, as expected, to be close to the results obtained for manganese oxide (4.5 eV in [79] or 5.0 eV in [148]). In Reference [79] it was argued for MnO that an even higher value of the Δ parameter does not really affect the shape of the simulated curve since its magnitude is already high enough to dump down any

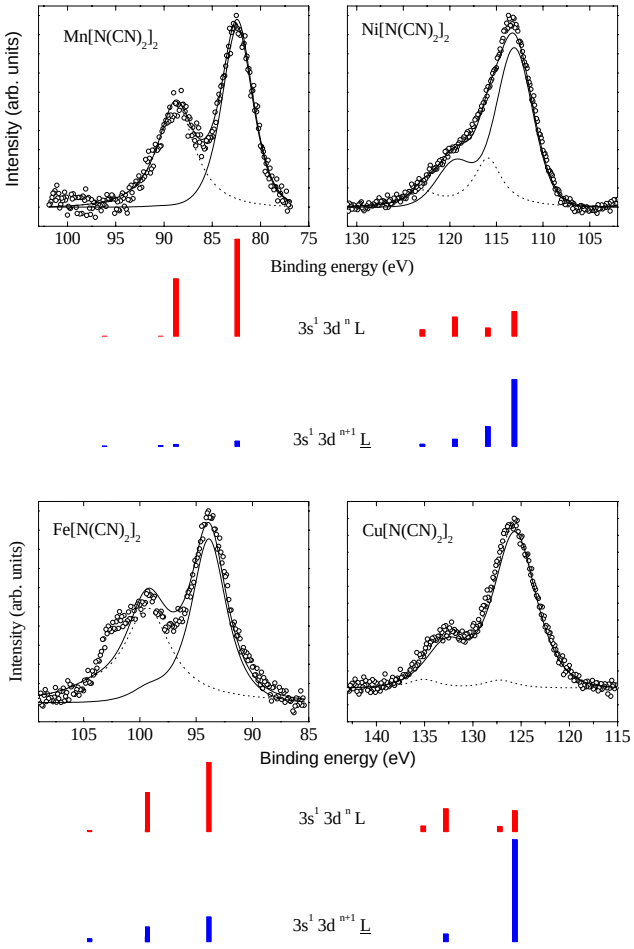

Figure 3.12: XPS spectra (circles) and model calculations (lines) of the 3s core levels. HS contributions are drawn with normal line while the LS ones are represented with dotted line. Below the spectra the composition of each line in terms of non–screened and screened final states is shown.

screening effects. According to the constrains resulted in our case from the physical model [148], such an conclusion becomes erroneous so that an unambiguous value of Δ was determined.

For $Fe[N(CN)_2]_2$ the charge–transfer energy is lower and allows a higher mix with screened final states. It is energetically easier to transfer electrons from the ligand nitrogen atoms to the metal ion. On the scale of atomic orbital energies the lower Q_{sd} value is due to the non–zero occupancy of minority spin 3d orbitals of iron which makes the further population of spin–down states to be more accessible. However the charge–transfer energy is not low enough to generate high contributions of final states with charge–transfer weight and the value of measured splitting is still a value of the magnetic exchange interaction. The percentage composition for the intensities of the peaks situated at 93.9 and 99.3 eV with respect to the nature of final states are $74\%|3s^1 3d^6 L;\ ^6D\rangle + 26\%|3s^1 3d^7 \underline{L};\ ^6D\rangle$ and $73\%|3s^1 3d^6 L;\ ^4D\rangle + 27\%|3s^1 3d^7 \underline{L};\ ^4D\rangle$. The Q_{sd} values previously derived for Fe(II) are 3.5 eV [79] and 5.8 eV [148].

The weight is changed for $Ni[N(CN)_2]_2$ and the trend observed for the compound with iron is confirmed. Δ becomes even lower and final states with a ligand core–hole must be accounted on equal footing with those without charge–transfer. The most striking feature of the Ni 3s spectrum (Figure 3.12) is the reduced relative intensity for the states in LS channel. The visible splitting fails to resemble the magnetic exchange interaction and is a measure of the charge transfer effect i.e. a extra–atomic property. The composition for the intensity of the main line positioned at 113.1 eV is $27\%|3s^1 3d^8 L;\ ^4F\rangle + 73\%|3s^1 3d^9 \underline{L};\ ^4F\rangle$. The ascertained Q_{sd} value is close to the values derived for NiO: 7.0 eV [79] and 6.5 eV [148].

For the last analyzed case of $Cu[N(CN)_2]_2$ the natural relaxation tendency of the system with a 3s core–hole is supported by a very low Δ. Final states with an electron transferred from ligand to metal position become dominant and the LS channel is drastically suppressed. The main line of the Cu 3s spectrum at 125.6 eV has the following composition: $21\%|3s^1 3d^9 L;\ ^2D\rangle + 73\%|3s^1 3d^1 0\underline{L};\ ^2D\rangle$.

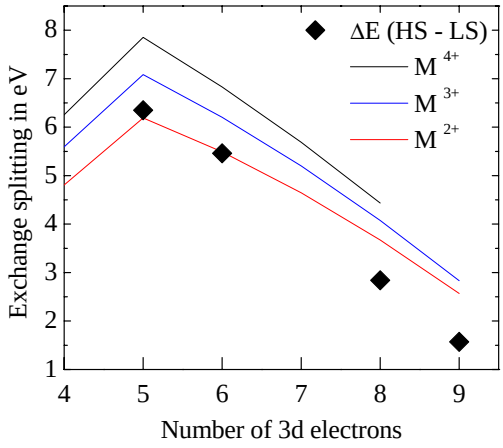

Figure 3.13: Comparison between the exchange splitting deduced from the 3s–model and the theoretically expected values for divalent, trivalent and quadrivalent 3d ions (from [148]).

Concluding, the analysis of screening effects in the TM XPS core–level lines reveals that for compositions with Mn and Fe the spectra resembles M^{2+} real valence states while for dicyanamide compounds with Ni or Cu this conclusion in only indirect. By employing an appropriate model the values of exchange splitting can be extracted from the experimental data and compared with the values theoretically expected for different valencies (Figure 3.13). In frame of this model, it can be deduced that all the TM ions are in divalent state in the investigated materials.

3.1.5 Valence band studies

The occupied density of states in the valence region was investigated by means of XPS and XES[6] measurements. Figure 3.14 shows the XPS valence band spectra of $Mn[N(CN)_2]_2$ along with the selectively excited XES data of each atomic species (see also [152]). The excitations energies used for the shown XES spectra were chosen to correspond to the L_α edge for Mn and K_α threshold for C and N resulting from the absorption spectra, so that a close picture of the undistorted element specific density of state is achieved[7]. The emission spectra are correlated with the occupied density of states in the valence band region by taking into account the binding energies of core levels, as extracted from the XPS core–level spectra (see Table 3.2). The features (peaks) visible in the XPS valence band spectrum and their corresponding peaks in the XES spectra are denoted with $A - F$. The comparison reveals that the top of valence (A) band is mainly derived from Mn 3d states while its bottom (F) is mostly due to 2s states of carbon and nitrogen. Some contribution to structure F comes from C 2p states as visible in the C emission spectrum. In the middle part of the valence band (B, C, D) the Mn 3d, N 2p and C 2p are strongly hybridized forming a broad structure in the XPS valence band. The feature E is formed by mixed N and C 2p states.

A deeper insight on the hybridization mechanisms and contribution of particular orbitals to the structures present in the valence band can be achieved by means of electronic structure calculations. The computational approach is however not trivial. Even tremendous progresses have been made in this field, the theoretical approach to the electronic structure of metal–organic compounds is still a delicate undertaking. The possible question marks may be tuned off by means of joint experiment–theory studies.

The calculations for $Mn[N(CN)_2]_2$ bulk crystal and terminated cluster models have been computed in frame of a joint co–operation by M. R. Peredson[8] [152]. The results from Reference [152] are shown in Figure 3.15. The lowest three panels show the densities of states which were broadened by 1.0 eV and the upper three by 0.3 eV in order to simulate the experimental broadening and to help the identification of structures. The total and 3d projected density of states are presented in the forth panel. For N and C densities the total and 2p components are shown.

The theoretical results show that the manganese density of states below the Fermi level (A) is entirely due to majority states while the states above the Fermi level are composed entirely of minority states. This points out a $3d^5$ electronic configuration of the Mn ions (+2 charge state) and a local spin moment of 5.92 μ_B. Additionally the Mn 4s contribution to the valence states was shown to be negligible. To be

[6]The XAS/XES data for dicyanamide materials were kindly provided Prof. Dr. Ernst. Z. Kurmaev

[7]This approach is actually an approximation. Even the absorption spectra is well resolved, it is difficult to tune the excitation XAS energy exactly to the desired value. Experimental as well as theoretical reasons are responsible for this. However it is reasonable to expect that in the excitation energy region very closed to the XAS edge, the emission spectra should resemble the density of states.

[8]Actual address: Center for Computational Materials Science, Code 6390, Naval Research Laboratory, Washington, DC 20057, United States

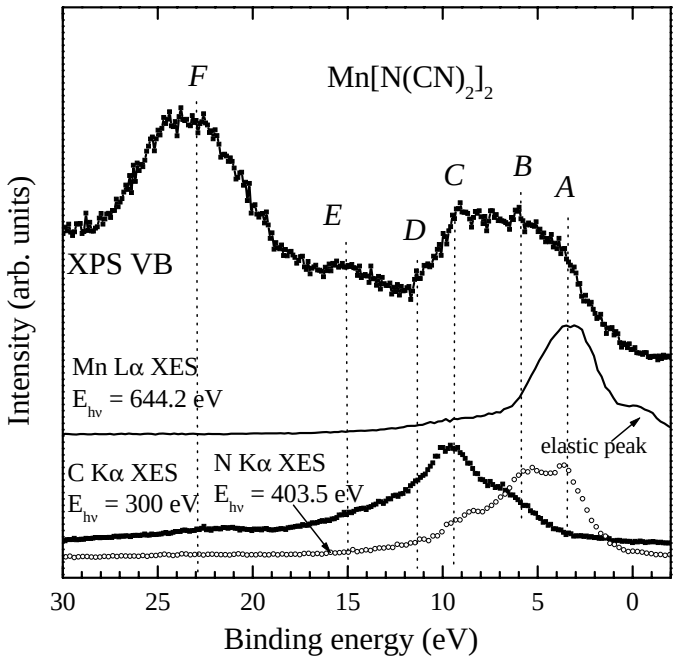

Figure 3.14: XPS valence band of $Mn[N(CN)_2]_2$. In the lower part the resonant XES spectra of constituents are presented.

mentioned XPS and XES probe occupied density of states so that the minority states are neither present in the XPS valence bad spectrum nor in the Mn XES curve. All the structures $A-F$ have been reproduced by the density of states curve. By accounting the elemental contribution to each of them, conclusive remarks can be made with respect to each key structure in valence band. Region F has large contribution from the N 2s, C 2s and C 2p orbitals and approximately resembles the composition of $2s\sigma$ bonding orbital for an isolated cyanide CN^- molecule which is: 50% N 2s, 20% C 2s, 10% N 2p and 10% C 2p. The $2s\sigma^*$ antibonding states, $2p\pi$ and $2p\sigma$ bonding states are situated about 11.8–14.5 eV above the bonding $2s\sigma$ states in CN^- which roughly corresponds to regions B, C and D.

Starting with the lower binding energies the features in the valence band of $Mn[N(CN)_2]_2$ can be thus assigned as it follows:

- F with a maximum at about 23 eV binding energy (Figure 3.14) has contributions from the N 2s, C 2s and C 2p atomic orbitals and roughly corresponds to the $2s\sigma$ bonding orbital of the cyanide radicals $C\equiv N^-$. It is thus not only visible in the N Kα XES spectrum but also present in the C Kα emission data

- E positioned at 15 eV is almost entirely due to N 2p states of the nitrogen atoms that form the local axis of symmetry i.e. $N-Mn-N$ axis of $Mn[N(CN)_2]_2$ molecule. Its weak signal can be observed in the N Kα XES spectrum.

- D at 13 eV correlates with the N and C Kα XES spectra and resembles the antibonding $2s\sigma^*$ molecular orbital in the cyanide $C\equiv N^-$ radical. It is visible in both the N and the C Kα XES spectra.

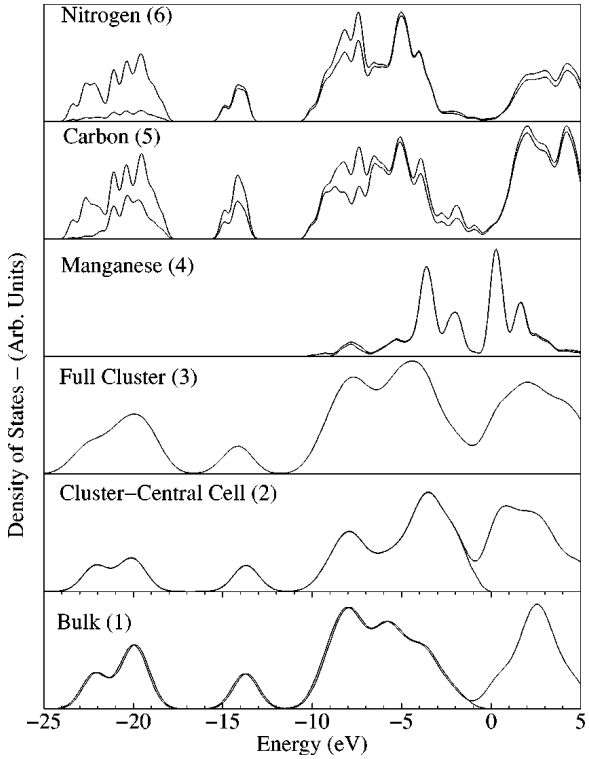

Figure 3.15: Calculated total and projected densities of states for $Mn[N(CN)_2]_2$ (from [152], see text for further details).

- *C* visible at about 9.3 eV comply with the composition of the bonding 2pπ molecular orbital of $C\equiv N^-$ and is strongly emphasized in both the N and the C Kα XES spectra. It corresponds practically to the maximum of the C Kα XES spectrum and a pronounced shoulder in the N Kα data.

- *B* present at 5.8 eV has contributions from the Mn 3d, N 2p and C 2p states and appears in all the resonant XES spectra shown in Figure 3.14. The contribution from nitrogen and carbon atoms may be assigned as being derived from the 2pσ molecular orbital of $C\equiv N^-$ radical. Its position correlates with a distinct shoulder of the C Kα spectrum and a local maximum in the N Kα spectrum.

- *A* at 3.4 eV corresponds to the higher occupied molecular orbital and its composition, as revealed by electronic structure calculations, is almost exclusively due to Mn 3d states. It accounts for the maximum visible in the Mn L_α resonant spectra. It is also visible as a local maximum in the N Kα spectrum.

The relative different weights for the composition of each structure, as resulting from the analysis of XPS/XES intensities and theoretical predictions, is due to the different atomic subshell photoionization cross sections.

An experimental proof for the Mn^{2+} valence state may also be derived from the non–resonant L–emission spectra of manganese states [152]. The comparison of intensity ratio of the $L_{\alpha,\beta}$ lines of the spin–orbit dublet in $Mn[N(CN)_2]_2$ and in reference manganese compounds also suggested the above mentioned charge state.

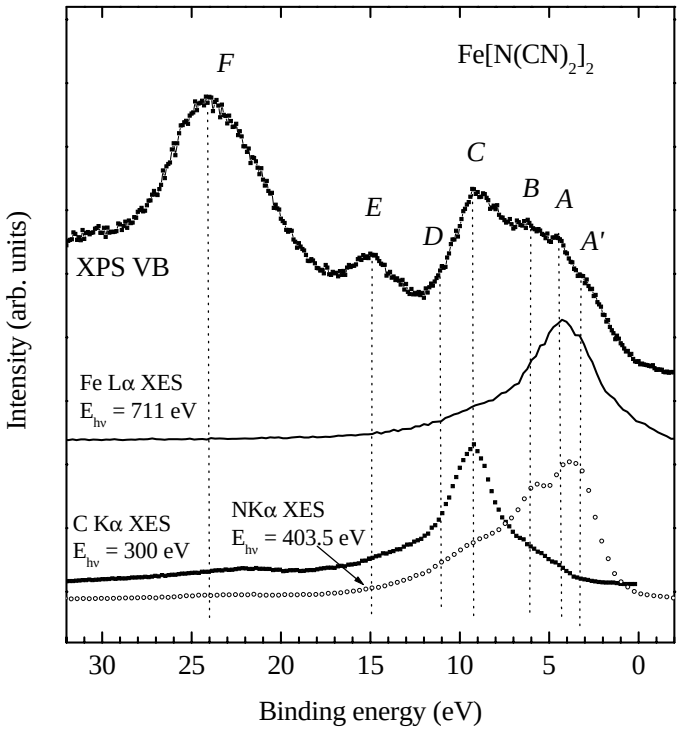

Figure 3.16: XPS valence band spectrum of $Fe[N(CN)_2]_2$ and XES resonant spectra of constituents.

The analysis of the valence band region of $Fe[N(CN)_2]_2$ (Figure 3.16) is analogous to the manganese dicyanamide compound[9]. The resonant XES spectra were included in the picture following the same procedure as for Figure 3.14. Most of the structures due to nitrogen and carbon are retained ($F - C$), only those close to Fermi level show some changes ($B - A$). The feature D becomes less visible and its position in derived from shoulders in both XPS valence band and C Kα XES spectra. Peaks C and B remain well visible on the XPS/XES spectra. The maximum of resonant metal L–emission spectrum is shifted to a higher binding energy as expected from the higher occupation of the 3d orbital (Fe^{2+} and consequently $3d^6$ configuration). Additionally a new feature (A') is present. Its position correlates with a pronounced shoulder in the Fe L_α resonant spectrum. Based on the XES spectra the electronic density composition of feature A' may be derived as mixture of Fe 3d and N 2p states. Accounting for the molecule geometry one can imagine a model scenario like this: the minority spin states of the 3d orbital become occupied when compared with $Mn[N(CN)_2]_2$ and thus the whole 3d band sinks on the energy scale. This also means the localization of 3d electron density is more pronounced in $Fe[N(CN)_2]_2$ than it was in the manganese compound. Fe 3d states hybridize with states of N atoms of the local geometry.

The valence band analysis of the dicyanamide compounds with Ni and Cu can be performed using the same receipt. Along the series common features of the XPS/XES

[9]Up to now electronic structure calculations are not available for further compounds in this series.

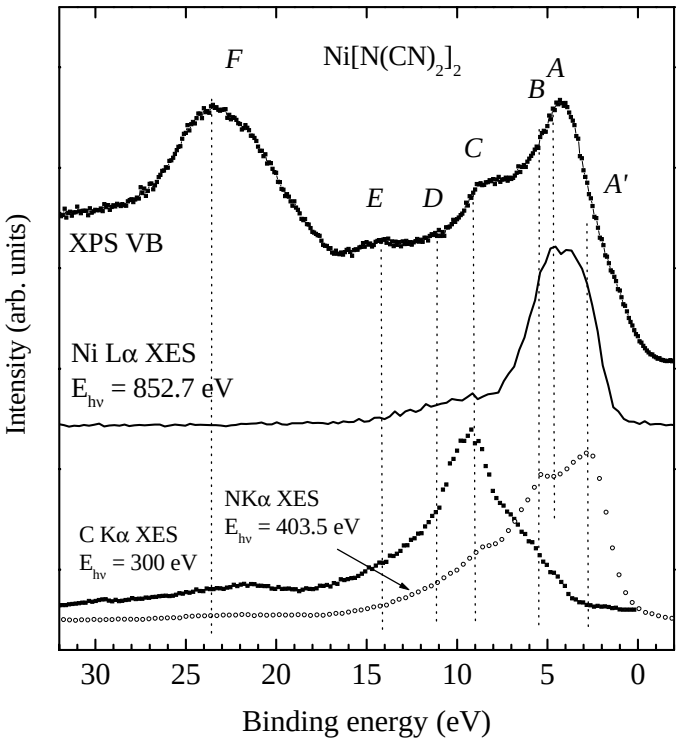

Figure 3.17: XPS valence band spectrum of $Ni[N(CN)_2]_2$ and the resonant XES spectra of constituents.

spectra may be observed and thus a consistent assignment for the visible structures is possible. For this reason only the main features are mentioned below. As in the case of $Fe[N(CN)_2]_2$ some of the maxima conserve their position and this may be related to the dicyanamide–derived orbitals. Thus the structures $F - C$ keep their meaning and the binding energy position. The gradual filling of the 3d orbital leads to a further shift to lower BEs of the gravity center of the d–band, as visible in the Ni and Cu L_α XES spectra. A somewhat changed situation is present in case of $Cu[N(CN)_2]_2$ where the depth of Cu states on the BE scale leads to metal contributions even in the C region. Furthermore the maximum of C Kα is not so well defined as in case of compounds with Mn, Fe or Ni. It should be noticed that the superposition of metal and C,N states on the BE scale does not really mean hybridization since according to the geometry of the crystal they may be localized in different regions of the solid.

Beside the occupied states, the valence band region was investigated with respect to the unoccupied states by means of XAS. The most attractive are from this point of view the 3d–metal states situated above the Fermi level. In Figure 3.19 two examples are presented. The spectra represent excitation from the 2p core levels into the 3d unoccupied valence states.

For the Mn XAS spectrum, the peaks at 639.8 eV and about 641 eV incident photon energies correspond to the excitation on the two main bands represented above the Fermi level in Figure 3.15, since the energy separation between the corresponding maxima is almost the same. As it will be seen later these correspond to t_{2g} and e_g derived bands. The further features at about 638.7 eV and 643.3 eV should be

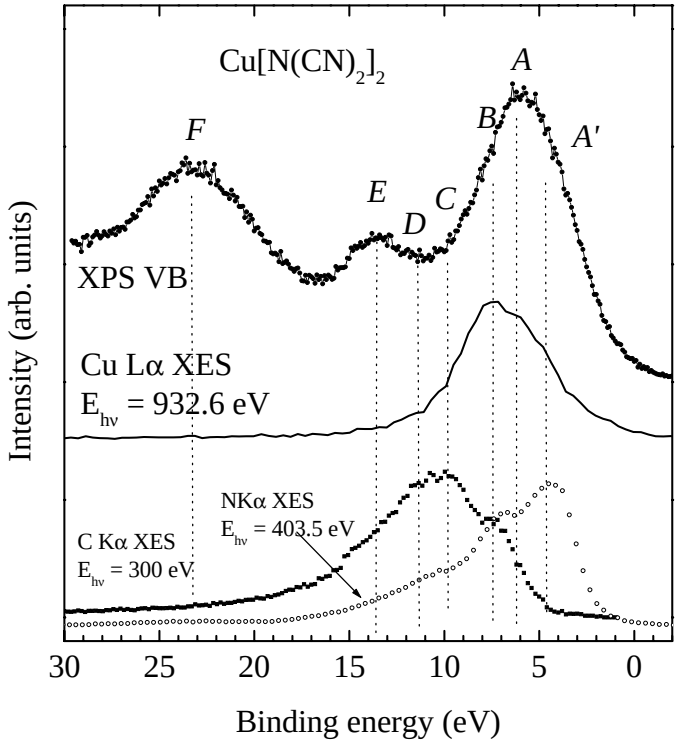

Figure 3.18: XPS valence band spectrum of $Cu[N(CN)_2]_2$ along with resonant XES spectra of constituents.

accounted in the more general theory of atomic multiplets. Just a simple comparison with the results presented in [153] indicate that the actual XAS spectrum is closed to the XAS spectrum of Mn^{2+} in O_h surrounding for $10Dq \approx 0.9$ eV. It can be also supposed that the axial elongation of the octahedral symmetry can account for the two mentioned structures like is was proposed for example in [154]. However without proper calculations such an idea still remains a supposition.

Both axial distortion end energy resolution may be also responsible for the shape of Fe XAS spectrum. It does not look like the calculated spectra for Fe^{2+} in [153]. A double maxima structure at about 706.9 eV and 708 eV probably account for the equally sized unoccupied t_{2g} and e_g (see next section for a complete description).

3.2 Discussion on the electronic structure

The comparison between the XPS valence band spectra and M L_α XES spectra converted to the binding energy scale can be used to separate the contribution of TM ions and bridging dicyanamide groups to the electronic structure. Two aspects are relevant in this direction. The first is that the electronic states arising from the dycianamide groups are roughly retained in the molecular crystal. The corresponding features in the XPS valence band spectra conserve their maximum along the series. With these considerations molecular crystals of this kind can be probably considered as an intermediate step between free molecules and solids with long order interatomic

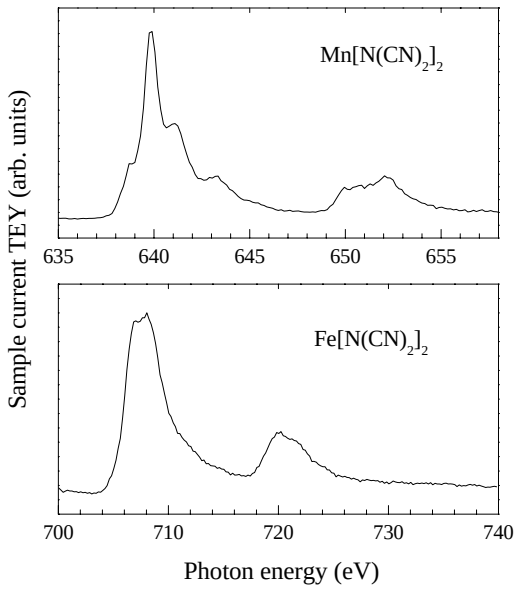

Figure 3.19: XAS spectra of the manganese and iron 2p edges in $Mn[N(CN)_2]_2$ and $Fe[N(CN)_2]_2$.

interactions. Secondly, the electronic states of TM ions are marked by the deepening of 3d–states when going from Mn to Cu which correlates with the gradual filling of 3d4s orbitals. In a simple model it is not possible to account with accuracy for the complicated M 3d4s–(C,N)2s2p hybridization effects but nevertheless one can get a intuitive picture on the electronic structure.

The common structure characteristics for the valence band region of TM dicyanamide materials are marked in Figure 3.20 on the XPS valence spectra. Their corresponding maxima and shoulders in the XES spectra may be followed in Figures 3.14–3.18. The resonant N 1s XES spectrum generally shows two maxima at lower binding energies (3.0–4.5 eV and respectively 5.3–7.6 eV) while a shoulder is present at about 9.2–10 eV. Some smaller structure is visible or must be accounted at 12–13 eV. The C 1s resonant XES spectra are marked by a maximum at 9.2–9.8 eV. At lower binding energies with respect to it a shoulder is visible at the same positions as the second intensive structure of the resonant N 1s spectra (5.3–7.6 eV). At higher values of binding energy a shoulder is present at about 13–14 eV. Another visible structure can be found at 22–23 eV.

With these considerations the maxima discerned in the XPS valence band spectra (Figure 3.20) can be assigned as the following:

- F with a maximum at about 23–24 eV binding energy has contributions from the N 2s, C 2s and C 2p atomic orbitals as explicit calculated for $Mn[N(CN)_2]_2$. Since it is a deep state its composition is expected to be independent on the nature of transition metal ion and to corresponds to 2sσ–derived bonding orbital of the cyanide radicals $C{\equiv}N^-$. The feature F is reflected in the C Kα emission spectrum but fails to be visible in the N 1s XES spectrum according to its composition and selection rules.

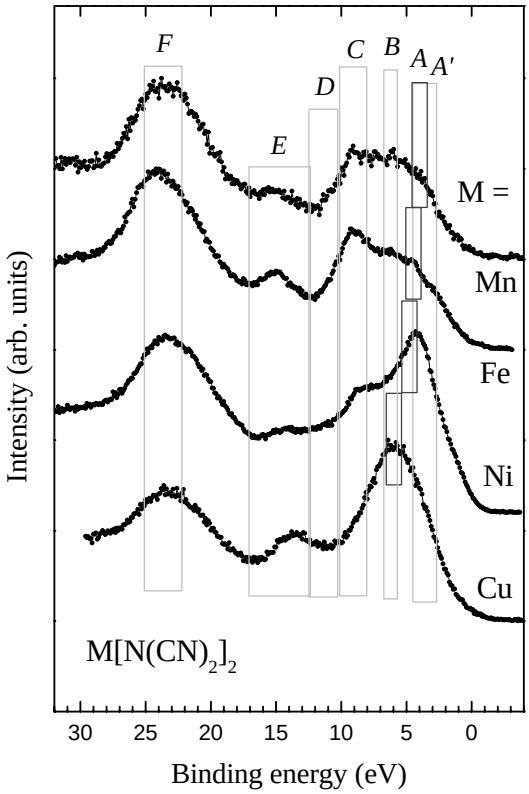

Figure 3.20: XPS valence band spectra of $M[N(CN)_2]_2$ (see body text for further details).

- E positioned at 14.0–15.4 eV is almost entirely due to N 2p states of the nitrogen atoms that form the local axis of symmetry i.e. $N-M-N$ axis of $M[N(CN)_2]_2$ molecule. Its position is slightly shifted when substituting the metal ion which suggest that at this depth on the binding energy scala electronic states due to the metal ion are utterly absent. This is confirmed by all the resonant L_α XES spectra even for the case of $Cu[N(CN)_2]_2$ which has lowest lying states on the BE scale among the transition metals. The small changes may be attributed to the various 3d occupancy of TM ions which implies different Coulomb repulsions. The structure E can be observed in the N Kα XES results.

- D at 11.0–13.0 eV correlates with the N and C Kα XES spectra and in case of $Mn[N(CN)_2]_2$ resembles the orbital composition expected from the antibonding $2s\sigma^*$ molecular orbital in the cyanide $C \equiv N^-$ radical. It is visible in both N and C Kα XES spectra as well as to some small extent in the resonant Cu L_α spectrum. The last has no necessary hybridization meaning although it cannot be excluded. For the further discussions the position of structure D is defined according to the shoulder in C Kα spectra and the corresponding local maximum in the XPS spectra.

- C visible at 8.5–10.0 eV comply with the atomic orbital composition of the

bonding 2pπ molecular orbital of C $\equiv$ N$^-$ and is strongly emphasized in both N and C Kα XES spectra. For further reference the C structure is defined as the maximum in the C Kα as well as the corresponding structure of the valence band spectrum. It is important to mention that this feature is also visible as a shoulder in the metal XES spectra which accounts for hybridization with 3d4s metal states.

While the above mentioned structures in the XPS valence band spectra can be globally defined for all the investigated samples, the other local maxima (B, A and A') request a deeper attention. The gravity center of transition metal 3d4s states shift to higher binding energy from Mn to Cu as the occupancy of the valence orbital increases. Furthermore the patterns are relatively complex and thus the features cannot be really traced back to their elemental composition. Even the assignation of structure C is not so 'clean' as that of F or D.

- B present at 5.1–7.4 eV was shown to have contributions from the M 3d, N 2p and C 2p states for the case of $Mn[N(CN)_2]_2$ and appears in all the resonant XES spectra. It is defined as the region corresponding to the second intensive local maximum in the resonant N 1s spectra. In the investigated 3d–metal dicyanamide series the overlap with metal 3d4s states increases from Mn to Cu. For $Cu[N(CN)_2]_2$ the feature B even coincides to the maximum of resonant Cu L_α spectrum. In all the metal resonant XES spectra its position is marked by a shoulder or maximum. For the sample which contains copper the situation is somewhat changed. The features B and A rather coincide due to the sinking of 3d states on BE scale. Within a rough approximation one can attribute the B maximum to density of states derived from the 2pσ orbitals of cyano group which hybridize with metal 3d4s states.

- A is visible at 3.4 eV for $Mn[N(CN)_2]_2$ corresponds to the higher occupied molecular orbital and its composition is almost exclusively due to Mn 3d states, as mentioned above. In case of the sample with iron (A at 4.4 eV) it still corresponds to the maximum of metal XES spectrum although a shoulder becomes visible at about 3.0 eV. This can be traced to the occupied minority–spin 3d states of Fe. For $Ni[N(CN)_2]_2$ structure A (4.4 eV) still resembles a 3d maximum of the resonant metal emission spectra while for $Cu[N(CN)_2]_2$ the maximum shifts to structure B, as previously mentioned. Formally A may be assigned to the maximum in the metal L_α spectra.

- A' at 2.5–4.0 eV generally corresponds to the first maximum in N Kα spectrum. Since this location is conserved along the series, feature A' also has a rather constant position. For $Mn[N(CN)_2]_2$ A and A' coincide. For all the other samples the feature A' is accompanied by a shoulder in the metal XES spectra resembling a certain M–N hybridization in this region of the BE scale.

Based on the information acquired, the aim of the following discussion will be the modelling of the whole density of states distribution from elemental and molecular 'building blocks'.

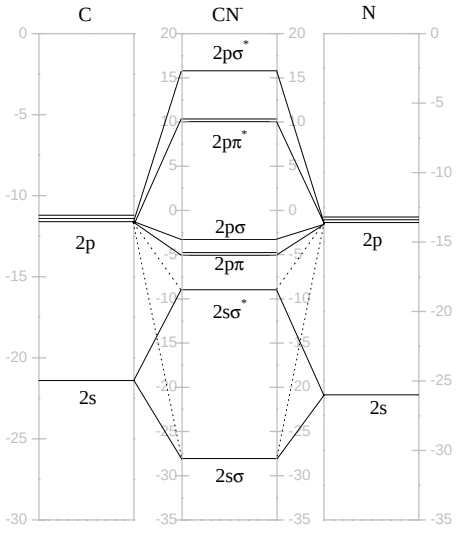

Figure 3.21: Schematic representation of the cyanide molecular orbitals.

As previously suggested an 'effective building block' is the CN group. This is not unexpected since, for example, in the well understood Prussian Blue compounds or other cyano complexes the CN groups retain its characteristic chemical bonding. This idea was additionally underscored by the core–level XPS investigations and by electronic structure calculations for the actual specific case (see previous section). In Figure 3.21 the result of a semi–empirical calculation for the cyanide group is presented. It was performed with the quantum chemistry package *MOPAC*[10]. In the lower part mainly the C 2s and N 2s states are mixed and give rise to the 2sσ bonding and 2sσ^* antibonding molecular orbitals, although there are also some contributions from the C,N 2p states. At higher energies the 2pπ, 2pσ, 2pπ^* and 2pσ^* result from the overlap of C 2p and N 2p states.

Such two cyano groups and one nitrogen atom are contained in the dicyanamide group (pseudo C_{2v} symmetry). As presented in Figure 3.22, the contribution of each CN^- group to the dicyanamide electronic states is already complex but their contribution to the overall density of states can be still traced back to group components. In fact one can imagine that all the molecular orbitals can be derived from CN^- electronic states which are now mixed with those of the central N and are labelled now as 2pπ or 2pσ. In the solid all these energetic levels (orbitals) will transform into bands accounting for the symmetry and periodicity of the solid.

The other building blocks of the investigated samples are the transition metal ions M^{2+}. They are placed in an axially distorted octahedral geometry given by nitrogen atoms. The electronic configuration of transition metal ions is schematically represented in Figure 3.23 for several ligand geometries. In octahedral environment O_h (sixfold coordinated) the crystal field reduces the degeneracy of the fivefold degenerated atomic d level (see for example [155]) which then splits into a threefold and a twofold degenerate states. The electrons on the threefold degenerate state are designated as t_{2g} (*Mulliken* notation) or d_ε (*Bethe* notation) electrons. The electrons

[10]Please note the different energy scales for the atoms and CN^- group.

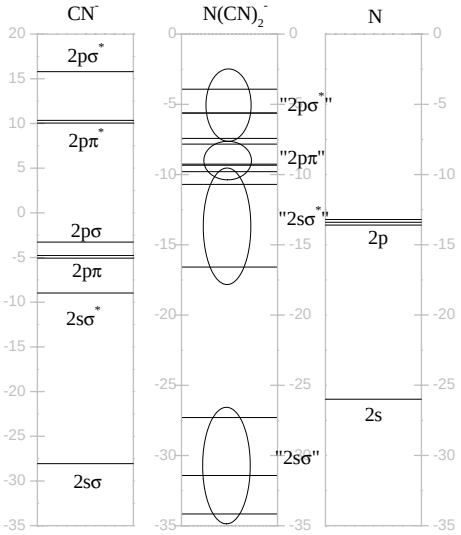

Figure 3.22: Schematic representation of the dicyanamide electronic structure.

corresponding to the twofold degenerate state are denoted as e_g (*Mulliken*) or d_γ (*Bethe*). The symmetry of these states implies that t_{2g} triplet corresponds to the d_{xy}, d_{yz} and d_{zx} atomic orbitals while the e_g doublet transform as the $d_{x^2-y^2}$ and $d_{3z^2-r^2}$ orbitals. In octahedral surrounding the e_g electrons suffer a greater electrostatic repulsion from the anion than the t_{2g} electrons. The corresponding splitting is generally denoted as $10Dq$. For the M^{2+} cations in dicyanamide materials the high–spin electronic configuration in cubic crystal field is then given by: ${}^6A_{1g}$: $t_{2g}^3 e_g^2$ for Mn^{2+}, ${}^5T_{2g}$: $(t_{2g}^2)t_{2g}^2 e_g^2$ for Fe^{2+}, $(t_{2g}^4)t_{2g}^1 e_g^2$ for Co^{2+}, ${}^3A_{2g}$: $(t_{2g}^6)e_g^2$ for Ni^{2+} and ${}^2E_g$: $(t_{2g}^6)e_g^3$ for Cu^{2+}. The paired electrons which do not contribute to the cation spin moment are indicated in parentheses. For axially distorted octahedra the symmetry is reduced to D_{4h} and the degeneracy is further reduced. The orbitals owing symmetry with respect to the z axis are the separated from the rest. The elongation also leads to a convenient spacial representation of the electronic lobes of each orbital by setting an unique z axis.

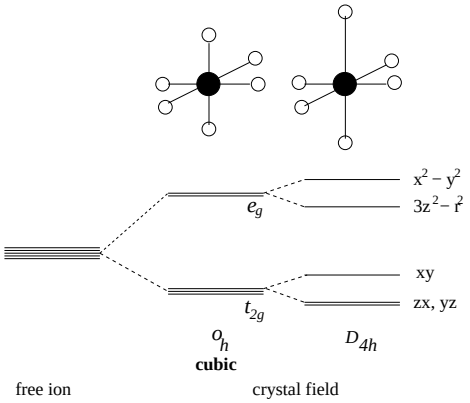

Figure 3.23: Octahedral unit and scheme of the crystal field splitting of the d–states.

Additional to the crystal field splittings presented in Figure 3.23, the magnetic interactions give rise to a spin–up ↔ spin–down separation. This is larger than the crystal field splitting and all the ions are present in a high–spin state.

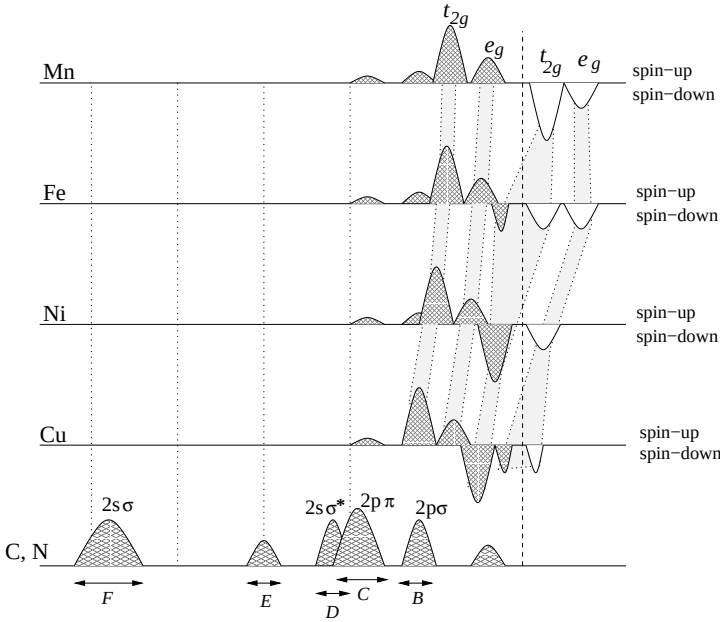

Figure 3.24: Schematic drawing of the electronic structure in dicyanamide materials. The upper four panels show the 3d density of states for the TM metals while the lowest panel indicate the C,N occupied states.

The qualitative distribution of the density of states is presented in Figure 3.24. For the sake of simplicity the O_h notations were still used even for the distorted octahedral symmetry and this convention will be further applied when meaning t_{2g} and e_g–derived bands. In fact the irreducible representation T_{2g} in O_h becomes $B_{2g} + E_g$ in D_{4h} and E_g becomes $A_{1g} + B_{1g}$ under the same transformation.

In the upper panel the Mn 3d states are shown in agreement with the electronic structure calculations presented in [152]. Beside the occupation of t_{2g} and e_g derived bands, some small distributions account for the hybridization in the regions B and C of the valence band i.e. hybridization with the 2pσ and 2pπ derived bands resulting from the dicyanamide groups. Further below (second panel) some spin–down t_{2g} states become occupied for Fe^{2+}. The carbon and nitrogen states are assumed to remain rather unchanged and are thus presented in only one panel for all the compounds. In case of $Ni[N(CN)_2]_2$ and $Cu[N(CN)_2]_2$ the filling of the 3d bands leads to a further occupation of the t_{2g} and e_g spin–down states.

3.3 Analysis of the magnetic superexchange interaction

The state of the art approach of the magnetic interactions in solids is based on complex computational procedures. In an oversimplified picture this follows like this:

one calculates the total energy of the system in the ferromagnetic (FM) and antiferromagnetic (AFM) configurations of magnetic moments and decides which one has the lowest energy. For example this has already been done in case of the $Mn[N(CN)_2]_2$ compound and was shown that the AFM alignment is energetically more convenient [152]. In this section qualitative explanations for the coupling between the magnetic moments will be attempted mainly with respect to the sign of magnetic interactions. The aim is to discern the factors responsible for the tuning of FM configuration for compounds with Co and Ni, while those with Mn and Fe were shown to have a canted AFM alignment. Since the the ferromagnetic coupling is still a exceptional case in the molecular chemistry, the patterns which favor FM alignment are of highly interest.

The sign of exchange coupling along the isostructural series can be generally accounted by two overall factors: the crystal structure and the nature of magnetic ions. The structure conserves the symmetry but is changed in terms of intra–atomic distances and bonding angles along the series. The nature of magnetic ions is first important with respect to the occupancy of magnetic orbitals. On the other hand the above separation into two main factors is arbitrary: the nature of magnetic ions directly influences the crystallographic structure due to the different ionic radii. An example from this point of view was delivered by *Subramanian et al.* on the perovskite $SeCuO_3$ [156]. In this particular case the gradual substitution of Se^{4+} ions (small radius) with Te^{4+} ions (large radius) resulted in a crossover of the magnetic interaction between Cu ions from FM to AFM ground state. The Cu–O–Cu angle was accounted for this change of sign thus resembling the structural tuning factor. In line with these considerations *Kmety et al.* [135] proposed that for the dicyanamide series the responsible factor is of structural nature: the M–C–M angle should changes from 140.4° to 142.6° going from $Mn[N(CN)_2]_2$ to $Ni[N(CN)_2]_2$ and thus a crossover value of 142.0° was extracted for the superexchange (SE) angle. Mn^{2+} has the largest ionic radius in the series while Ni^{2+} has the smallest. No explanation which accounts for the crossover was proposed. Furthermore it remains unclear wether the structure or nature of magnetic ions (or both) are responsible for the above described behavior.

The first step in the analysis of the actual system is to discern for the eligible magnetic interactions. The situation is schematically presented in Figure 3.25 while the corresponding patters can be followed in Figure 3.2 representing the unit cell of the crystal.

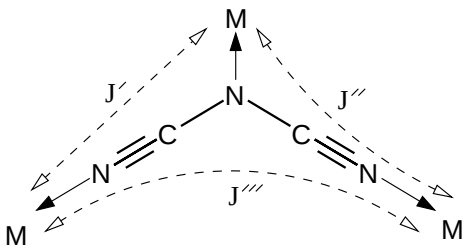

Figure 3.25: Possible magnetic exchange interaction patters in the dicyanamide materials.

The first interaction to be accounted for is the direct metal to metal exchange (J′). The magnitude of J′ depends on the overlap of magnetic d orbitals on TM ions

and appears to be practically zero. This can be estimated by taking into account the distance between cations: the direct interaction coupling rapidly decreases with respect to the inter–atomic spacing. In the cubic TM oxides the atom to next–neighbor distances reach some $5.9 - 6.3$ Å. Consequently the direct exchange interaction is utterly zero (see for example [157] or [158]). For the dicyanamide compounds the situation is similar, the cation–cation spacing (from 5.8 to 6.1 Å) being comparable to the TM oxides. Concluding, the J′ contribution to the exchange will be neglected in the following analysis.

The second and third exchange interactions marked in Figure 3.25 with J‴ and J″ represent indirect or superexchange patterns. In these cases the TM cations are to be regarded as "source" of magnetic moments while the organic species owing filled orbitals provide the exchange paths. In case of J″ the SE pathway corresponds to M–N–C–N–M i.e. middle nitrogen to end nitrogen in the dicyanamide group. For J‴ the SE pathway is given by the end–to–end $[N(CN)_2]^-$ group. As originally proposed by *Anderson* in its *kinetic* form the SE interaction occurs with the excitation of an electron from a bridge–anion orbital into the partially filled d orbital of the TM cation [159–161]. For the case of a 180 degrees cation–anion–cation SE interaction *Goodenough* [162] estimated that a further anion in the bridge would weaken the strength of interaction by about an order of magnitude. These considerations suggest that $J''' \ll J''$ and J‴ can be neglected. A direct corroboration for this assumption was in fact delivered by theoretical calculations [152]. In order to determine the superexchange interaction calculations for the FM ($\uparrow\uparrow$) and AFM ($\uparrow\downarrow$) configurations were performed for the bulk material and embedded cluster models. The 2–unit cluster used is presented in Figure 3.26. It is composed by two $Mn[N(CN)_2]_2$ molecular units, six additional dicyanamide units which account for the octahedral surrounding of each Mn^{2+} ions as well as six sodium atoms on Mn positions in order to achieve overall charge neutrality. Both bulk and cluster calculations indicate that the system in the AFM configuration is favored over FM order with about $18 - 20$ meV per formula unit. Since in the 2–unit cluster there is no end–to–end dicyanamide interaction pathway, this finding actually accounts for the relation $J''' \ll J''$. Another justification is given by the previous studies focused on materials which contain the dicyanamide bridge as SE pathway. In case of the one–dimensional compound presented in [163] the geometry of the end–to–end $[N(CN)_2]^-$ superexchange path is roughly comparable with those in the investigated systems but the bridge is composed by two $[N(CN)_2]^-$ units. The coupling results to be antiferromagnetic ($J < 0$) with a very low estimated value of $0.3 - 0.4$ cm^{-1}. This result practically resembles a system of non–coupled magnetic moments and shows that the the end–to–end $[N(CN)_2]^-$ is a very poor SE mediator[11]. In conclusion, in the following by SE pathway will be referred to the M–N–C–N–M, J′ and J‴ being neglected.

The magnetic interaction between two weakly coupled spins $\vec{S}_A$ and $\vec{S}_B$ localized on the molecular units A and B can be described in terms of spin–only Heisenberg–Dirac–Van–Vleck Hamiltonian:

$$\mathcal{H} = -2J\vec{S}_A\vec{S}_B \tag{3.14}$$

[11] See also the results for the thematically related azido–bridged transition metal complexes [118, 164–167]. The information will be used later in the analysis of the M–N–C–N–C bridges.

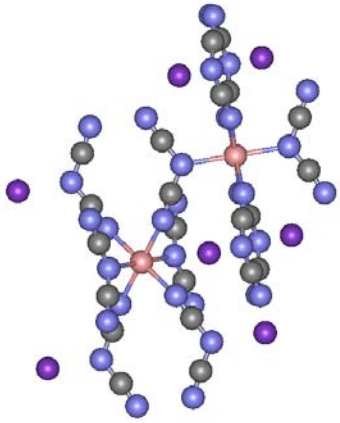

Figure 3.26: 2–unit embedded cluster used for electronic structure calculations of $M[N(CN)_2]_2$ compound.

where J is the single exchange integral. With this sign convention $J > 0$ denotes the ferromagnetic coupling between spins while $J < 0$ stays for the antiferromagnetic coupling. It is worth to notice that the Hamiltonian described in Equation 3.14 is purely phenomenological and leaves out the mechanism of interaction. Denoting by a and b the singly occupied molecular orbitals (SOMOs) on A and B, the exchange coupling constant in a simple Heiter–London model is given by:

$$J = 2\beta S + K \tag{3.15}$$

where:

$$S = \int a\ b\ dv \tag{3.16}$$

is the overlap integral,

$$\beta = \int a\ h\ b\ dv \tag{3.17}$$

is the resonance integral and

$$K = \int a(1)b(2)\ \frac{e^2}{r_{12}}\ a(2)b(1)\ dv \tag{3.18}$$

is the two–electrons exchange integral. The integrals β and S have opposite signs so that their product in negative i.e. antiferromagnetic contribution. The term K is necessarily positive and thus stays for ferromagnetic coupling. Generally $2\beta S$ is dominant and the coupling is antiferromagnetic. From Equation 3.15 it becomes clear which are the conditions to be fulfilled in order to achieve a FM alignment between the spins of units A and B:

(i) the two SOMOs are orthogonal or quasi–orthogonal. This relation leads to the vanishing of the antiferromagnetic term.

(ii) the two electron exchange K is large enough to provide the stabilization of FM alignment. This is achieved when the product ab is large i.e. the overlap density is large in some regions between A and B.

These conditions look apparently simple and should serve as a solid basis for further discussions. However their practical utility is only accidental. The main reason is certainly the construction of proper SOMOs which is usually quite arbitrary. Only if the molecular complex has naturally separated molecular units this approach may represent a worthy practical approach [168]. Secondly, the situation becomes rather complicated if the $A - B$ exchange interaction includes more than two SOMOs. Among the advantages of such orbital approaches, their modelling power is probably the most important. Up to now three main directions may be 'distilled' in the filed of magneto–chemistry: the molecular–orbital model proposed by *Hay et al.* [169], the valence bond model with 'natural orbitals' developed by *Kahn and Briat* [170] and the broken symmetry–model of *Noodleman* [171]. A quantitative comparison of these models can be found in Reference [172]. Even such approaches represent considerable contributions to the understanding of extended SE bridges, their practical applicability is restricted to certain conditions. For the particular case of currently discussed systems they would become so complex that they will certainly lose their appealing features as models.

In order to define the principal mechanism of the antiferromagnetic SE interactions some parameters are essentials. The first is the on–site Coulumb interaction U also known as Hubbard parameter:

$$U = E(\mathrm{d}^{\mathrm{n}+1}) + E(\mathrm{d}^{\mathrm{n}-1}) - 2E(\mathrm{d}^{\mathrm{n}}) \tag{3.19}$$

Another important factor is t_{ij} which represent the hoping–integral between the orbitals i and j. *Anderson* [160, 161] has shown that the virtual hopping of electrons from the diamagnetic bridge to TM cation leads to a lowering of the total energy for the antiferromagnetic state. The kinetic exchange coupling parameter is given by:

$$J_{ij}^{kin} = -\frac{2t_{ij}}{U} \tag{3.20}$$

For usual insulating materials typical values of the transfer integrals t_{ij} are about $0.1 - 0.5$ eV, U has values between 5 and 10 eV and thus the magnitude of J_{ij}^{kin} is situated between -10 and -500 K [173]. For the sake of simplicity, *Anderson* dealt with orthogonal magnetic orbitals and the excited virtual states were derived from their semi–localization. For simple TM oxides the charge–transfer energy Δ must be included in order to get a more rigorous account of the SE mechanisms. This is defined as:

$$\Delta = E(\mathrm{d}^{\mathrm{n}+1}\underline{L}) - E(\mathrm{d}^{\mathrm{n}}) \tag{3.21}$$

In fact in the Anderson mechanism, one starts from the assumption that $U << \Delta$ which corresponds to pure Mott–Hubbard insulators. As evident from the Zaanen–Sawatzky–Allen diagram [144] this is only a particular case. The *Anderson* theory was consequently improved to account for charge–transfer materials and a very good agreement for the Néel temperatures was achieved [174]. In the model proposed by *Anderson* the most important ferromagnetic contribution is the electrostatic exchange interaction also called ferromagnetic potential exchange [160, 161]:

$$J_{ij}^{pot} = \langle ij|ji\rangle \tag{3.22}$$

This contribution is equivalent to the factor K listed in Equation 3.18. Hence, the overall exchange coupling has a form which resembles those of Equation 3.15.

$$J_{ij} \approx J_{ij}^{kin} + J_{ij}^{pot} \tag{3.23}$$

where is was emphasized that only the two main contribution have been so far accounted. Later *Goodenough* [162] and *Kanamori* [175] employed the orbital symmetry and improved the SE model of *Anderson*. They provided semi–empirical qualitative criteria for the sign and strength of SE interaction. They are nowadays known as the Goodenough–Kanamori–Anderson (GKA) rules.

It would be of course desirable to apply the GKA rules for the dicyanamide materials as intended in Reference [135] and account on this way for the AFM–FM crossover. Since the antiferromagnetic contribution could be in principle attributed to SE interaction over the extended bridge, the key of the problem would be the revealing of factors responsible for ferromagnetism. Following the GKA rules this should result from certain symmetry aspects. However such an approach is related to the existence of 180° or 90° cation–bridge–cation interactions which are not present for the current materials. Accordingly the GKA rules deliver no output for the dicyanamide materials. A good example related to this issue might be the compound $CuGeO_3$ presented in [176] where side groups modify the 90° interaction in a consistent way.

The sum of above comments clearly indicates that the analysis of SE interaction in dicyanamide materials certainly request a specific approach. This will be done in the following.

The first step is related to the general accounting of ferromagnetic component of the SE interaction in a kinetic model. Hence the usual employed terms are related to the SE between two half–occupied metal orbitals $J(e,e)$, the SE interaction can also occur between half–filled and empty orbitals $J(e,0)$, one full and one half–filled orbital $J(ee,e)$ and finally one full and one empty orbital $J(ee,0)$. Actually an extended SE model may be build up onto this idea first suggested by *Anderson* [177] and extended by *Goodenough* [162]. The further term of SE interaction arise in higher orders of perturbation theory and their magnitude is lower. For example, the magnitude of $J(e,0)$ interaction is given by [173]:

$$J_{ij}(e,0) = \sum_{j'} \frac{t_{ij'}^2 I_{j'j}}{U^2} \tag{3.24}$$

where $I_{j'j}$ is the intra–atomic exchange integral. This SE mechanism accounts for a ferromagnetic contribution and can be quite efficient when the electron transfer into empty shells is strong. Since the I/U ratio is roughly 0.1, the $J(e,0)$ interaction can reach about $10-20\%$ of the conventional kinetic exchange. In a series of papers, *Weihe* and *Güdel* discussed on the problem of SE interaction and suggested some trends [178–181]. They shown than the intra–atomic exchange integrals are in general proportional to the number of unpaired electrons of on the metal ion: $I_n = nI$, where it was generally assumed that the mentioned exchange integral is the same for all orbitals. Additionally they parameterized all the possible SE contributions and by

assuming realistic values of the parameters they show that their magnitudes generally obeys:

$$|J(e,e)| > J(e,0) \gg J(ee,e) > |J(ee,0)| \tag{3.25}$$

Thus, while $J(e,e)$ and $J(ee,0)$ resemble antiferromagnetic contributions, the values of $J(e,0)$ and $J(ee,e)$ are positive. An overall AFM interaction can then arrive in the frame of kinetic model when $J(e,e)$ is zero or very small and $J(e,0)$ or $J(ee,e)$ becomes dominant. Moreover, since the late TM ions have no unoccupied 3d orbitals, in the frame of kinetic SE model the only possible ferromagnetic contribution results from $J(ee,e)$.

The second step of this analysis deals with the description of the SE interactions for dicyanamide materials based on the information gathered on the electronic structure. There are two main SE paths in the electronic structure of the dicyanamide bridge: the 2pσ and 2pπ derived orbitals. The efficiency of each path may be described as being dependent on two factors: the energy difference to the levels of 3d cation and their reciprocal overlap. The first factor can be evaluated from the valence band studies. Its physical meaning may be understood in terms of virtual hopping as originally proposed by *Anderson*: a large energy difference implies a low hooping efficiency and thus a weak SE interaction. The second factor is more complex and cannot be unambiguously defined. Some recipes for simple structures can be followed in frames of the *angular overlap model* [182–184]. Consequently the strength of each path will be described in terms of a co–valency parameter like:

$$\lambda = \frac{\langle bridge|\mathcal{H}_{eff}|metal\rangle}{E_{metal} - E_{bridge}} \tag{3.26}$$

where *bridge* and *metal* represent the orbitals of the dicyanamide group and TM ion which are responsible for the SE magnetic interaction. This equation actually includes the factors relevant for the evaluation of the transfer integrals t_{ij} in Equation 3.20.

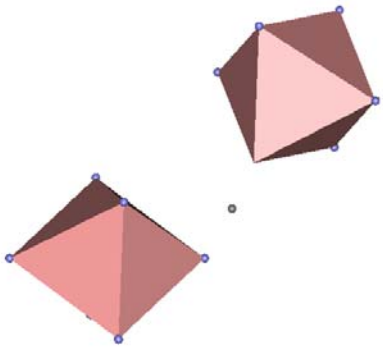

Figure 3.27: Cluster used in the discussion of superexchange interaction.

For simplicity only two hexa–coordinated M^{2+} ions will be considered as previously considered for the cluster calculations (Figure 3.27). This cluster seems to be sufficient for the description of sign and magnitude of magnetic interaction as shown for $Mn[N(CN)_2]_2$ [152]. The N atoms situated on the local axis of symmetry of distorted octahedra are denoted with N_t while those in the basal plane of

bi–pyramides are denoted with N_b. With this notation the SE pattern is written as $M^{2+} - N_t - C - N_b - M^{2+}$. In the series the $M^{2+} - N_t - C$ angle is about 120° and the $C - N_b - M^{2+}$ about 175°. Because of this geometry not all the SE mechanisms are equally favored.

Let us take the virtual hopping of a e_g electron from the $d_{3z^2-r^2}$ orbital on the SE path given by the 2pσ orbital. It is acceptable to imagine the lobes of the 2pσ orbital of the dicyanamide group to be oriented along $N \equiv C - N - C \equiv N$ or, in other words, along $N_t - C - N_b$. Thus the $M^{2+} - N_t - C$ fragment represents an effective metal $d_{3z^2-r^2}$ to bridge 2pσ overlap. On the contrary, the $C - N_b - M^{2+}$ results in a reduced $d_{3z^2-r^2}$ to 2pσ overlap in the second MN_6 rhombus–shaped unit. Both consideration make use of the orientation of $d_{3z^2-r^2}$ orbital along the symmetry axis of structural bi–pyramides. In spite of this, the $C - N_b - M^{2+}$ may be characterized by an effective overlap between the bridge 2pσ orbital and t_{2g} orbitals in the array $C - N_b - M^{2+}$. It takes into account the orientation of the t_{2g} electronic lobes in the basal plane of bi–pyramides. This means: the geometry of the bridge and its relative spacial orientation to the MN_6 units lead to a dumped down $e_g \leftrightarrow e_g$ magnetic SE but to an effective $e_g \leftrightarrow t_{2g}$ SE when accounting for the 2pσ bridge orbital. To be noticed is that, for the sake of simplicity, the labels specific for the octahedral symmetry were still used even the MN_6 exhibit an axial distortion (see previous section).

For the above considerations the virtual hopping from a 3d ion to the neighboring nitrogen atoms was considered to be equivalent to the metal to dicyanamide hopping. This is reasonable since the distance between magnetic ions is comparable to those of the simple metal ions even the bridge is now formed by three instead of one diamagnetic atom.

Analogous, the SE effectiveness of 2pπ orbital can be discussed. The electronic lobes of this orbital can be considered to have mirror planes perpendicular to $N \equiv C - N - C \equiv N$. As discussed above for the Equation 3.27, the terms to be considered are overlap and energy difference between orbitals. A glance on Figure 3.20 reveals in the case of $Mn[N(CN)_2]_2$ a 3d metal to 2pπ energy difference of ≈ 5.5 eV. This value enters the denominator in Equation 3.27. For the 2pσ SE path the corresponding value is about 3 eV which means a two times lower magnitude. Additionally the overlap of the 2pπ orbitals to that of 3d ion can be considered to obey [184]:

$$|e_\sigma| > |e_\pi| \tag{3.27}$$

where e_{orb} denotes the metal–to–ligand interactions. The sum of these aspects suggest that the strength of the 2pπ SE path can be considered to be low when compared to 2pσ and will be neglected in the following analysis.

Let us now apply the above considerations for the cases of compounds with Mn and Ni. The choice is motivated by the fact that Mn^{2+} has all the 3d orbitals half–occupied while Ni^{2+} has full t_{2g} orbitals and half–occupied e_g orbitals. Thus, for $Mn[N(CN)_2]_2$ the $e_g \leftrightarrow t_{2g}$ SE interaction represents a $J(e,e)$ interaction, which is negative. On the contrary, for $Ni[N(CN)_2]_2$ the $J(e,e)$ is dumped down by the bridge geometry and $e_g \leftrightarrow t_{2g}$ magnetic SE is reduced to $J(ee,e)$, which is positive. The situation for the compound with iron is intermediate but since two t_{2g} electrons may still interact in SE terms with two e_g electrons, the $J(e,e)$ interaction is still dominant.

For the case of composition with cobalt[12] the occupancy of t_{2g} is higher and it seems like $J(ee, e)$ becomes dominant and the classic SE is suppressed.

Some additional aspects are to be elucidated. The first is related to the physical meaning of the above consideration. Namely, if correct, such an approach should be also valid for other types of compounds. Indeed, the ferromagnetic nearest–neighbor interaction in NiO can result from co–valency effects as proposed in [145, 185]. This happens if the half–filled e_g electrons and the filled t_{2g} electrons on the nearest–neighbor ion are responsible for SE interaction, which is really the case according to the geometry of the ligand orbitals. Moreover, one can also account for the magnitude of the 90° covalent SE in NiO [181]. Hence the above mentioned approach leads to a similar result as expected from the potential exchange and may be considered as an alternative approach.

The second aspect is the evaluation of the coupling constant magnitude which is done is the following for the compound containing Ni. The ferromagnetic contribution $J(ee, e)$ has a form similar to that of $J(e, 0)$ (see Equation 3.24). The values of $t_{i,j}$ can be extracted from the parameters used in the simulation of 3s–splitting (see References [174, 186]). With $t = T^2/\Delta$ where $T \approx 0.9$ eV, the redefined SE value of the Hubbard energy $U_{SE} \approx 10$ eV [174], $\Delta \approx 3$ eV, $I = nI_0 \approx 0.4$ eV with $I_0 \approx 5000$ cm^{-1} [178] and $n = 2$ the number of unpaired spins, the exchange coupling constant becomes:

$$J = 2\left(\frac{T^2}{\Delta}\right)^2 \frac{I}{U^2} \approx 6 \cdot 10^{-4}\,\text{eV} \tag{3.28}$$

Equation 3.28 uses the redefinition of electronic structure parameters for the purpose of superexchange interaction evaluation as proposed in [174] since the Racah parameters cannot be neglected. Once again, the above value is comparable with the expectation for simple transition metal oxides but this is acceptable since the M–M distances are comparable even for different number of atoms in the SE bridge.

At the ordering temperature the thermal energy equals the magnetic ordering energy. In a simple molecular field model the coupling SE constant is related to the ordering temperature as:

$$T_c = \frac{2JzS(S+1)}{3k_B(2S)^2} \tag{3.29}$$

where z is the number of TM neighbors ($z = 8$ in this case) and S is the cation spin ($S = 1$ for Ni^{2+}), $k_B = 8.61 \cdot 10^{-5}\,\text{eV}\,\text{K}^{-1}$ is the Boltzmann constant. We obtain a value $T_c \approx 20$ K. This estimation is of course accidentally when compared to the measured value of 21 K since physically reasonable estimations were used. However it clearly indicates that the order or magnitude of a few tens of kelvin is correct.

Since for $Ni[N(CN)_2]_2$ the occurrence of the FM alignment can be explained on this baseis, for the other compounds some trends can be indicated. So it is expected that the strength of AFM ordering to be lower for $Ni[N(CN)_2]_2$ as compared to $Mn[N(CN)_2]_2$ since SE between half–filled orbitals is reduced according to the 3d occupancy. For $Co[N(CN)_2]_2$, even the $J(e, e)$ is expected to have a non–negligible value, the $J(ee, e)$ type SE becomes dominant. Furthermore the ordering temperature

[12] This compound was not included in this work but is mentioned at this point for a more general view.

of $Co[N(CN)_2]_2$ is expected to be lower than that specific for $Ni[N(CN)_2]_2$, which is experimentally supported by the lower ferromagnetic Curie temperature.

Concluding, based on the electronic structure information, we propose that the AFM–FM crossover is due to the occupancy of the 3d orbital i.e. the nature of TM ion. The geometry is responsible for the particular pattern of the SE interaction but the changes in bounding angles cannot account for the trigger of ferromagnetic coupling. With these consideration, the crossover angle mentioned in [135] looses any physical meaning.

Besides the sign of SE magnetic interactions, some other aspects of the magnetic behavior are still to be elucidated. Among them the most important are the anisotropy and the small canting of AFM structures. Although general applicable mechanisms can be proposed [135], only some hypothesis can be stated without a corresponding computational approach.

3.4 Conclusions

Investigations on the electronic structure of materials with the $M[N(CN)_2]_2$ general formula with M = Mn, Fe, Ni, Cu, revealed that they can be regarded as intermediate step between free molecules and solids with long order interatomic interactions. In a combined XPS/XES study it was possible to account for the organic and TM contributions in the valence band region. This information was used to analyze the sign of magnetic superexchange interaction. Particular structural factors and the nature of magnetic ions were found responsible for the occurrence of ferromagnetic interaction. The validity of this result was underline by the correct estimation of the order of magnitude for the ferromagnetic ordering temperature.

XPS core–level studies revealed that for M = Mn, Fe the 3s multiplet splitting can be employed as spectroscopic tool. For compositions with M = Ni, Cu this can be done only after accounting for the magnitude of the screening effects. This was performed in frame of an appropriate model for the 3s multiplet splitting in insulators and employing a novel numerical procedure.

The presented study certainly generally opens the perspective for the same kind of investigations for other metal–organic compounds or particular molecular magnets. This is necessary since the computational approach to this class of materials is still on a challenging level. Several prerequisites are to be accounted. The first is related to the nature of the sample. XPS measurements request UHV conditions and thus any sample must keep its molecular structure even at very low pressures. Samples containing water or other in UHV volatile groups must be carefully handled since they may collapse and loose their structure. Measurements at low temperatures including entry–sample configurations at same condition could serve as alternative. Additionally the chemical and crystallographic structure of the samples must be always checked when the chemical stability is questionable. Further kinds of measurements like the use of circular dichroism (XMCD) may be regarded as potential and highly valuable experimental tools for this class of materials.

Chapter 4

Six–membered 'ferric wheel' molecule

Ring–shaped clusters with even number of transition metal ions per molecular unit have gained a lot of attention as attractive models for one–dimensional magnetic materials and for the investigation of interacting metal ions at the simplest level. In contrast to the 3d metal–organic compounds presented in the previous chapter, these molecule–based materials are characterized by a particular crystallographic structure: the magnetic ions in the cluster are surrounded by a organic 'crown' which makes the inter–cluster distances to be high on atomic level. Thus, the inter–molecular magnetic interactions are utterly negligible and the magnetic behavior is given only by magnetic interactions inside the cluster. The synthesis and magnetic properties for such cyclic clusters containing $6 - 18$ Fe^{3+} ions have been reported (see [117, 187, 188] and the references therein).

A few years ago hexanuclear clusters containing an alkali ion (Li or Na) were reported [189, 190]. The alkali ion placed in the center of a hexagonal wheel formed by Fe^{3+} ions plays an important role in stabilizing the structure and influences the Fe–O–Fe angles [187, 189]. The $S = 5/2$ spins are coupled antiferromagnetically in the sense of a negative exchange coupling constant. The magnetic coupling results in a total cancellation of the spins and gives a $S_{tot} = 0$ ground state. This aspect does not alter the attractiveness of these materials: they are appealing models for the basic theories of magnetism as spin–dynamic models [187, 191–194] and exhibit novel types of magnetic behavior [195].

From the specific point of view of electronic structure and magnetism, the mentioned clusters have a special relevance due to the oxo–bridged magnetic 3d ions. This issue is a long standing problem of the magneto–chemistry, most of the studies being focused on metal dimers (see for example Reference [118]). Among them, the Cu^{2+} dimers received a higher attention since each of the ions has only a singly occupied magnetic orbital and additionally it was shown that simple valence bond models are enough for a qualitative and roughly quantitative approach [118, 169]. The kernel of all these studies is practically the investigation of the magneto–structural effects i.e. the dependence of the sign and strength of magnetic exchange coupling on the distances and angles of the path of interaction. Various complexes resembling oxo–bridged Fe^{2+} dimers were also reported in the literature, an exhaustive review being

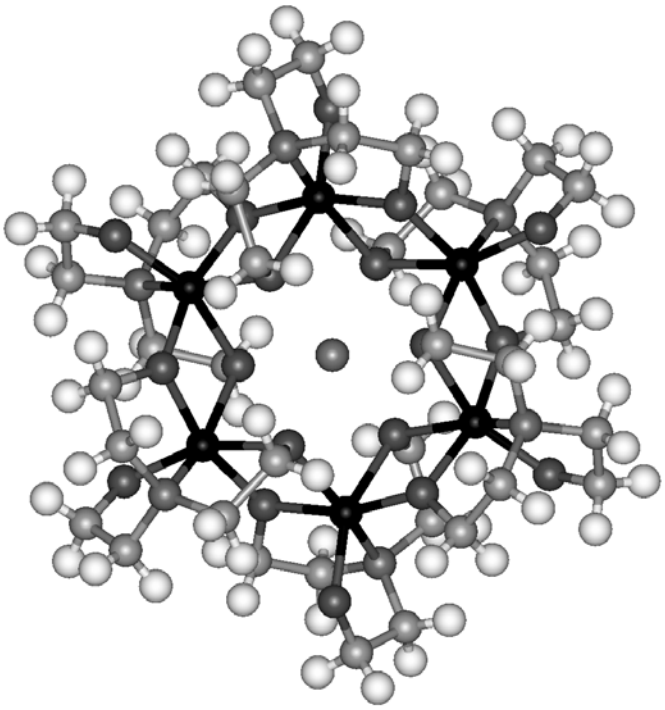

Figure 4.1: A 'ferric–wheel' molecule with six oxo–bridged Fe^{3+} ions (black atoms). In the center of the molecule an alkali ion is placed. The O atoms are depicted as dark grey spheres while N and C atoms are represented by light grey spheres. The white spheres represent H atoms.

presented in Reference [196]. In [187] it was shown that changes in the bridging Fe–O–Fe angle results in changes of the exchange coupling. From computational point of view such molecules are a difficult challenge due to their high number of atoms in molecule (over 100), their low symmetry and due to the fact that Fe and H atoms are present. Computational approaches are usually expensive and time–consuming, simpler but reliable solutions being developed. Once again, experimental investigations are requested to discern about their quality.

In an analogous manner to the previous chapter, specific experimental techniques were employed for the study of electronic structure. The aim of this study is to get an experimental description for the electronic structure of a hexanuclear iron ring and to employ the gained information together with theoretical results in order to elucidate specific questions related to the magnetic properties.

The present work was performed on samples having the following chemical composition: $Li \subset Fe_6[N(CH_2CH_2O)_3]_6Cl \cdot 6CHCl_3$. The samples were synthesized in the group of Prof. Dr. Rolf W. Saalfrank[1] [189, 190] and were kindly made available to us.

[1]Actual address: Institut für Organische Chemie der Universität Erlangen–Nürnberg, 91054–Erlangen, Germany

4.1 Studies on the electronic structure

The experimental results are briefly presented in this section emphasizing on the main features. Detailed comments of each experimental finding will be presented in the section dedicated to discussions.

4.1.1 Sample and specific experimental details

Single crystals of Li $\subset Fe_6L_6Cl{\cdot}6CHCl_3$ with L = $[N(CH_2CH_2O)_3]$ were drained in UHV conditions in a small gold crucible. As previously described [187] the hexagonal unit cells ($R\overline{3}$ space group) are preserved upon drying but the lattice parameters a and b are reduced by about 30%. The conservation of the molecular structure in UHV conditions is an important advantage.

Because of the insulating properties of the sample, charge neutrality on the surface was achieved during XPS measurements by using a low–energy electron flood gun. Precautions were taken in order to monitor possible changes of the surface quality when recording spectra. A detailed study of the surface damages induced by the X–rays was performed for more than 48 hours and only after $12-14$ hours some changes in the spectra became visible. These changes were not necessarily due to radiation damages, another possible factor being the usual covering of the surface with carbon arising from the rest gas in the main chamber. The recording time of the presented spectra was less than 8 hours.

For the XAS/XES spectra, crystalline powder was poured on a conductive carbon adhesive band. Each spectrum was recorded on a different point on the sample in order to avoid possible artefact features resulting from the sample damage through the synchrotron radiation. For some of the incident energies the spectra on the same point were repeated in order to ensure the repeatability. For all types of measurements, the way the calibration of the spectra was performed is indicated in text.

4.1.2 XPS 1s core–level spectra of C, N and O Calibration

Since the neutralizer was used during the XPS measurements, the calibration of the spectra has been performed with reference to a known peak. However, more non–equivalent positions for carbon atoms can be discerned in the chemical formula and thus no fully unambiguous calibration receipt can be proposed.

The calibration was performed by comparing the C 1s spectrum with the reference binding energies of carbon for C^* in $CH_2-C^*H_2-O$ at 286.35 eV (PTMG from [141]) and $CH_2-C^*H_2-NH$ at 285.65 eV (PEI from [141]). It was assumed that the contribution from adsorbed carbon is low and a fit with two peaks with equal areas was performed assuming a 0.8 eV binding energy difference as constrain condition (see Figure 4.2). Symmetric Lorentz functions were considered for the shape of each peak as well as a convolution with a 0.6 eV Gauss line simulating the apparatus broadening. Due to the calibration the determination of absolute binding energies implies a lower resolution and the magnitudes indicated in text should be regarded as having only an approximate value.

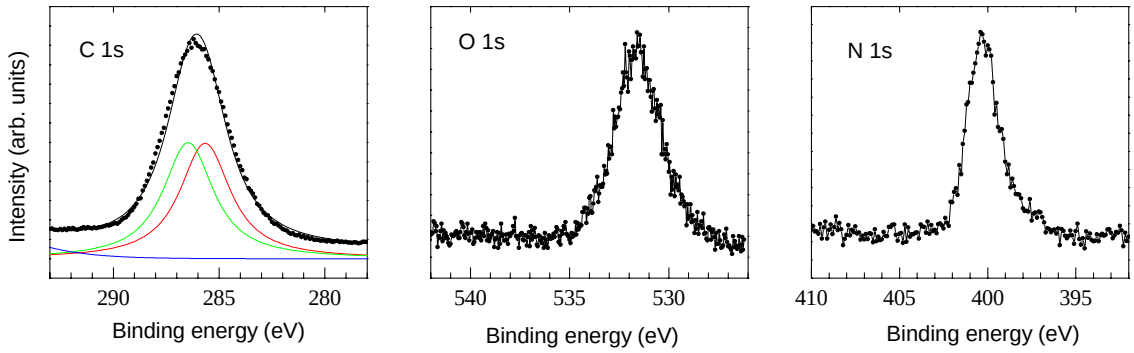

Figure 4.2: XPS 1s core–level line of carbon (left), oxygen (middle) and nitrogen (right panel) recorded for the 'ferric–wheel'.

In Figure 4.2 the XPS 1s signals of oxygen and nitrogen are also presented. As expected for a polycrystalline sample and due to the use of neutralizer, the width of the peaks at the half maximum intensity is rather high. It does not allow the full employment of the resolving power specific for the experimental setup. The maximum of the N 1s peak is positioned at about 400.3 eV while the oxygen spectrum exhibit a maximum at about 531.6 eV.

4.1.3 Iron XPS core–level lines

The partial occupied 3d sub–shell of the iron ions is responsible for the spin magnetic moments and thus the study of the electronic properties were focused on the ion lines.

As discussed in Chapter 3, for insulating materials the XPS spectra of TM ions are a sum of ion specific and material specific features[2]. However, for ions having electronic structures close to a half–filled sub–shell like Mn^{2+} or Fe^{2+} the final state screening effects are expected to be low and to change the intrinsic TM ion spectra to a lower extent than for the late 3d metals.

The Fe 2p lines recorded for Li $\subset$ $Fe_6[N(CH_2CH_2O)_3]_6Cl$ are plotted in Figure r4.3 along with those of $LiFeO_2$ (from [197]) and FeO (from [51]). The formal valence state of iron is 2+ in FeO and 3+ in $LiFeO_2$.

Below each line of the spin–orbit components a satellite is visible for all the cases and it corresponds to the final states with charge transfer contribution. The intensity and binding energy difference to the parent line are however different. For the two cases of $LiFeO_2$ and FeO this difference can be explained in simple terms: while going from a 2+ to a 3+ formal valence state it becomes more difficult to transfer electrons from ligand to the 3d ion i.e. the charge–transfer energy Δ is larger. In contrast to this trend, for the hexanuclear cluster the binding energy difference between main line ($2p^5 3d^n L$) and charge transfer satellite ($2p^5 3d^{n+1}\underline{L}$) is lower and comparable to FeO. The expected valence state of iron in the 'ferric–wheel' is 3+ [187, 189]. This rather unexpected finding reiterates once again that screening effects in the final state of

[2]Please see Chapter 3 for detailed discussions.

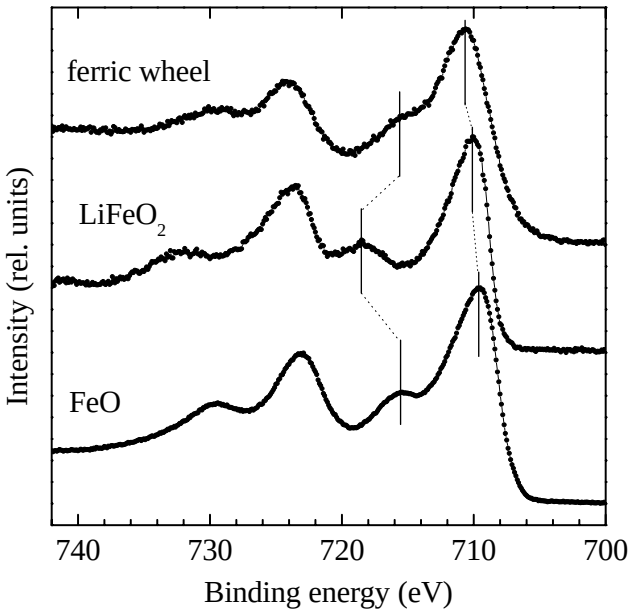

Figure 4.3: XPS 2p core–level line of iron recorded for the 'ferric–wheel', $LiFe^{3+}O_2$ and $Fe^{2+}O$.

photoemission are due to both nature of TM ion and configuration of ligand atoms. These two aspects have to be carefully investigated before dropping any conclusion.

The binding energy of the main line (710.6 eV), mainly corresponding to $2p^5 3d^n L$ final states, is higher than the position for other materials presented in Figure 4.3. According to the distribution of Fe $2p_{3/2}$ binding energies in different iron compounds (709.6 eV [51] or about 709.3 eV [147] in FeO, $\sim$ 710.7 eV in $FeCl_2$ [147]), the position of the main line resembles a formal trivalent valence state or divalent ions in a compound with higher degree of ionic character.

The multiplet spitting of the 3s core–level line of iron is plotted in Figure 4.4. The experimental spectra were fitted with Lorentzians and were corrected for the background arising due to secondary electrons using the Tougaard procedure. This was done in order to allow the comparison with the lines of $LiFeO_2$ and FeO (from [51, 148]). In the case of the Fe 3s spectra of the ferric–wheel and FeO, three peaks can be distinguished and a number of three peaks were used simulating the experimental spectra. For $LiFeO_2$ only two peaks have physical meaning in the spectrum [148] and thus, only two were considered for the fitting procedure. Only the two main peaks are marked in Figure 4.4. As presented in Section 1.1.2.7 and illustrated in the previous chapter, the splitting of the 3s core–level line originates from the exchange coupling between the 3s hole and the 3d electrons. The value of this splitting is about 6.5 eV for Fe^{3+} and about 5.5 eV for Fe^{2+} in simple iron oxides. The distance between the two main peaks in the 3s XPS spectrum of the 'ferric–wheel' was found to be 5.6 eV. Such position for the second peak would correspond, by simple comparison, to a 2+ valence state. However, the magnetic properties of the sample can be well described by taking account a $3d^5$ configuration for iron in the ground state. Thus, the interpretation of the 3s spectrum should be in principle consistent with a formal $3d^5$ electronic

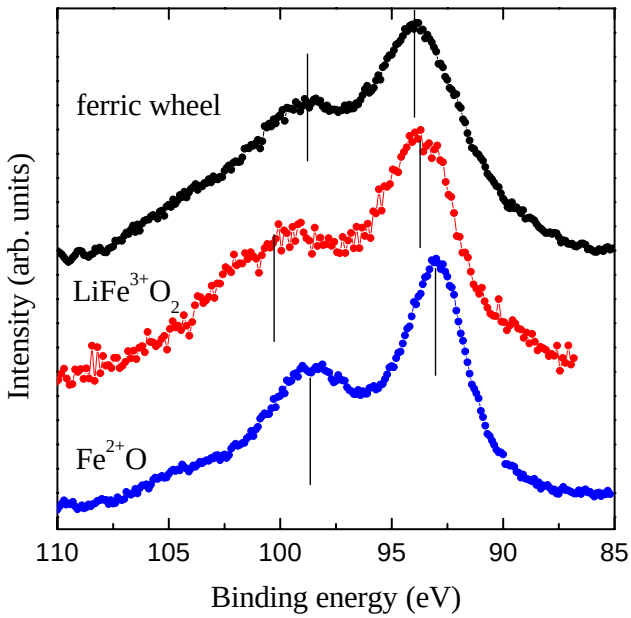

Figure 4.4: Multiplet splitting of the XPS 3s core–level line of iron recorded for the 'ferric–wheel', $LiFe^{3+}O_2$ and $Fe^{2+}O$.

configuration. We interpreted this as an interplay between the intrinsic multiplet splitting and the charge transfer parameters [198]. This aspect will be discussed later along with additional spectroscopic data and electronic structure calculations.

4.1.4 Valence band region

The XPS spectrum of the valence band region is plotted in Figure 4.5 along with the element selective emission spectra of iron and oxygen. The calibration of the XES spectra was performed by recording the reference lines of a pure iron sample (Fe L_α edge at 705.0 eV [199]) and MgO (O K_α edge at 525.0 eV [200]). The emission spectra were located in the valence band region by accounting for the proper XPS binding energies of the core–levels (531.6 eV for O 1s in Figure 4.2 and 710.6 eV for Fe $2p_{3/2}$ in Figure 4.3). Series of different excitations energies were recorded for each edge but no relevant features were visible. Therefore they are not listed here.

According to the shape of the emission spectra the maximum at about 6 eV binding energy in the shape of the XPS VB spectrum mainly corresponds to the Fe 3d4s states. The O 2p states, whose contribution is visible in the O K_α spectrum, are located relatively in the same region. Their maximum is positioned at about 7 eV binding energy. This indicates a strong hybridization between the O 2p and Fe 3d states. The states giving rise to maxima around 18 and 25 eV binding energy are most probably 2s contributions from C, N and O. However because six elements are present in the sample, only hints concerning each contribution to these features can be formulated.

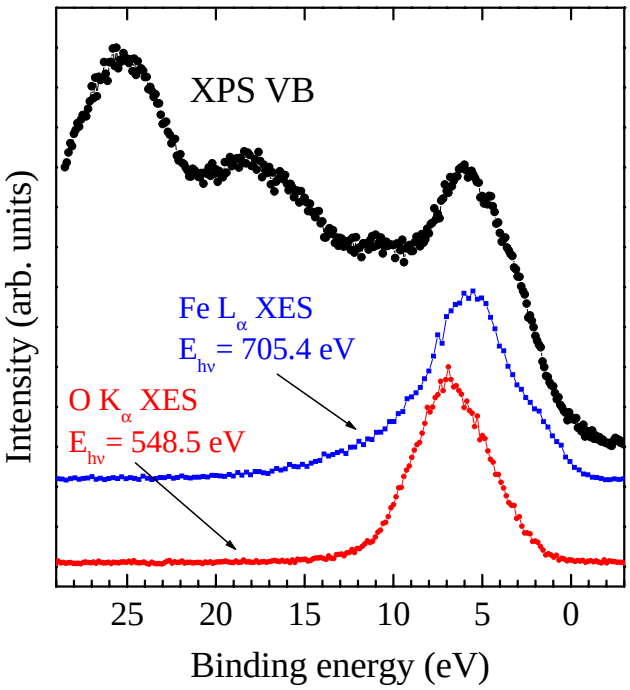

Figure 4.5: XPS valence band spectrum of Li $\subset$ Fe_6L_6Cl with L = $[N(CH_2CH_2O)_3]$ and along with element sensitive XES spectra of iron and oxygen.

4.2 Computational results

Electronic structure calculations for the 'ferric–wheel' have been performed by Dr. Andrei V. Postnikov[3] using the SIESTA method [201]. This computational method implies norm–conserving pseudopotentials and localized basis of numerical orbitals. Exchange correlation was treated within the Kohn–Sham density functional theory (DFT) in either the local spin density approximation (LDA) or generalized gradient approximation (GGA). Up to now only collinear magnetic density can be considered. As mentioned before, the actual magnetic structure resembles a non–collinear antiferromagnetic coupling. However, the sign and magnitude of exchange coupling constants is expected to be reproduced when the canting angles are relatively low. A single molecule consisting of 140 atoms (see the chemical composition) was considered in a $22 \times 22 \times 18$ Å box. The slow convergency of the self–consistent cycle can be improved by broadening the energy levels with en 'electronic temperature'. The calculations were performed for both ferromagnetic and antiferromagnetic configurations of magnetic moments.

The results show that the AFM alignment of spins is energetically favored and the AFM configuration thus represents the ground state of the magnetic spin system. The 4s contribution to the overall DOS is very low. In Figure 4.2 is plotted the position projected DOS for two neighboring iron atoms in the AFM pattern. The same contribution but in the FM configuration is plotted in right panel of Figure 4.2.

Independent on the choice of spin alignment, each iron atom seems to have a

[3]Actual address: Fachbereich Physik, Universität Osnabrück, 49069–Osnabrück Germany

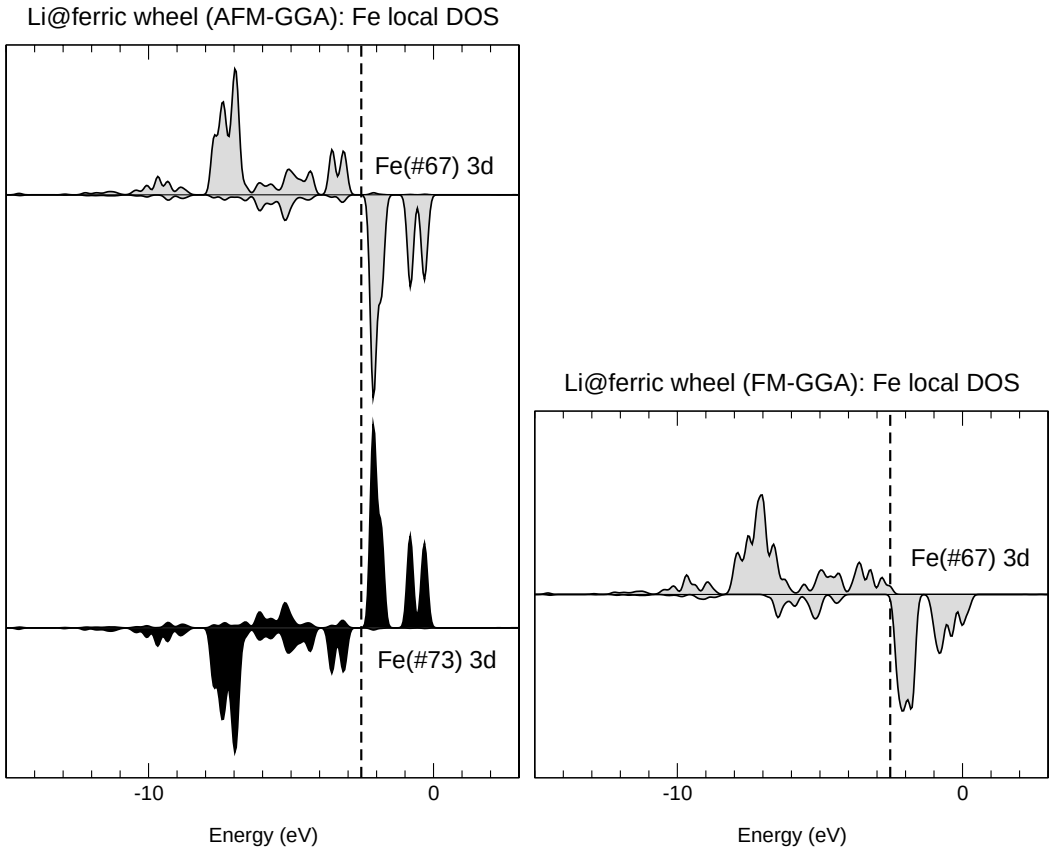

Figure 4.6: Broadened iron projected density of states calculated for the 'ferric–wheel' in the antiferromagnetic (left panel) and the ferromagnetic configuration (right panel).

spin $S = 2$ which differs from the expected $S = 5/2$ magnitude from magnetic measurements [187]. In spite of this, for the FM configuration the total spin of the molecule is $S = 15$ which actually corresponds to a $S = 5/2$ spin assigned to each iron atom. The difference of $S = 1/2$ is due to a magnetic moment induced on the 2p states of oxygen in the oxo bridge.

The convergence to the same local magnetic moment in both AFM and FM configurations is reflected in Figure 4.2: the bands are marked by relatively similar distributions of the DOS. A maximum of the Fe 3d states can be observed about 5 eV below the Fermi level as well as a sharper peak of unoccupied states just above E_F. Most of the minority density of states remains unoccupied on each iron position. The only major difference is visible at the Fermi level. For the AFM type of calculations a small gap separating the occupied and unoccupied states is present while the FM result is marked by a non–zero density of states at the Fermi edge. To be noticed is that no intra–atomic correlations were considered (no Hubbard U contribution). Additionally the canting of the AFM structure was not considered.

The element projected DOS allows the identification of all structure visible in the XPS spectrum listed in Figure 4.5. A good agreement was found for the O and Fe partial DOS compared to the emission data. Thus the maximum at 6 eV BE is due to Fe 3d and O 2p states. At about 11 eV the N and C 2p states are visible while

the C 2s and N 2s contributions can be found at 15 and respectively 18 eV. The peak visible in the XPS VB data at 25 eV is mainly due to the O 2s states.

4.3 Discussions

The Fe 3s and 2p photoelectron spectra show features which are uncommon for the 3s and 2p spectra of transition metal oxides. In opposition to the expected trend for the formal valence state, the 3s core–level spectrum shows a multiplet splitting which resembles a 2+ formal valence state instead of the expected 3+ value, as deduced from magnetic results [187]. This can be explained by a consistent interpretation of the 2p and 3s core–level data recorded for Fe. The Fe 2p spectrum presents a charge transfer satellite which is closer to the main line than the similar features in $LiFeO_2$ or FeO. It suggests that the energy difference between final state with of without charge transfer is low which probably corresponds to a relative low charge transfer energy. For the iron 3s line this effect of co–valency can lead to an overlap between the low–spin final state without ligand hole and charge–transfer features of the main line. The result is a 'visible' 3s multiplet splitting which is reduced over the value expected from the valence state.

An alternative explanation of this problem can be stated on the hypothesis that the 3s multiplet splitting reflects only the local values of spin magnetic moment. Based on the computational results, this rather corresponds to a 2+ real valence state of the iron ions.

One common problem occurred during the computational approach was the extremely bad convergency. This was treated by broadening the energy levels with 'electronic temperatures' of 600, 400 and 200 meV. Unfortunately for both LDA and CGA calculations the total energy results and magnetic moments obtained were dependent on the value of broadening which suggest that these values are not fully reliable.

Even under these circumstances, one can still get the order of magnitude for the exchange coupling constant between two iron ions. Assuming the interaction between the next neighbor rigid spins, the Heisenberg hamiltonian can be written as:

$$\mathcal{H} = -\sum_{i \neq j} J_{ij} \mathbf{S}_i \mathbf{S}_j \tag{4.1}$$

Then from the energy difference between the FM state $E_{\mathrm{FM}} = -6\,J\,S^2$ and the AFM state $E_{\mathrm{AFM}} = +6\,J\,S^2$ one can still evaluate the order of magnitude for the exchange coupling constant:

$$J = \frac{1}{12\,S^2}\,\Delta E \tag{4.2}$$

The energy difference obtained from the LDA calculations is $\Delta E^{\mathrm{LDA}} = 439$ meV which leads to an coupling constant $-J^{\mathrm{LDA}} = 9.14$ meV $= 106$ K. For the GGA results the obtained values are $\Delta E^{\mathrm{GGA}} = 705$ meV and $-J^{\mathrm{GGA}} = 14.7$ meV $= 170$ K. The experimental deduced value is 18–20 K (1.55–1.75 meV) [187]. The difference to the experimental value can be explained by the intra–atomic correlation U which

was not considered in these calculations; it tends to reduce the calculated exchange parameters.

A better convergency can be accomplished if fix spin moments calculations are performed. The broadening 'electronic temperatures' can be reduced to 15 meV without to affect the convergency. Taking, for example, the energy differences between the calculation with 30 μ_B and 20 μ_B fix spin moment per formula unit, an exchange coupling constant of $-J = 7.32\,\mathrm{meV} = 85\,\mathrm{K}$.

4.4 Conclusions

We report on new spectroscopic data of the six–membered 'ferric wheel' molecule. The multiplet splitting of the 3s XPS core–level recorded for Fe suggest a 2+ formal valence state for these ions. The deviation from the 3+ state obtained from magnetic measurements can be explained by accounting for the charge–transfer effects. One can conclude, that the relaxation effects in such organo-metallic systems could lead to consistent changes of the photoelectron lines of the metallic ions. Additionally, electronic structure calculations revealed a $S = 2$ spin on iron positions, the difference to $S = 5/2$ being induced by polarization on the bridging O atoms. From the XPS and XES data recorded for the valence region as well as from the computational results, we have determined the partial contributions of the constituents to the valence band. From the computational results on the electronic structure, the order of magnitude of the exchange coupling constants was determined.

Chapter 5

$LaNi_{5-X}Me_X$ (Me = Cu, Al) intermetallic compounds

Intermetallic compounds of owing the RM_5 general formula (Haucke compounds), where R is a rare–earth, yttrium or lanthanum and M is a transition metal, have attracted for the last twenty years the interest of the scientific community and industry due to their technological relevance as permanent magnets ($SmCo_5$) or as practicable hydrogen storage materials ($LaNi_5$). For compositions with lanthanum it was primarily the consequence of the extraordinary properties of $LaNi_5$ based alloys to adsorb and desorb under moderate conditions larger amounts of hydrogen per unit volume than liquid hydrogen [202, 203]. $LaNi_5$–type alloys are nowadays technologically and commercially very important for a wide range of applications including negative–electrode materials for widespread rechargeable Ni–metal hydride (Ni–MH) batteries, hydrogen source for fuel cells and energy–conversion or storage systems [204–206]. More than a billion RM_5–based batteries are produced and sold per year.

Various specific properties are of interest when talking about metal hydrides: storage capacity, velocity and reversibility of hydrogen sorption, plateau pressure and temperature, cycling life and, nevertheless, implementing, environmental and economical costs. Nowadays several systems are widely used. Alloys deriving from $LaNi_5$ were found to be very attractive due to their fast and reversible sorption properties, plateau pressure of a few bars at room temperature, respectable long cycling–life as well as their environmentally safe character. La or Ni are, in contrast to Cd, no hazardous constituents. Their disadvantage is connected to the storage capacity which remains below 2 mass% (see Reference [202]).

Substantial changes in properties of hydrogen host materials can be induced by alloying: hydrogen storage properties and/or crystal structure are strongly modified when nickel is partially substituted by aluminium or cooper. For example $LaNi_5$ hydrogenates up to $LaNi_5H_{6.7}$ at a vapor pressure of about 4 atm (42 °C) whereas for $LaNi_3Cu_2$ the storage capacity is reduced to 4 H atoms per formula unit and an equilibrium pressure of about 1.5 atm. Various effects can be also induced by substituting with other metals. Several La substitutions were also accounted for strong changes of the alloy properties.

There is a considerable interest in the electronic structure and magnetic properties of $RNi_{5-x}Me_x$ compounds. In spite of huge experimental effort concentrated on this

class of materials, most of the studies dealt with technological issues like improvement of cycle life, deterioration mechanism, optimal casting conditions and so forth. Only a few studies were dedicated to the electronic structure or magnetic properties. This may be the reason why some of the aspects are still controversial and the work is far to be complete.

Let us take $LaNi_5$ as an example: first–principles augmented plane wave (APW) calculations of $LaNi_5$ electronic structure were first reported by *Malik et al.* [207]. A charge transfer of 1.5 electrons from La to Ni atoms was calculated. Later theoretical studies performed by *Gupta* found no explanation for such a large charge transfer and suggested a bonding arising from hybridization rather than electron transfer [208, 209]. The results based on a semi–empirical tight–binding method shown a qualitative describing of the electronic structure. Nowadays it is well accepted that no charge transfer takes place in $LaNi_5$ but some of the results are still contradictory. For example: *Nakamura et al* [210] seem to reach right conclusions but their results on the electronic structure were reported to be "similar" to those reported both in [207] and [208, 209]. This is of course inconsistent.

Concerning the magnetic properties, $LaNi_5$ is considered to be at 4.2 K a classical Pauli–type–paramagnet. The estimated exchange-enhancement factor ($s = 5 - 6$) is lower than that reported for Laves–phase compounds. In case of RCo_2 paramagnets (R = Y, Lu, Sc, Hf), which exhibit strong exchange-enhancement factors ($s = 9 - 10$), it was evidenced that their magnetic behavior is more complicated than the Pauli–type paramagnetism [211–213]. Could it be also the case for $LaNi_5$? Or the accepted opinion regarding the Pauli–type paramagnetism of $LaNi_5$ is right due to the lower exchange–enhancement factor? To these questions as well as to others not listed at this point, it will be given a detailed answer in this work.

The aim of this study is to clarify the magnetic behavior of $LaNi_5$ and of selected substituted $LaNi_{5-x}Me_x$ systems by means of experimental and theoretical investigations of the electronic structure and of magnetic measurements. Some important aspects will be given a special attention. The magnetic data are now corrected for the presence of magnetic impurities. The presented analysis makes use of the deep correlation between the electronic structure and the magnetic properties and gets on this way a solid basis. From this point of view, the joint approach is a consistent way to reach undoubted conclusions.

5.1 State of the art

$LaNi_5$ was reported to be at 4.2 K an exchange–enhanced Pauli–type paramagnet having a magnetic susceptibility $\chi = 2.5 \times 10^{-3}$ emu/f.u. [214], 2.27×10^{-3} emu/f.u. [215] or 1.98×10^{-3} emu/mol [216]. An exchange–enhancement factor of about 5–6 was reported. These data must be reconsidered nowadays for at least two reasons. First, no corrections for the presence of magnetic impurities were performed and thus the accuracy of the above numerical data is questionable. They can only be regarded as upper limits. Secondly, recent developments in the understanding of 3d metallic paramagnetism revealed that at low temperatures the magnetic behavior of strong exchange-enhanced paramagnetic materials (s = 9–10) is more complicated than a simple Pauli–type paramagnetism [211–213].

Despite of the huge number of papers published on hydrides, only a few dealt with the electronic structure and magnetic properties of $LaNi_5$. The first spin–polarized self–consistent APW calculations by Malik *et al.* predicted a large charge transfer of 1.5 electrons from La to Ni atoms and a weak ferromagnetism with 0.69 μ_B magnetic moment per formula unit almost entirely due to Ni (the Ni minority spin band should be almost filled) [207]. Other calculations as well as experimental results conflict with these statements. *Gupta* used a tight–binding recursing formalism [208, 209] to qualitatively describe the electronic structure. No explanation for such a charge–transfer was found: the bounding in $LaNi_5$ arises from hybridization rather than from charge transfer, as previously proposed [217]. Recently first–principles TB–LMTO–ASA calculations were reported [218–223]. $LaNi_5$ was shown to be non–magnetic and with a valence band mainly derived from the Ni 3d states. The La 4f states are unoccupied and give rise to a sharp peak in the DOS about 3 eV above the Fermi level. The calculations pointed out a large value for the density of states at the Fermi level, in agreement with the experimental results. Nakamura *et al.* employed a TB–LMTO–ASA formalism and reported a 0.602 μ_B/f.u. magnetic moment [210]. No statement on the magnetic behavior was made. Very recently first–principles calculations were performed within the GGA approximations for $LaNi_5$–H hydrides [224]. Unfortunately they leaved out the parent compound.

Photoemission investigations were also reported for this compound. XPS measurements revealed that no charge–transfer should be expected between La and Ni since no chemical shifts were detected for Ni 2p and La 3d line compared to pure La and Ni [217, 225–227]. It is a clear experimental indication that no charge transfer takes place upon formation of the alloy. XPS/UPS valence band studies on $LaNi_5$ [221, 225, 228, 229] show that the density of occupied states is dominated by the Ni 3d states.

With one exception, all the reported band structure calculations were not directly compared with photoemission data. Thus they give a rather good view on the electronic structure of $LaNi_5$ but cannot rule out controversial results like in Reference [210]. In Reference [221] the theoretical results for compositions with x = 1 were compared with recorded UPS valence band but the authors calibrated the binding energy by assuming no chemical shifts of the Ni lines, which is inconsistent. Practically there are no other joint studies of the electronic and magnetic properties for this class of materials.

The partial substitution of Ni in $LaNi_5$ was accounted for strong effects on the heat of hydride formation (compound stability) and hydrogen adsorption/desorption properties. Such variations may be caused by differences in the electronic structure of the host intermetallic compound, particulary band filling effects. It has been found that substitutions by Cu or Al decreased the equilibrium pressure of the $LaNi_{5-x}(Cu,Al)_x$ electrodes [230–233].

5.2 Samples details

The samples were prepared by induction furnace of pure components (La 99.9%; Ni, Cu, Al 99.99%) in purified argon atmosphere and remelted several times in order to ensure a good homogeneity. A small excess of La ($\leq 1\%$) was added to compensate for

the weight loss during melting. The samples were annealed under vacuum at 1000 °C for one week. The samples were kindly made available to us by Prof. Dr. Emil Burzo[1].

The $LaNi_5$ intermetallic compound crystallizes within a hexagonal structure of $CaCu_5$ type (space group $P6/mmm$; Pearson symbol $hP6$) in which La atoms occupy the $1a$ sites. In this system nickel atoms are distributed over the $2c$ sites in the basal La planes ($z = 0$) and $3g$ type sites in the middle plain of the hexagonal structure ($z = 1/2$) (see Figure 5.1) [234].

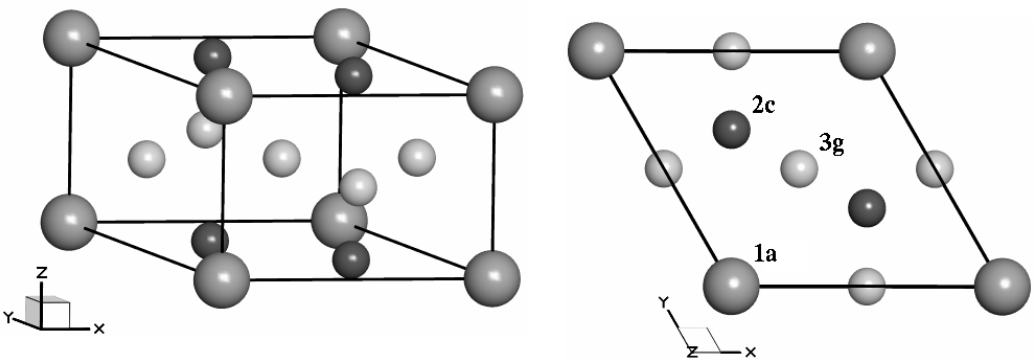

Figure 5.1: $CaCu_5$–type structure of $LaNi_5$.

Different solid solutions for the $LaNi_{5-x}Cu_x$ system were reported, with a copper content ranging from x = 1.5 to x = 5 [234]. Copper was reported to substitute nickel at both $2c$ and $3g$ sites [234–237]. Nevertheless the preference for the occupancy of $2c$ sites by Cu is rather unexpected because in $LaNi_{5-x}M_x$ compounds M atoms larger than Ni (M=Mn, Fe, Al, Si) usually occupy the $3g$ positions since these allow larger Ni–M distances. The X–ray diffraction patterns of the investigated $LaNi_{5-x}Cu_x$ samples showed the presence of only one phase with a $CaCu_5$–type structure in the composition range $x \leq 1.5$. The composition dependence of the lattice parameters is presented in Figure 5.2 and their numerical values are listed in Table 5.1 together with some recent crystallographic data found in the literature. While the a parameter of the hexagonal is decreased at higher copper concentrations, the opposite variation of c results in an overall increase of the cell volume (see Table 5.1)

Compound	Structure type	Lattice parameters a (Å)	b (Å)	Cell volume V(Å^3)	c/a ratio	Reference
$LaNi_5$	$CaCu_5$	5.0110	3.911	85.05	0.780	this work
		5.0170	3.981	86.78	0.794	[221]
		5.0100	3.972	86.34	0.793	[222]
$LaNi_{4.5}Cu_{0.5}$	$CaCu_5$	5.0106	3.940	85.66	0.786	this work
$LaNi_4Cu$	$CaCu_5$	5.0100	3.980	86.51	0.794	this work
		5.0400	4.009	88.19	0.795	[221]
$LaNi_{3.5}Cu_{1.5}$	$CaCu_5$	5.0090	4.001	86.93	0.799	this work

Table 5.1: Crystallographic data for the $LaNi_{5-x}Cu_x$ system.

[1]Actual address: Babeş–Bolyai University, Faculty of Physics, RO-3400 Cluj–Napoca, Romania.

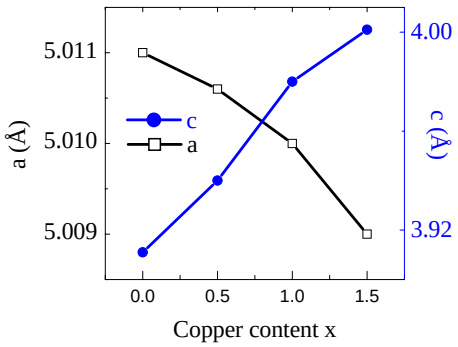

Figure 5.2: Dependence of the lattice parameters versus copper content for the $LaNi_{5-x}Cu_x$ system.

For the ternary $LaNi_{5-x}Al_x$ the crystallographic structure is marked by a change in the cell type. The X–ray diffraction patterns shown that for $x < 2$ the single substituted $LaNi_{5-x}Al_x$ system form solid solutions having hexagonal $CaCu_5$–type structure. For $2 < x \leq 3$ the structure changes to a $HoNi_{2.6}Ga_{2.4}$–type [238] analogous to other $RNi_{5-x}Al_x$ systems (R = Gd [239]; R = Dy [240]; R = Nd, Gd [241]. This structure is also hexagonal (space group $P6/mmm$; Pearson symbol $hP18$), having a larger unit cell than the $CaCu_5$ one. The unit cell parameters of the two types of structures are related by $a_{HoNi_{2.6}Ga_{2.4}} = \sqrt{3}a_{CaCu_5}$ and $c_{HoNi_{2.6}Ga_{2.4}} = c_{CaCu_5}$ [241] (see Figure 5.3).

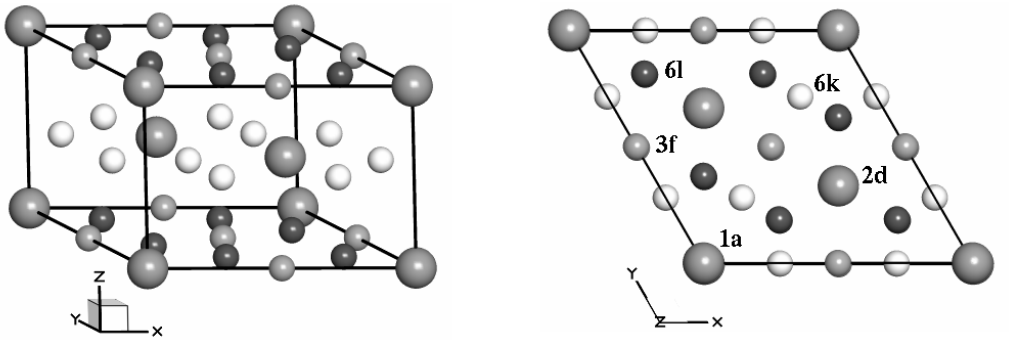

Figure 5.3: $HoNi_{2.6}Ga_{2.4}$–type hexagonal structure of $LaNi_{5-x}Al_x$ compounds when $2 < x \leq 3$.

In $CaCu_5$–type structure, the Al substitution takes place at the $3g$ sites situated in the $z = 1/2$ plane which does not contain La atoms since this site allows greater Ni–Al distances. The total filling of the $3g$ sites by Al is not possible since the distances between Ni and Al or Al–Al are smaller than the sum of metallic radii $r_{Ni}+r_{Al}$ or $r_{Al}+r_{Al}$ and thus a structure change appears. The occurrence of $HoNi_{2.6}Ga_{2.4}$ superstructure induces an increase of the distances between Al($3f$)–Ni($6k$) and Al($3f$)–Al($6k$), making the possibility to locate aluminium in the $3f$ and $6k$ sites. In this structure, Ni occupies completely $6l$ sites and Al $3f$ sites. The $6k$ sites are statistically occupied by

Ni and Al and the 2*d* sites are completely occupied by La. The composition dependence of the lattice parameters of $LaNi_{5-x}Al_x$ compounds is listed in Table 5.2 along with some recent crystallographic data found in the literature. For the composition range with $CaCu_5$–type structure the volume of the unit–cell increases more rapidly than for copper substitutions. Numerically for compositions with x = 1, the relative variation of the unit–cell volume with respect to $LaNi_5$ is $\Delta V/V = 1.71\%$ for $LaNi_4Cu$ and $\Delta V/V = 6.36\%$ for $LaNi_4Al$.

Compound	Structure type	Lattice parameters a (Å)	b (Å)	Reference
$LaNi_5$	$CaCu_5$	5.011	3.911	this work
$LaNi_4Al$	$CaCu_5$	5.071	4.062	this work
		5.063	4.063	[234]
		5.070	4.076	[221]
		5.058	4.008	[222]
$LaNi_3Al_2$	$CaCu_5$	5.145	4.122	this work
$LaNi_2Al_3$	$HoNi_{2.6}Ga_{2.4}$	9.180	4.050	this work

Table 5.2: Crystallographic data for the $LaNi_{5-x}Al_x$ system.

5.3 Experimental and computational details

The magnetic measurements presented in this study were performed in the temperature range 1.7–300 K and fields up to 8 T. For each temperature, the magnetic susceptibility has been determined from magnetization isotherms, according to the Honda–Arrott plot [242]:

$$\chi = \chi_p + \frac{cM_s}{H} \tag{5.1}$$

by extrapolation to $H^{-1} \rightarrow 0$. By c a presumed impurity content is denoted and M_s is their saturation magnetization. The aim of this procedure is to eliminate any possible alteration of the χ values as a result of the presence of small quantities of magnetic ordered impurities. It requires measurements at multiple fields values at the same temperature. The samples were generally shown to be free from magnetic impurities. A very small content of a magnetic ordered phase ($< 0.1\%$) was evidenced only at low temperatures. This can increase the magnetic susceptibilities by up to $15 - 20\%$, if corrections were not made.

For XPS studies all samples were prepared and investigated in the same manner in order to facilitate the comparison. They were fractured in preparation chamber in vacuum below 5×10^{-8} mbar and then immediately moved into the main chamber. The XPS spectra were recorded in a vacuum below 5×10^{-9} mbar. Binding energies are given with reference to the Fermi level. The calibration of the XPS spectra was performed according to the $4f_{7/2}$ core level of gold which was found at 84.0 eV. This is based on the metallic character of the samples i.e. good electrical conductivity. The amount of oxygen on the fresh cleaved surfaces was checked by survey spectra and monitored through the measurements. The samples presented tiny amounts of oxygen

and tiny amounts of carbon. The presence of this small oxygen contamination can be explained by adsorption at the surface after cleaving the samples in the preparation chamber. Its presence due to fracturing along oxygen–rich grain boundaries, where oxygen had naturally segregated, is excluded.

The presented band–structure calculations were carried out in frame of the ab–initio tight–binding linear muffin–tin orbitals formalism in the atomic sphere approximation (TB–LMTO–ASA) [243–245] and employing The Stuttgart Tight–Binding LMTO Program, version 4.8. The choice of this type of calculations is motivated by the relatively large number of atoms in the super–cell. Additionally the investigated structures are closed packed crystalline configurations. Relativistic corrections were included with spin–orbit coupling. The Perdew–Wang non–local exchange correlation potential was used. The structures were considered to be ordered i.e. a possible clustering of the substituting atoms was avoided. The convergence criteria was set to 0.01 mRy between the energy of two consecutive iteration steps.

5.4 Experimental results

5.4.1 Magnetic data

The magnetic data presented in this section were kindly provided to us by Prof. Dr. Emil Burzo.

The temperature dependence of the magnetic susceptibilities χ for $LaNi_{5-x}Cu_x$ are plotted in Figures 5.4 and 5.5. The low temperature susceptibility values χ for $LaNi_5$ are shown in the inset of Figure 5.4 as a function of T^2. As evidenced at $T < 10$ K, the susceptibility of $LaNi_5$ follows a relation of the form:

$$\chi_p = \chi_0(1 + aT^2) \tag{5.2}$$

with $a = 1.3 \times 10^{-3}$ K^{-2}.

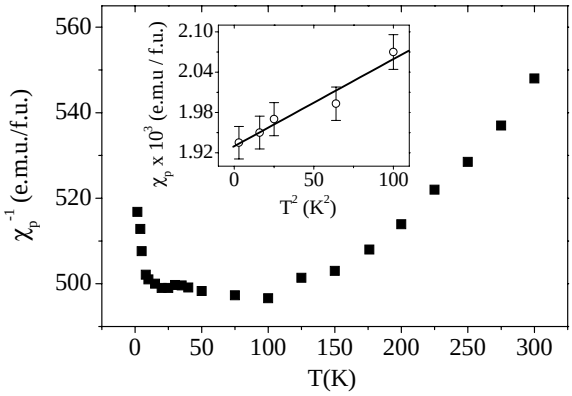

Figure 5.4: Temperature dependence of the magnetic susceptibilities for $LaNi_5$ ($\chi_p \pm 1\%$). In inset the low temperatures behavior is plotted.

The same thermal dependence pattern is visible for all the samples in this system: the magnetic susceptibilities increase up to a temperature T_{max} and then decrease.

Above a characteristic temperature T^* a Curie–Weiss type behavior is observed. The T_{max} and T^* are shifted to lower temperatures when increasing the copper content. For x = 0, $T_{max} \simeq 90$ K and $T^* \simeq 150$ K. Due to this shift, the region where the T^2 dependence can be observed is diminished, and thus no reliable data on the T^2 dependence can be obtained for compounds with x $\geq$ 0.5. These magnetic data show a transition from a Pauli–type paramagnetism to a Curie–Weiss behavior as the temperature increases, similar as found in cobalt based compounds [211–213]. In the high temperature magnetic susceptibilities can be described by the Curie–Weiss law: $\chi = C(T-\theta)^{-1}$. We denoted by C the Curie constant and θ is the paramagnetic Curie temperature.

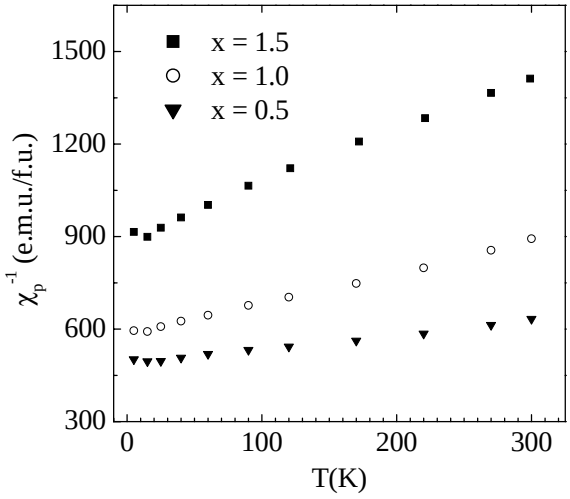

Figure 5.5: Temperature dependencies of the magnetic susceptibilities for $LaNi_{5-x}Cu_x$ with x = 0.5, 1.0 and 1.5 ($\chi_p \pm 1\%$).

Sample	$-\theta$ (K)	$M_{eff}(Ni)$ (μ_B/atom)	C (emu·K/fu)	$\chi_p \times 10^3$ (emu/fu)
$LaNi_5$	1104	2.15	2.850	1.93 (1.7 K)
$LaNi_{4.5}Cu_{0.5}$	978	1.96	2.163	1.90 (4.2 K)
$LaNi_4Cu$	577	1.41	0.990	1.60 (4.2 K)
$LaNi_{3.5}Cu_{1.5}$	526	1.15	0.581	1.15 (4.2 K)

Table 5.3: Magnetic data obtained on the $LaNi_{5-x}Cu_x$ system, including the low temperature paramagnetic susceptibilities.

From the linear region of χ^{-1} versus T, the effective nickel moments $M_{eff}(Ni)$ as well as the paramagnetic Curie temperature θ, were determined (see Table 5.3). The $M_{eff}(Ni)$ and θ values were obtained directly from experimental data with or without considering the diamagnetic and paramagnetic contributions of the constituents ions. The differences between $M_{eff}(Ni)$ and θ values obtained in both of these cases are not significant. The effective nickel moments and the absolute value of the paramagnetic Curie temperatures decrease in a similar way with increasing Cu content. The θ values are negative for all the studied compounds.

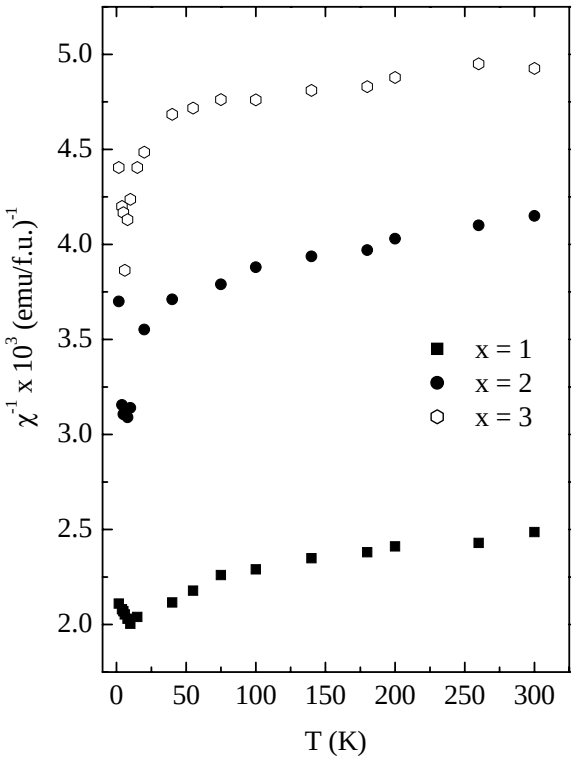

Figure 5.6: Thermal variations for the reciprocal magnetic susceptibilities measured for $LaNi_{5-x}Al_x$ ($\chi_p \pm 1\%$).

For the $LaNi_{5-x}Al_x$ system the temperature dependence of the magnetic susceptibilities follows a similar pattern – Figure 5.6. The T_{max} values which mark the maximum value of magnetic susceptibility are shifted to lower temperatures and are situated at about 12 K (x = 1), 8 K (x = 2) and 6 K (x = 3). For aluminium doped samples, above a characteristic temperatures T^*, which decrease from $T^* = 20$ K (x = 1) to 10 K (x = 3), the magnetic susceptibilities can be described as a superposition of a Pauli paramagnetic term, χ_{Pauli}, on a Curie–Weiss type contribution:

$$\chi = \chi_{Pauli} + C(T - \theta)^{-1} \tag{5.3}$$

Sample	$-\theta$ (K)	$M_{eff}(Ni)$ (μ_B/atom)	C (emu·K/fu)	$\chi_p \times 10^3$ at 1.7 K (emu/fu)	$\chi_{Pauli} \times 10^4$ (emu/fu)
$LaNi_5$	1104	2.15	2.850	1.93	–
$LaNi_4Al$	650	0.72	0.260	0.47	1.00
$LaNi_3Al_2$	240	0.27	0.028	0.27	1.80
$LaNi_2Al_3$	220	0.18	0.008	0.23	1.85

Table 5.4: Magnetic data obtained on the $LaNi_{5-x}Al_x$ system, including the low temperature paramagnetic susceptibilities.

Similar to the $LaNi_5$ compound, for the ternary system with aluminum $LaNi_4Al$

in the low temperature range ($T \leq 10$ K) the magnetic susceptibilities follow a T^2 dependence by Equation 5.2 with $a = 0.23 \times 10^{-3}$ K^{-2} – Figure 5.7.

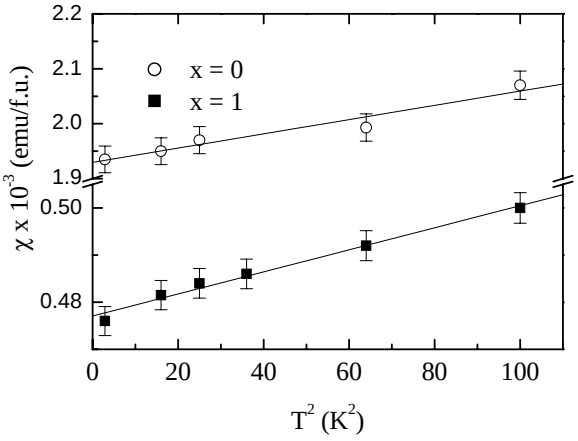

Figure 5.7: Magnetic susceptibility versus T^2 in the low temperature region for $LaNi_5$ and $LaNi_4Al$

Since the temperatures T_{max} are very low for compounds with higher aluminium content than $x \geq 2$, it was not possible o analyze the temperature dependence of their magnetic susceptibilities in low temperature region. A stronger dependence of the Curie constants on the aluminium content can be noticed than in case of copper substitutions. The numerical data extracted from magnetic measurements on $LaNi_{5-x}Al_x$ are presented in Table 5.4.

5.4.2 XPS results

The XPS measurements were aimed at two main issues. First the absolute binding energy and the Ni 6 eV satellite are excellent indicators of the nickel electronic structure and correlations effects. Second, valence band spectra are expected to reflect the changes induced by substitutions in the DOS distribution of the parent compound $LaNi_5$.

$LaNi_{5-x}Cu_x$

The Ni 2p and La 3d core level lines of $LaNi_{5-x}Cu_x$ are presented in Figure 5.8. The La $3d_{3/2}$ line overlaps with the Ni $2p_{3/2}$ line. The 2p lines of a pure Ni sample fractured in UHV were measured under the same conditions as the $LaNi_{5-x}Cu_x$ system. Each of the Ni 2p lines at about 852.7 and 869.8 eV are accompanied by one satellite positioned at about 6 eV higher binding energies. The satellite intensity is lower as compared to that of pure Ni. Since of the overlap between La $3d_{3/2}$ and Ni $2p_{3/2}$ signals, no accurate determination of the Ni $2p_{3/2}$ binding energy can be performed. Still taking into account the sharpness of Ni $2p_{3/2}$ as compared to the relatively low intensity of La signal around 850 eV, the binding energy of Ni $2p_{3/2}$ peak is determined to be 852.7 ± 0.05 eV in all the indicated spectra. This means

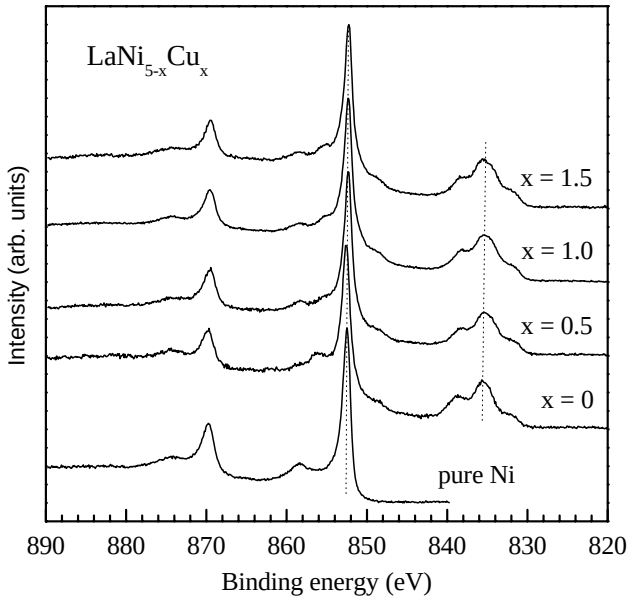

Figure 5.8: The Ni $2p_{3/2}$, $2p_{1/2}$ and La $3d_{3/2}$ core lines for $LaNi_{5-x}Cu_x$.

that no detectable charge transfer to/from the Ni atoms occurs when alloying with La and Cu. The shape of La 3d line is practically identical with the XPS results previously reported for $LaNi_5$ [225, 227]. In Reference [227] a single crystal sample was investigated. The multi–peak structure between 830 and 840 eV may be explained by accounting for interplay of multiplet effects as calculated for La $3d_{5/2}$ line in other lanthanum compounds [246]. Since the La $3d_{3/2}$ is expected to have a similar form, this accounts for the low–intensity peaks at 848.5 and 855.5 eV near the Ni $2p_{3/2}$ peak. Additionally, the position of the structures can be considered as unchanged in the series. An accurate determination of the La $3d_{5/2}$ binding energy is affected by the shape of the line.

In Figure 5.9 are plotted the Cu 2p core lines recorded for this system. No satellite structures are present below the two Cu lines corresponding to the spin–orbit splitting. Their binding energies was determined as being constant and about 932.3 eV. For pure Cu the binding energy of the Cu $2p_{3/2}$ line is 932.7 eV [147]. This difference will be discussed later. From the features of the Cu 2p lines (no satellite structures and low width) a possible d^{10} electronic configuration of the Cu d band is indicated.

The XPS valence bands recorded for the $LaNi_{5-x}Cu_x$ samples and for pure Ni are presented in Figure 5.10. There is a similarity of the Ni 3d bands in pure Ni with those in $LaNi_5$. This fact evidences that the valence band of $LaNi_5$ is mainly derived from Ni d states. The structure at about 6 eV binding energy is the well–known Ni satellite. The contribution of La states to the valence band of $LaNi_5$ is not visible in the spectra because of the low cross-sections of La. Alloying with Cu does not induce visible changes in the Ni d band. A slight shift to higher binding energies of the Ni 3d states occurs with increasing Cu concentration but the changes can be regarded as being minimal. A rather independent Cu d band is formed around

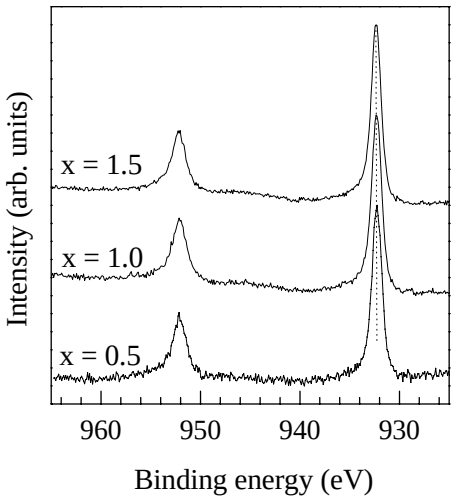

Figure 5.9: The Cu 2p core lines recorded for the $LaNi_{5-x}Cu_x$ system

3.3 eV binding energy. By increasing the Cu content, the relative intensity of the Cu d band is increased. These Cu states are probably completely filled with electrons (d^{10} electronic configuration) since they are situated deep enough below the Fermi level. This affirmation is also supported by the features of Cu 2p core–level lines as mentioned before. The width of the Cu specific line is not changed by increasing the Cu content.

$\mathbf{LaNi_{5-x}Al_x}$

The Ni 2p and La 3d core–level lines are plotted in Figure 5.11 for the $LaNi_{5-x}Al_x$ samples. Analogous to the previous system due to the overlapping of the Ni $2p_{3/2}$ line with the La $3d_{3/2}$ one, no accurate determination of the Ni 2p positions can be made. A fit was performed by taking into account that the sharp peak corresponds to the Ni $2p_{3/2}$ line. The determined binding energies, in the limit of experimental errors, seem to be not dependent on aluminium content and to correspond although a hardly detectable shift to higher binding energies might be accounted at the limit of experimental resolution. This feature indicates that the alloying with aluminium does not induce measurable charge transfers to/from nickel positions, although the trend exists. A specific feature of the presented spectra is the gradual vanishing of the Ni 6 eV satellite when alloying with Al; for samples with $x > 1$ it cannot be observed. The small peak at about 855 eV can attributed to the presence of a small quantity of some lanthanum in other configuration or to some changes in the shape of La 3d line as visible for the 3d $_{3/2}$ component. To be noticed that lanthanum exhibits an anomalous chemical shift, the La 3d $_{3/2}$ line in La_2O_3 being positioned at 834–835 eV i.e. above the value specific for the pure metal [147]. Moreover since of the complicated shape of the La 3d lines it is difficult to evaluate possible shifts of the lanthanum specific lines.

Several factors are responsible for the difficulties related to the determination of Al 2p binding energy. Among them: the low photoionization cross–section ($0.72 \times$

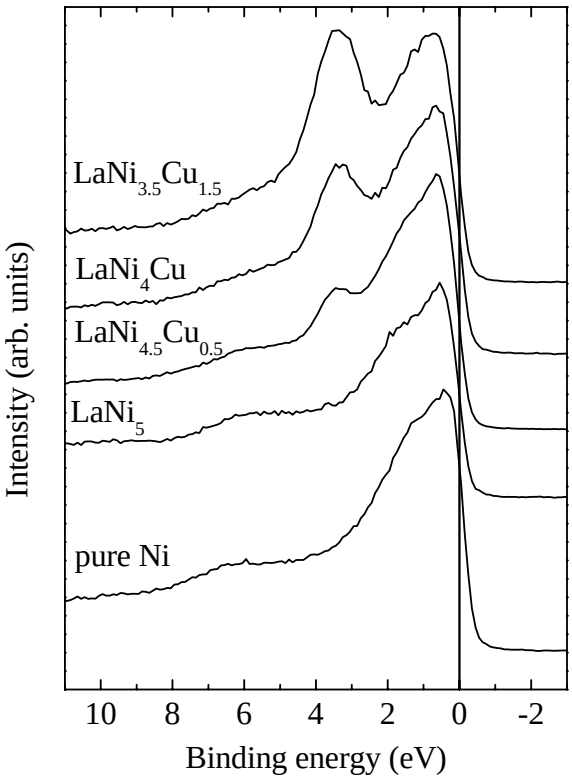

Figure 5.10: Valence band spectra recorded for the $LaNi_{5-x}Cu_x$ system.

10^{-2} Mb compared with 0.2998 Mb for Ni 2p [38], some amount of oxidized Al and background disturbance due to the Ni 3p, the low atomic concentration as well as the low spin–orbit splitting (about 0.4 eV [247]). An higher acquisition time was set up for the sample with the highest aluminum concentration and the recorded spectrum is shown in Figure 5.12. The spin–orbit coupling of the Al 2p lines is visible around 72.3 eV. The two peaks at about 66.8 and 68.2 eV are the two spin–orbit components of the Ni 3p line. The structure at about 74.8 eV probably corresponds to oxidized Al. To be noticed that even pure Al samples investigated after a long–time Ar sputter usually present some traces of oxidized materials [247]. Without taking into account the asymmetry of Al peaks, the binding energy of Al $2p_{3/2}$ can be evaluated at $72.0 - 72.2$ eV. The reported values for pure Al are 72.9 eV [147], 72.7 eV [247] or even 72.5 eV [248] in an older measurement.

The XPS valence bands recorded for the $LaNi_{5-x}Al_x$ system and pure Ni are shown in Figure 5.13. The contribution of La states to the valence band is not visible in the spectra. Alloying with Al induces visible changes in the $LaNi_5$ valence band, the most visible being the shift of maximum of the valence bands to higher binding energies. The maximum is placed at 0.59 eV in pure Ni, $\simeq 0.67$ eV in $LaNi_5$, 0.80 eV in $LaNi_4Al$, 1.60 eV in $LaNi_3Al_2$ and 1.74 eV for $LaNi_2Al_3$. Assuming a constant experimental resolution, the density of states at the Fermi level decreases for all the ternary compositions when compared to $LaNi_5$. Since the Ni 3d states are expected to be dominant in the valence band region the shift of the maxima is associated to

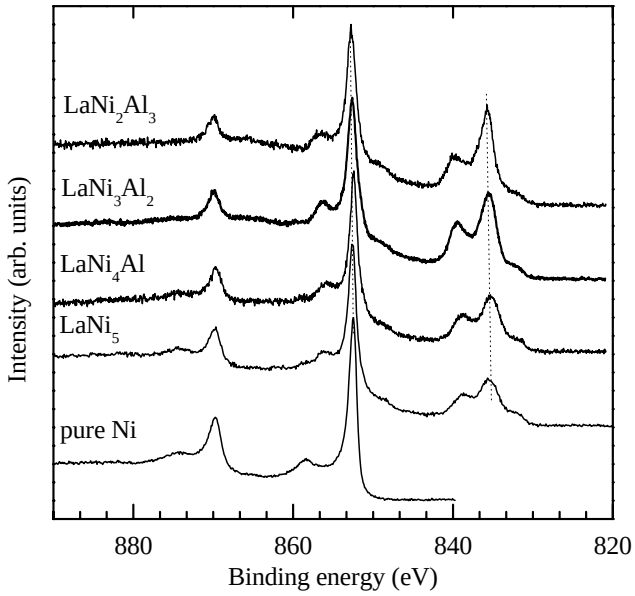

Figure 5.11: The Ni 2p and La 3d XPS core–level lines recorded for the $LaNi_{5-x}Al_x$ system.

strong changes in the Ni d band with alloying.

The XPS experimental findings for the $LaNi_{5-x}Al_x$ system are interesting since it would be reasonable to expect a gradual filling of the Ni bands as the corresponding maximum is shifted to lower binding energies. This is however not reflected by the core–level measurements of the Ni 2p line, at least not above the experimental resolution.

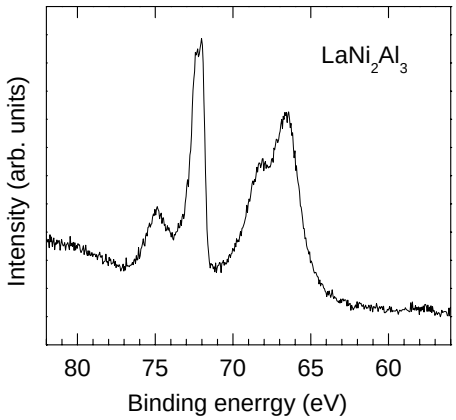

Figure 5.12: Al 2p and Ni 3p recorded for the $LaNi_2Al_3$ sample

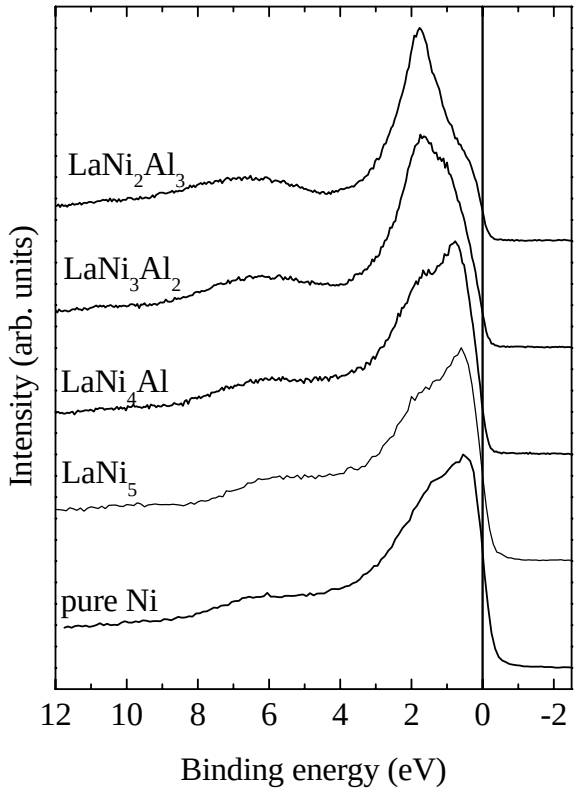

Figure 5.13: XPS valence band spectra recorded for the $LaNi_{5-x}Al_x$.system.

5.5 Computational results

As previously mentioned, computational results are available in the literature for the parent compound and some single substituted compositions $LaNi_4Me$. In order to achieve a solid basis for the current study, band structure calculations were performed in the same terms for all compositions.

$LaNi_5$

The density of states (DOS) and the local contributions from each atom site are presented in Figure 5.14 for $LaNi_5$. As previously reported, spin–polarized calculations converged well to a self–consistent non–magnetic solution. $LaNi_5$ is certainly non–magnetic, as indicated by magnetic measurements. Analogous to the results obtained with XPS in the valence band region, the valence states of $LaNi_5$ are dominated by the Ni 3d band, which is not completely filled with electrons. The contribution of Ni 4s states is negligible. La states (mostly 5d) hybridize with Ni 3d bands but their contribution to the density of states at the Fermi level is very low (below 3.5%). The La 4f states are practically unoccupied and give rise to a sharp DOS peak located at about 4.8 eV above the Fermi level. The Ni 3d–La 5d hybridization is a key factor of the electronic structure: its role is evident when arguing on the character of the compounds which is evidently of non charge–transfer type. The DOS at the Fermi

edge was calculated at 8.65 states/eV·f.u. which is in very good agreement with the previously reported values [221, 249]. The accuracy of this value is granted by the dense mash considered in the sampling of Brillouine region (1200 k points).

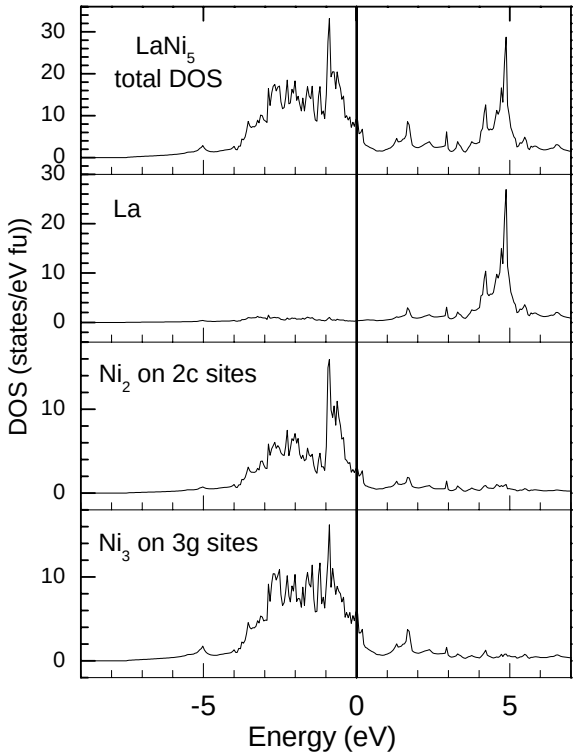

Figure 5.14: Calculated total and partial densities of states for $LaNi_5$.

At this point it is useful to mention that the output concerning the static charge distribution is not relevant, as considered sometimes in the literature. This consideration is not only a feature of the employed computational method but a quite general issue. The reason is simple: although the choice of the radii around each nucleus, where the charge is considered to belong a certain atomic species, is not arbitrary, its value has no precise relevance for the charge assigned to each crystallographic position. Therefore no charges assigned to each atomic position will be mentioned in this work.

$\mathbf{LaNi_{5-x}Cu_x}$

For $LaNi_{5-x}Cu_x$ both $2c$ and $3g$ occupancies for the Cu atoms should be taken into account as suggested by experimental studies [234–237]. In this work various configurations for the construction of the super–cell were tried out in order to simulate combined occupancy schemes. While the general density of states distribution seems to be roughly unaffected by the choice of substitution on $2c$ or $3g$ sites, this issue should be still given a reasonable answer. It should be mentioned that from this point of view, the argument of the minimum total energy (used in [222]) is not reliable enough to choose in favour at a certain configuration because the accuracy of the

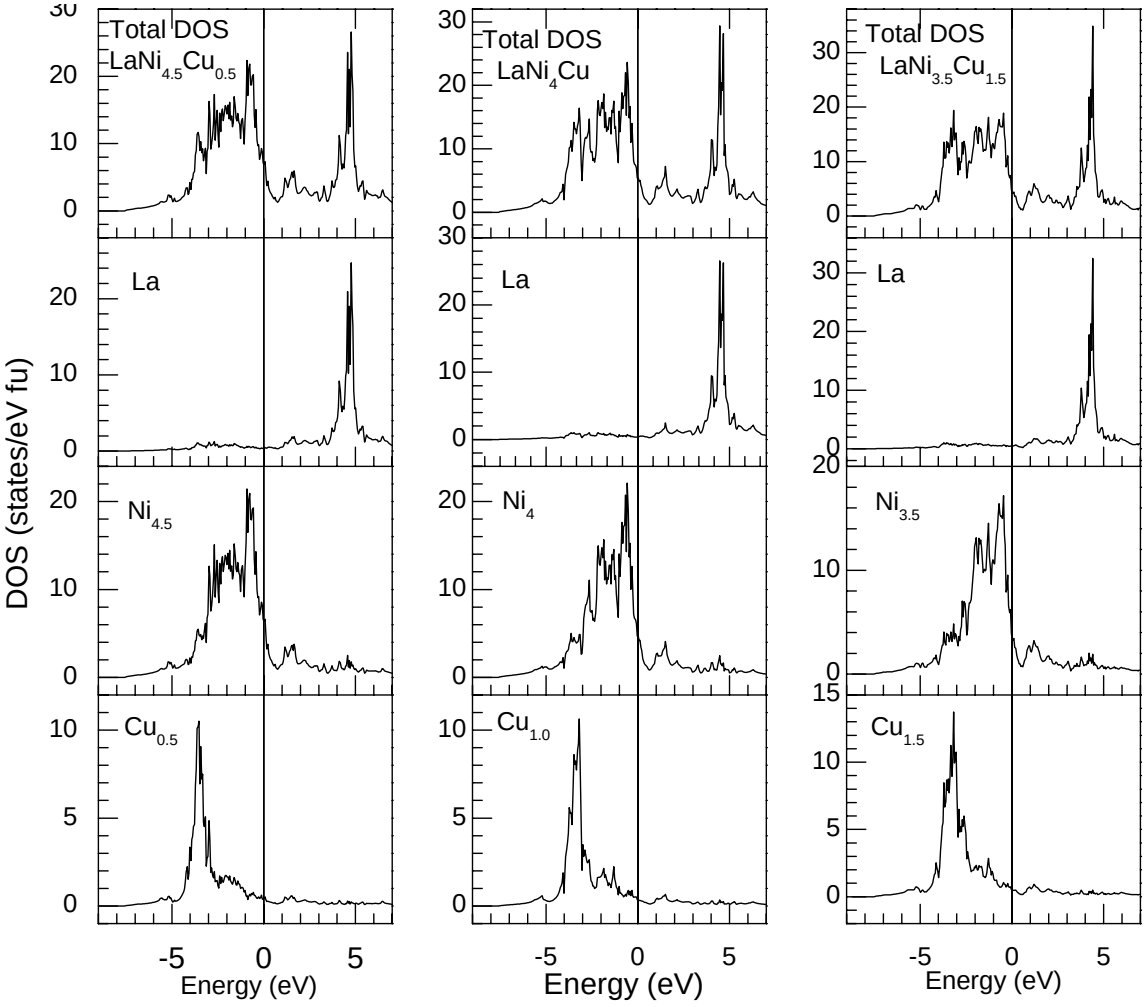

Figure 5.15: Calculated total and partial densities of states for the $LaNi_{5-x}Cu_x$ system.

TB–LMTO–ASA method with spherically symmetric potential in the atomic spheres does not warrant sufficient accuracy. The convergence to a non–magnetic solution was chosen as 'minimum criteria'. It was possible to show that only the substitutions on solely $3g$ sites lead to non–magnetic solutions as indicated by the magnetic measurements. Consequently, the substitutions on the Ni $2c$ sites were neglected in this work.

The total and partial DOS calculated for $LaNi_{5-x}Cu_x$ samples are plotted in Figure 5.15. The most important finding is visible in the lower panels. In agreement to the results evidenced in the XPS valence band study, a Cu band located at about 3–4 eV below the Fermi level is present. This corresponds to the Cu structure evidenced at 3.3 eV binding energy in the XPS spectra. The copper contribution at the Fermi level is very low and mostly of 4s character. The total DOS at the Fermi level has a descending trend: 6.01 states/eV·f.u. for x = 0.5, 5.46 states/eV·f.u. for x = 1.0 and 4.77 states/eV·f.u. for x = 1.5. The accuracy of these values was granted by a dense mesh employed in the sampling of the k–space (at least about 600 k points in

the irreducible wedge of the first Brillouin zone). The decrease of DOS at E_F is due to the narrowing of Ni 3d band as the Cu content is increased. The gravity center of Ni 3d states is slightly shifter to lower energies but cannot account for the mentioned dependence. In contrast to the results reported in Reference [221], for x = 1.0 the Fermi level is not located in a local minimum region of the DOS.

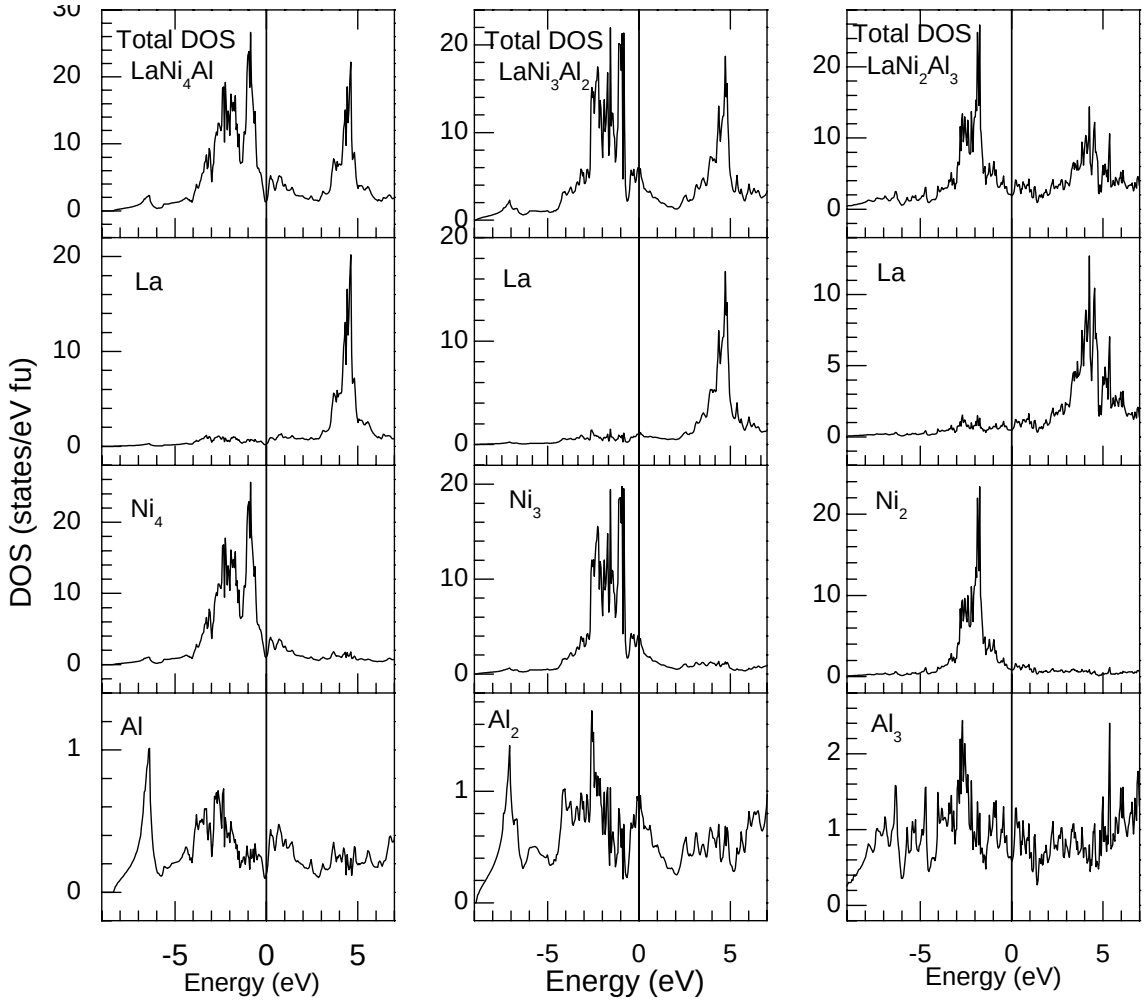

Figure 5.16: Calculated total and partial densities of states for the $LaNi_{5-x}Al_x$ system.

$\mathbf{LaNi_{5-x}Al_x}$

For compositions with aluminum (see the results listed in Figure 5.16) the changes of the Ni 3d band are obvious as visible in the XPS VB spectra. The Al substitution was considered to take place solely on $3g$ sites in agreement to the previous works [221, 222, 250]. All the calculations for the $LaNi_{5-x}Al_x$ system converged self–consistent to non–magnetic solutions. The Al contribution to the DOS shape is significant only at about -7 eV on the energy scale. Similar to the previous system, the La states are important only above the Fermi level where the 4f states are present in DOS. The

region of interest located just below the Fermi level is almost entirely due ti Ni d states. However the DOS at E_F has a complicated dependence with respect to the composition. For x = 1.0 the Fermi level is positioned in a local minimum region of the DOS distribution, as presented in [221, 222]. The calculated DOS at Fermi level was 1.42 states/eV·f.u. for x = 1 in agreement with the previous results. This decrease of about 85% with respect to the parent compound is considerably higher than for the compositions with copper where the percentage decrease was only about 10% for x = 1. This underlines the strong effects upon alloying with aluminum. For higher Al concentrations there is no trend the variation of absolute DOS at E_F. The calculated densities of states are: 5.90 states/eV·f.u. for x = 2 and 1.90 states/eV·f.u. for x = 3. These values resemble a more complicated situation and can be associated to the strong narrowing of the Ni d band.

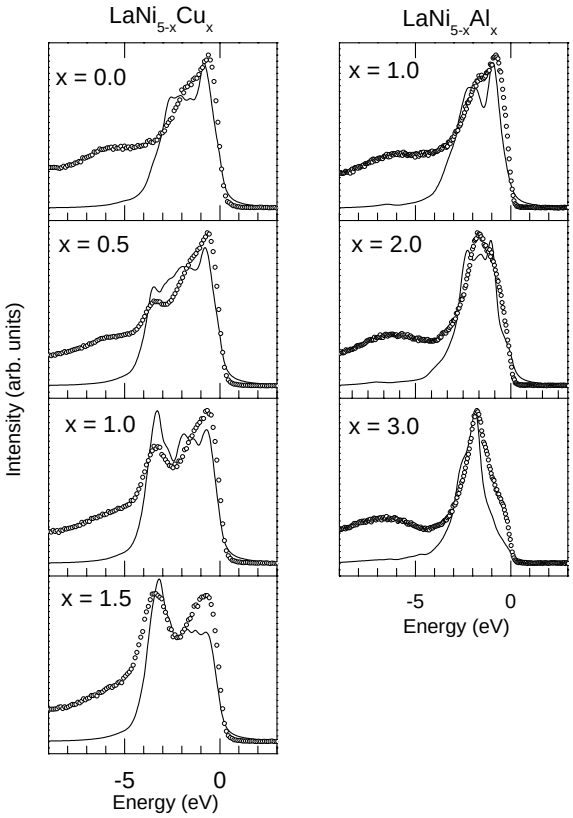

Figure 5.17: Comparison of the measured XPS valence bands (points), and the convoluted DOS (by Lorentzians of half–width 0.4 eV and taking into account proper cross–sections for partial bands with different l–symmetry; solid line) for the $LaNi_{5-x}Cu_x$ and $LaNi_{5-x}Al_x$ systems.

The theoretical results can be compared with the measured XPS valence bands. The orbital projected partial densities of states were multiplied with the proper cross-sections for 1486.6 eV incident radiation (Ni 3d: 0.52×10^{-2} Mb, Ni 4s: 0.83×10^{-3} Mb, La 5d: 0.76×10^{-3} Mb, La 6s: 0.29×10^{-3} Mb, Cu 3d: 0.12×10^{-1} Mb, Cu 4s: 0.27×10^{-3} Mb Al 3p: 0.59×10^{-4} Mb from [38]) and their sum was then convoluted

by Lorentzians of half–width 0.4 eV. The computed densities of states describe rather well the general features of experimental spectra. Important are from this point of view the good agreement between the maxima in the XPS VB spectra and the maxima in the simulated curves. The visible differences can be attributed mainly to the facts that band structures were calculated at 0 K and those obtained by XPS were recorded at room temperature. Also the inelastic scattering background present in XPS spectra was not subtracted.

5.6 Discussions

Before turning to the analysis of the presented results, let us briefly review the the aspects involved in the state of the art understanding of metallic magnetism. One of the first attempts to understand itinerant magnetism was due to Pauli [251]: the electrons in a non–interacting system (free–electron gas) can be fully described by two relevant quantum numbers: spin and electron momentum k. The magnetic susceptibility of the free–electron gas is given by:

$$\chi_{Pauli} = 2\mu_B^2 n(\varepsilon_F) \tag{5.4}$$

and depends alone on the density of states at the Fermi energy $n(\varepsilon_F)$. Later Stoner succeed to formulate the famous mean–field model for the magnetic behavior of itinerant electrons by replacing the free–electrons energy levels with the electronic band structure of the solid [252]. The susceptibility of the itinerant gas of electrons is given by:

$$\chi_{Slater} = \frac{2\mu_B^2 n(\varepsilon_F)}{1 - In(\varepsilon_F)} = \frac{\chi_{Pauli}}{1 - In(\varepsilon_F)} = s\chi_{Pauli} \tag{5.5}$$

where I is called 'Stoner exchange factor' and represents the exchange energy between un and down spins (Couloumb repulsion). The above formula gives a quantity equal to the Pauli susceptibility multiplied by a 'Stoner exchange–enhancement factor' s. Even the Stoner model gives a rather good description of the ground state properties, its finite temperature description completely fails. Moreover due to its band character this model can not account for the existence of local magnetic moments in metals. Van Vleck was the first to reveal the importance of electron correlations in a possible justification of a local picture [253]. The effects of electron correlations became a way to reconciliate the mutually opposite pictures of band theories and localized models. Systems where electrons never localize may be regarded as systems with weak electron correlations; on the other hand strong electron correlations induce the localization of the magnetic moments on certain crystallographic sites. Among the most successful models of local magnetic moments in metals should be mentioned the Anderson model in dilute alloys [254] and the Friedel model [255].

The magnetic behavior of some transition metal alloys shown that the study of electron correlations must be analyzed from a more general point of view. $ZrZn_2$ [256] and Sc_3In [257] turned out to be very weak itinerant ferromagnetic metals with low Curie temperatures (25 K and 6 K) and small magnetization ($M_{ZrZn_2}(0) = 0.24\ \mu_B$/fu and $M_{Sc_3In}(0) = 0.12\ \mu_B$/fu). Above T_C they obey a Curie–Weiss law but the effective moments deduced from the Curie constants are significant larger compared to those

for the spontaneous moments. Moreover due to the low value of magnetization one cannot include the above materials in any local moment model. The response to this challenge was the theory of spin fluctuations (see the review presented in Reference [258]) and its advanced form of self–consistent renormalization (SCR) theory of spin fluctuations [258, 259].

The concept of spin fluctuations generally specifies "any shift (in time and space) between the instantaneous value of magnetic moments and their mean value given by the molecular field approximation and the Bolzmann statistics" [260]. The kernel idea relies on the thermal excitations of the electron–hole pairs across the Fermi surface; they have a collective character and may be described in terms of spin density fluctuations.

One of the most important quantity used to describe the itinerant electron magnetism is the meas square amplitude of the local density fluctuations $\langle S_L^2 \rangle$ which has a variable nature. It can be generally expressed in terms of the wave–number dependent susceptibility χ_q by assuming certain approximations. A real magnetic material must be then regarded through a proper interpolation between two mutually opposite extreme cases: the local and the extended moment limits. For the case of local moment limit the spin density fluctuations have a local character in real space and can be analyzed like a system of interacting local moments. The local amplitude of spin fluctuations $\langle S_L^2 \rangle$ is large and fixed, only the transverse components being important [261]. In the opposite case of extended moment limit (weak–ferromagnets or exchange–enhanced paramagnets) the amplitude of spin fluctuations is small, only long wave components of the wave–number dependent susceptibility contribute to the magnetic behavior i.e. the spin fluctuations have a local character in reciprocal space (see Figure 5.18 after [259]). Moreover the longitudinal components of spin fluctuations play an important role.

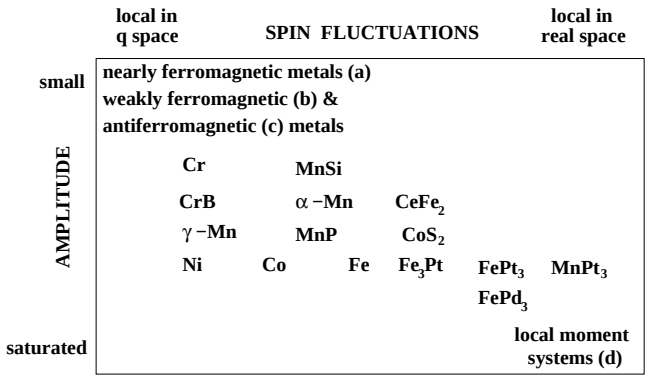

(a) Pd, $HfZn_2$, $TiBe_2$, YCo_2, YRh_6B_4, Ni−Pt alloys, etc.

(b) Sc_3In, $ZrZn_2$, YNi_3, Ni_3Al, $Fe_{0.5}Co_{0.5}Si$, $LaRh_6B_4$, $CeRh_3B_2$, $TiBe_{2-x}Cu_x$, Ni−Pt alloys, etc.

(c) β −Mn, V_3Se_4, V_3S_4, V_5Se_8, Cr−Mo alloys, etc.

(d) magnetic insulator compounds, 4f−metals, Heusler alloys

Figure 5.18: Classification of magnetic materials with respect to the nature of spin fluctuations.

When interpolating between the two extreme cases both transverse and longitudinal components play important roles. A very important prediction of the spin fluctuations theory is the temperature–induced local magnetic moments.

For the low temperature region it was pointed out that the magnetic susceptibility of exchange–enhanced paramagnets is described by:

$$\chi = s\chi_{Pauli}\left[1 + \frac{\pi^2}{6}s^2\left(2\frac{n''(\varepsilon_F)}{n(\varepsilon_F)} - 1.2\frac{n'^2(\varepsilon_F)}{n^2(\varepsilon_F)}\right)T^2 + ...\right] \tag{5.6}$$

where $n(\varepsilon_F)$, $n'(\varepsilon_F)$ and $n''(\varepsilon_F)$ are the density of states and its first and second derivatives at the Fermi level [262, 263]. In Equation 5.6 the field dependence of the susceptibility was leaved out. The above formula shows that an additional temperature dependent term must be included in order to describe the magnetic susceptibility in the low–temperature region. Some years latter it was shown that the thermal variation of susceptibility should be proportional to $T^2 \ln T$ rather than to T^2 [264]. This may lead to a better quantitative account but does not alter the physical meaning of the above equation. The Equation 5.6 indicates that under a favorable distribution of the density of states, the susceptibility may increase with rising temperature. This requires as a necessary condition the density of states to have a strong positive curvature at the Fermi edge ($n''(\varepsilon_F) > 0$). In term of spin fluctuations the thermal dependence of the susceptibility would then indicate a rapid growth of the local amplitude of spin fluctuations with the temperature. Above a temperature T^* the spin fluctuations will reach the saturation owing the charge neutrality requirement. In the high temperature region the susceptibility of exchange–enhanced paramagnets follows a Curie–Weiss law without localized moments. The Curie constant is generally given by the sum of transverse contribution of the localized limit C_t and the longitudinal contribution of the itinerant limit C_l. However the transverse component will be dominant (limit case of local moments with short–range order). The Curie constant is independent from the saturation moment at 0 K being related to the band structure around Fermi level.

The sum of these considerations clearly underlines the importance of the electronic structure when analyzing magnetic properties of itinerant electronic systems.

The temperature dependence of the wave number dependent susceptibility, χ_q, of a strong exchanged enhanced paramagnet is significant only when the q values are small i.e. for small q values χ_q has a large enhancement and the spin fluctuations in this case have a local character in the reciprocal space (see Figure 5.18). The average amplitude of local spin fluctuation

$$\langle S_L^2 \rangle = 3k_B T \sum_q \chi_q \tag{5.7}$$

is a temperature dependent quantity and increases with temperature until it reaches an upper limit determined by the charge neutrality condition at a temperature T^*. The spin fluctuations reach the saturation regime and the effective moments corresponds to a given electron configuration only for systems which show a strong exchange enhanced susceptibility. If the spin fluctuations are saturated, as in systems having very high exchange enhancement factors, S, the effective moments reflect the

electron configuration of the 3d–ion. Below T^* the temperature variation of the local amplitude of spin fluctuations (longitudinal components) determines the magnetic susceptibility. Above T^* only the transversal components of spin fluctuation contribute to the Curie constant. Thus, at $T > T^*$, the alloy behaves as having local moments. The maxima in the χ versus T curves observed in the studied systems may be considered as a cross-over between the low T regime governed by longitudinal spin fluctuations and the classical regime determined by transverse spin fluctuations. A related example is given by the RCo_2 (R = Lu, Y) compounds: values of 3.87 μ_B/Co atom were determined, corresponding to Co^{2+} electron configuration [212, 213]. In $LaNi_5$, since of smaller exchange enhancement factors, the $\langle S_L^2 \rangle$ is not saturated, as shown by the effective Ni moment (2.15 μ_B) smaller as compared to that of Ni^{2+} ion considering only spin contributions (2.82 μ_B).

The experimental data for $LaNi_5$ may be also analyzed in the dynamical mean field theory (DMFT) combined with standard LDA band calculations [265]. In weakly correlated system, the local spin susceptibility is expected to be nearly temperature independent, while in a strongly correlated system, leading Curie–Weiss behavior at high temperatures is expected. For an itinerant electron system, the τ dependence of the correlation function results in the temperature dependence of $\langle S_L^2 \rangle$. Fluctuating moments and atomic like configuration are large at short times. The moment is reduced at longer time scales, corresponding to a more band like less correlated electronic structure near the Fermi level.

In the magnetic behavior of the two investigated systems certain common features are present. For all studied samples the susceptibilities increase as function of temperature up to a value located at T_{max} and then decrease. Above a characteristic temperature T^*, the presence of Curie–Weiss contributions may be observed which decrease when increasing substituent content and are very weak for high x values. The extent to which these features are visible depend on the nature of Ni substitution.

These experimental findings can be analyzed in frame of models which take into account the electron correlation effects in d–bands. Such models are the spin fluctuation model [258, 259] or dynamical mean field theory [266]. These models reconcile the dual character of the electron which as a particle requires a real space description and as a wave, a momentum space description. The temperature induced magnetic moments introduced by *Moryia* for systems having a strong enhanced paramagnetic susceptibility are an important concept from this point of view. The spin fluctuation model considers the balance between the frequencies of longitudinal spin fluctuation which are determined by their lifetime and of transverse fluctuations which are of thermal origin.

For compositions with copper, the experimentally determined nickel moments are smaller than the value characteristic for Ni^{2+} ions, considering only spin contribution (2.83 μ_B/ion) and decrease with increasing Cu content (see Table 5.3).

Two essential different mechanisms may be considered as responsible for this behavior. The first may be related to a possible of diminution of exchange enhancement factor when Ni is replaced by Cu thus resulting in a saturation decreases. Since at $T > T^*$ the $\langle S_L^2 \rangle$ values are not saturated even for $LaNi_5$, the lower exchange enhancement factors can be responsible for the observed behavior. A second mechanism considers a gradual hybridization of the Ni–3d band with Cu states as result

of increasing Cu content i.e. the electronic configuration of nickel must be gradually modified.

The effective mechanism can be identified by employing the information extracted on the electronic structure. The gradual filling of the Ni d band when alloying with Cu should be reflected in the absolute binding energies of the Ni and Cu 2p lines.

In the limit of experimental error, the binding energies of Ni 2p lines show no shifts when compared to pure Ni. This primarily indicates that the number of electrons Ni bands are constant even through alloying and/or the changes are so low that no chemical shift is visible. However the intensity of the well–known Ni 6 eV is altered by the substitutions. For the compositions with Cu the intensity of the mentioned structure is diminished but it still present for x = 1.5. The nature of this satellite is still a matter of debate. The non–zero magnetic moment value on Ni sites or inter–band d–electron hopping mechanisms were previously considered. Recently by using a numerically exact quantum scheme in the LDA + DMFT was possible to reproduce the 6 eV satellite in DOS spectrum of Ni at $T = 0.9 \cdot T_c$ [265]. This satellite was shown to have substantially more spin up contributions. However, regardless of the explanation employed for the nature of the 6 eV feature in Ni compounds [11, 267–269], the lack of the structure is attributed to the gradual filling of the Ni 3d band and/or changes in the electron correlations properties [265].

The position of the Cu $2p_{3/2}$ peak, although at lower binding energy as compared with pure Cu (0.4 eV difference) remains unchanged for all concentrations. The sharpness of the Cu 2p lines additionally support this finding. In fact when it is possible to promote electrons from different sub–shells of the same atoms and thus to reach almost complete or almost uncomplete sub–shells, such shifts are possible and they are actually of non–chemical nature. This is obviously the case of the late d metals. For the particular case of copper, the electrons can be promoted between the 3d and 4s shells. Accounting for the different mean radii of the orbitals $r_{4s}/r_{3d} \approx 3$ such an effect can lead to shifts of the order of a few eV [43]. The non–chemical nature of the Cu 2p shifts in $LaNi_{5-x}Cu_x$ is also supported by the constant position of the peak for all concentrations.

A deeper view can be achieved in the VB region. The hybridization effects between Ni and Cu 3d–states were shown to weak in $LaNi_{5-x}Cu_x$, as evidenced from both XPS valence band results and theoretical calculations. The Cu states behave like almost separated impurity atoms in a $LaNi_5$–lattice. In addition, the Ni d band remains almost unchanged when composition is modified and the Ni 2p XPS core–level lines do not show any shifts which could indicate band–filling effects. Thus, the smaller effective nickel moments as compared to that of Ni^{2+} ion and their decrease when changing the composition cannot be attributed to a gradual filling of the Ni 3d band. The experimentally observed trend may be correlated with the exchange enhancement factors which are not so high, even in $LaNi_5$, to obtain the saturation of spin fluctuations $\langle S_L^2 \rangle$ and decrease as Ni is replaced by Cu. A similar behavior was evidenced in $Y(Co_{1-x}Ni_x)_2$ compounds [213].

The exchange enhancement factors can be calculated from the experimentally obtained low–temperature susceptibilities and the calculated DOS at the Fermi level, as plotted in Figure 5.19. The occurrence of the first mentioned mechanism which is based on the diminution of exchange enhancement factors as the copper content

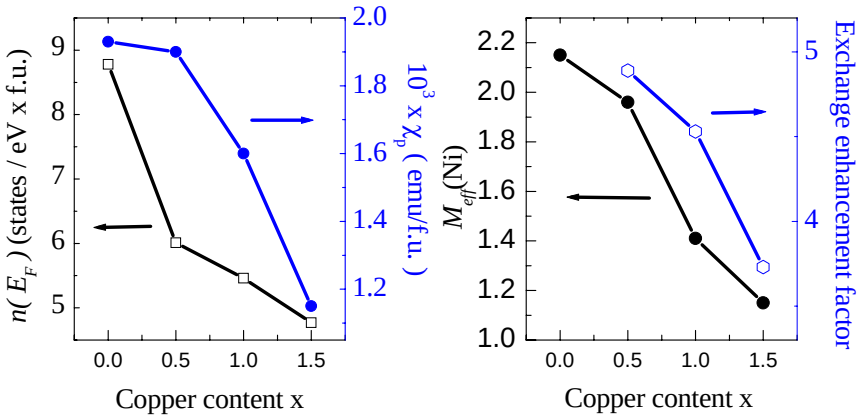

Figure 5.19: Calculated DOS at E_F and measured χ_p for the $LaNi_{5-x}Cu_x$ system (left), as well as deduced effective Ni moment and estimated Stoner exchange enhancement factors (right).

increases, is evident. The reduction of effective nickel moments can be thus associated to the electron–electron correlation effects reflected in the exchange enhancement.

For compositions with aluminum, the situation is somewhat different in spite of the similarities in the magnetic behaviors. The XPS results and band–structure calculations clearly show different changes on the electronic structure of the parent compound $LaNi_5$ when substituting Ni with Me = Cu or Al. For compositions with copper, the corresponding Ni 3d band suffers only minor changes by alloying, a rather independent Cu being formed. The Ni 3d band becomes narrower as increasing Cu content: in the first neighborhood of Ni sites the average number of Ni atoms is lower. As expected from the aluminum DOS and the Al low photo–ionization cross–section [38], for the $LaNi_{5-x}Al_x$ system only low–intensity separate Al features occur. Additionally there is a gradual hybridization of the Ni–3d band with Al–s-p states. However, the shape of the Ni d band is strongly changed by allowing. This is expected to be reflected in differential magnetic behavior of the two investigated series.

The intensity of 6 eV satellite in Ni 2p core–line for $LaNi_5$ is smaller than for pure nickel and vanishes in $LaNi_{5-x}Al_x$ for compositions $x \geq 2$. However the charge transfer from or to nickel atoms, when exists, is very low. This observation is based on the absolute position of the Ni 2p binding energies. The investigated composition range is wider than for the previous system and thus allows the observation of even smaller effective nickel moments. The Ni contributions to the Curie constants are smaller as the aluminum content increases and, in addition, there is an increase of the Pauli paramagnetic terms. These changes are very important for compositions $x > 1$. In case of $LaNi_3Al_2$ the effective nickel moment is only 0.27 μ_B and nearly vanished in $LaNi_2Al_3$.

Consequently for the $LaNi_{5-x}Al_x$ the decrease of effective nickel moments in the high–temperature region can be assigned to changes in the correlation effects of Ni d bands. Some additional charge in the Ni bands, although not excluded should be very low. The nickel is nearly nonmagnetic or even nonmagnetic in $LaNi_2Al_3$ and $LaNi_3Al_2$ as evidenced by magnetic measurements. The small temperature dependent

contributions to susceptibilities, in the above samples, may be also considered as the result of the presence of small clusters of nickel atoms. If this mechanism is present, quantities smaller than 1% of Ni atoms are situated in clusters as result of non–randomly Al substitutions on $6k$ sites. The Al substitution, probably, not in all cases may be made randomly, although the samples were careful prepared.

The factor a in Equation 5.2 can be evaluated from the total DOS according to Equation 5.6. This is presented in Figure 5.20 for the $LaNi_4Al$ compound. The receipt used for the calculation of a is the following: the DOS curve was calculated in a small energy interval around the Fermi level and for this computation a dense mesh in the sampling of the Brillouin region was used. As predicted by Equation 5.6 and expected from the magnetic data, the DOS has a strong positive curvature at the Fermi edge ($n''(\varepsilon_F) > 0$). An interval free from $n'(\varepsilon_F) = 0$ points was chosen and a polynomial fit was performed. A value $a = 0.11 \times 10^{-3}$ K^{-2} was deduced for $LaNi_4Al$.

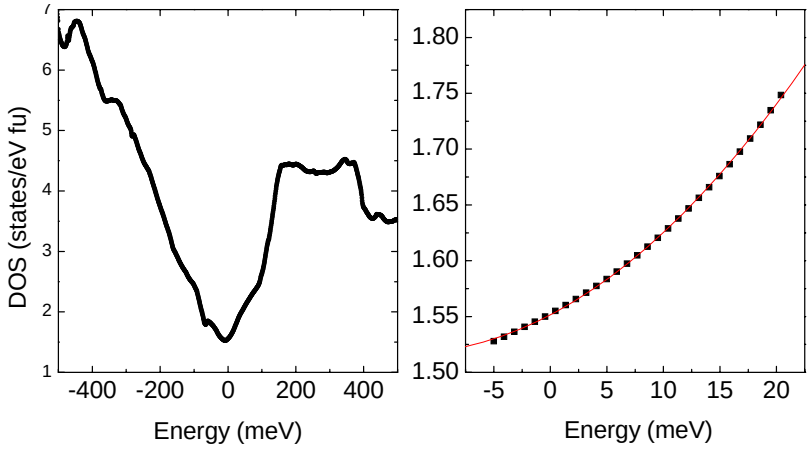

Figure 5.20: Calculated DOS at E_F with fine energy steps for $LaNi_4Al$ (left panel) and the polynomial fit of the DOS dependence around the Fermi level (right panel).

5.7 Conclusions

Joint investigations on the electronic structure and accurate magnetic measurements indicate that $LaNi_5$ is a non–saturated spin fluctuation system. Its common description in the literature as paradigm exchange–enhanced Pauli paramagnet must be reconsidered due to the more complicated magnetic behavior.

The ternary $LaNi_{5-x}Cu_x$ system was also find to be a non–saturated spin fluctuation system. The exchange enhancement factors are not high enough to attain the saturation of $\langle S_L^2 \rangle$ values, as emphasized for x = 0. The XPS measurements and the band structure calculations show that there is a weak hybridization between Cu–d and Ni–d bands. The substitution with Cu does not induce visible changes in the shape of the Ni 3d band. The reduction of the effective nickel moments is due to the diminished Stoner exchange–enhancement factors as the copper content increases.

In $LaNi_{5-x}Al_x$ system there is a transition from a magnetic behavior characterized by temperature induced moments to a Pauli-type paramagnetism when increasing the

aluminium content. This behavior was correlated with the gradual hybridization of Ni–3d bands and diminution of d–electron correlations. The spectroscopic data and the band structure calculations clearly evidenced this gradual hybridization.

Chapter 6

Conclusions and outlook

In the present work spectroscopic investigations on the electronic structure of some interesting materials are presented. The aim was to accomplish a clear view on their electronic properties and then to apply this information in order to answer some specific questions related to their magnetic behavior. The following conclusions can be drawn:

Transition metal dicyanamide compounds

The first spectroscopic results focusing on the electronic structure of $M[N(CN)_2]_2$ (M = Mn, Fe, Ni, Co, Cu) compounds have been presented. By comparison of the XPS spectra recorded for the valence band region and combination of these results with additional XES data, it was shown that the dicyanamide groups act like an organic matrix of the overall electronic structure: the features arising from N and C remain unchanged in the series. The center of gravity of the transition metal 3d valence bands are shifted to lower binding energies as the occupancy of the 3d orbital increases from Mn to Cu. Based on the well described valence band region, an intuitive view of the magnetic relevant orbitals has been generated. The hybridization between the transition metal 3d states and the N 2p and C 2p states increases from Mn to Cu. For $Cu[N(CN)_2]_2$ the maximum of the Cu 3d density of states even coincides with the maximum attributed in the XPS data to the $2p\sigma$ orbitals of the cyano groups. For the compound with Mn the experimental results are in excellent agreement with electronic structure calculations.

Furthermore the magnetic superexchange interaction was discussed, focusing on the factors which are responsible for the occurrence of ferromagnetic interactions via organic bridges. Both structural factors (bond angles and distances) and nature of 3d ion were identified as responsible predictive factors. A particular superexchange pattern was proposed: the crystal structure favors the exchange between full occupied and half–filled 3d orbitals and, according to the nature of the transition metal, this can result in a ferromagnetic interaction for the compounds with Ni or Co. A promising aspect for the future investigations was evidenced for $Ni[N(CN)_2]_2$. The correct order of magnitude for the magnetic ordering temperature was estimated taking into account some spectroscopic results, which is a new approach.

The XPS data for the core–level lines arising from the transition metals were

carefully analyzed with respect to the influence of the screening effects. It was shown that the multiplet splitting of the 3s core–level correlates well with the value of magnetic moment for the sample with Mn. For the other compositions the charge–transfer effects play an important role and become dominant for the compounds with Ni and Cu. A novel numerical procedure was proposed for the modelling of the 3s multiplet splitting in insulators. With this new approach we have evidenced the possibility to evaluate the magnitude of magnetic splitting of the 3s core–level line in new materials even in the case of dominant screening effects in the final state of photoemission.

Six–membered 'ferric–wheel' compound

We report the first XPS/XES data for this compound of special interest in the field of molecular magnetism. The value of the measured 3s multiplet splitting of Fe was explained by higher co–valency effects. This interpretation was found to be consistent with the shape of the 2p core–level line. Judging from the results present in this chapter, it becomes clear that in such metal–organic compounds the charge transfer effects must be carefully analyzed.

The XPS/XES data for the valence band region allowed us to localize the Fe 3d and O 2p states. The hybridization of Fe 3d states with C or N 2p stated was shown to be low. The comparison with calculations of the electronic structure indicates the main contributions of all the structures present in the valence band spectra. From the difference between the energies of the ferromagnetic and antiferromagnetic configurations, the order of magnitude of the exchange coupling constants was determined.

$LaNi_{5-x}Me_x$ (Me = Cu, Al) intermetallic compounds

We present *joint* spectroscopic and computational studies on the electronic structure of $LaNi_5$ and $LaNi_{5-x}Me_x$ compounds. The experimental data on the XPS valence band region were found to be in excellent agreement with the TB–LMTO–ASA band structure calculations. The substitutions with Cu induces no significant changes in the shape of the Ni 3d band, a rather independent Cu band being found. Only a weak hybridization of the Cu and Ni d states was observed. The Ni substitution by Al is marked by strong changes of the Ni valence band, the center of gravity of the 3d bands being shifted to lower binding energies. The hybridization between Ni 3d and Al states is gradually increased for higher Al concentrations.

The accurate magnetic data show that the magnetic behavior of these compounds is more complicated than expected for an exchange–enhanced Pauli paramagnet. $LaNi_5$ has to be regarded as a non–saturated spin fluctuation system. For the $LaNi_{5-x}Cu_x$ series we have concluded that the reduction of effective nickel moments as the copper content increases is due to a reduction of the d–electron correlations which are reflected by the lower Stoner exchange–enhancement factors. Possible filling effects of the Ni 3d bands were ruled out according to the spectroscopic data. The ternary $LaNi_{5-x}Cu_x$ system was found to be a non–saturated spin fluctuation system. In the $LaNi_{5-x}Al_x$ system there is a transition from a magnetic behavior characterized by temperature induced moments to a Pauli–type paramagnetism when increasing the aluminium content. This behavior was correlated with the gradual hybridization of

Ni–3d bands and diminution of d–electron correlations, as deduced from the spectroscopic data and the computational results.

Outlook

In order to achieve a broader view on the role of transition metals in the electronic structure of $M[N(CN)_2]_2$ compounds, more compositions are necessary to be investigated. While $Co[N(CN)_2]_2$ is expected to obey the trends indicated by the presented results, compositions with less than 5 electrons on the d shell are of high interest. Additional computational efforts are requested for the compounds with Fe, Ni and Cu in order to gain a consistent picture of the electronic and magnetic properties.

Further oxo–bridged iron clusters will be investigated in Osnabrück in the next future. The importance of these studies is underlined by the novelty of spectroscopic investigations on this kind of materials. Further computational efforts are requested in order to describe the values of magnetic exchange coupling in the 'ferric–wheel'.

Investigations on intermetallic $LaNi_{5-x}Me_x$ with Me = 3d transition metals are the next step in the study of the compounds derived from $LaNi_5$. Some data are nowadays available for x = 1 and M = Fe, Mn and so forth, but joint experimental and theoretical studies still remain to be performed.

Acknowledgements

In the first place I would especially like to thank apl. Prof. Dr. Manfred Neumann for his constant and invaluable support. Each time an interesting scientific question came up, his appeal for insight discussions and interpretation of the experimental data results helped me move on and gave me valuable hints. His encouragement and advices consistently assisted my work in Osnabrück.

My special thanks go to Prof. Dr. Emil Burzo for guiding me through the field of magnetism ever since I was a student at the 'Babeş–Bolyai' University of Cluj–Napoca. The enjoyable and fruitful collaboration with him is certainly the reason for my scientific activity in the field of magnetism. Prof. Dr. Burzo is also acknowledged for the fruitful co–operation on intermetallic compounds.

I am indebted to Prof. Dr. Ernst Z. Kurmaev for the consistent collaboration on several interesting systems. He is also acknowledged for the supply of the emission and absorption data for the dicyanamide materials.

Dr. Andrei V. Postnikov has been a steady dialog partner during the last half of my stay in Osnabrück. The discussions with him helped me clarify several underlying aspects concerning the relationship between magnetism and electronic structure. He is gratefully acknowledged for performing the theoretical calculations for the 'ferric–wheel' and for his patience, advices and support concerning the use of TB–LMTO code.

I was fortunate to meet Prof. Dr. Marin Coldea for several times in Osnabrück. His natural talent as lecturer helped me to understand essential aspects of magnetism.

During my stay in Osnabrück I had the opportunity and pleasure to meet several guests of Prof. Neumann. I was lucky to collaborate with Prof. Dr. Andrej Ślebarski on magnetism in correlated metallic systems. He is also acknowledged for the very interesting and substantial discussions. The discussions with Dr. Vadim R. Galakhov helped me get a clear view on the 3s multiplet splitting in transition metal insulators. Prof. Dr. Viorica Simon is acknowledged for the collaboration in the field of glasses.

Former and actual colleagues are acknowledged for the very pleasant working atmosphere: Markus Bach, Stefan Bartkowski, Vasile Caciuc, Mihaela Demeter, Werner Dudas, Franz Fangmeyer, Daniela Hartmann, Karsten Küpper, Thorsten Mayer, Bolormaa Sanduijav, Dr. Bernd Schneider, Dr. Helmut Schürmann and Dr. Stefan Plogmann.

Special thanks to Mihaela: your friendship means a lot to me. For her kindness and true help especially during the first part of my stay in Germany, Daniela remains the kind colleague anyone would like to meet at the workplace. It has been a pleasure to share the office with Bernd. I was able to solve many technical problems only with the help coming from Werner.

The work in the Department of Physics was more enjoyable thanks to the friendly and uncomplicated administrative assistance of Ms. Anna–Klara Ostendorf, Ms. Marion von Landsberg and Ms. Birgit Guss.

The financial support of the Deutsche Forschungsgemeinschaft and the Osnabrück University are gratefully acknowledged.

At last, but not least, I am grateful to Paqui and my family for their support. Sincere thanks to Paqui for her constant encouragements and the patience spent during the last months. Without the effort of my family during the physics study in Romania I would not be able to present this work. During the last years they have been with me every moment in spite of the distance which separated us.

Bibliography

[1] W. Hallwachs, "Über den Einfluß des Lichtes auf elektrostatisch geladene Körper," *Wiedemann'sche Annalen*, vol. 33, pp. 301–312, 1888.

[2] H. Hertz, "Über den Einfluß des ultravioletten Lichtes auf die elektrische Entladung," *Wiedemann'sche Annalen*, vol. 31, pp. 983–1000, 1887.

[3] J. J. Thomson, "Cathode Rays," *Philosophical Magazine*, vol. 44, pp. 293–316, 1897.

[4] A. Einstein, "Über einen die erzeugung und verwandlung des lichtes betreffenden heuristichen gesichtspunkt," *Annalen der Physik*, vol. 17, pp. 132–148, 1905.

[5] C. N. Berglund and W. Spiecer, "Photoemission studies of copper and silver: Theory," *Physical Review*, vol. 136, pp. A1030–A1044, 1964.

[6] K. Siegbahn, C. Nordling, A. Fahlman, R. Nordberg, K. Hamrin, J. Hedman, G. Johansson, T. Bergmark, S. E. Karlson, I. Lindgren, and B. Lindberg, *ESCA–Atomic, Molecular and Solid State Structure Studied by Means of Electron Spectroscopy.* Almquist and Wicksell, Uppsala, 1967.

[7] K. Siegbahn, C. Nordling, G. Johansson, J. Hedman, P. F. Heden, K. Hamrin, U. Gelius, T. Bergmark, L. O. Werme, R. Manne, and Y. Baer, *ESCA Applied to Free Molecules.* North Holland, Amsterdam, 1969.

[8] K. Siegbahn, D. Hammond, H. Fellner-Feldegg, and E. F. Barnett, "Electron spectroscopy with monochromatized X–rays," *Nature*, vol. 176, pp. 245–252, 1972.

[9] H. P. Bonzel and C. Client, "On the history of photoemission," *Progress in Surface Science*, vol. 49, pp. 107–153, 1995.

[10] G. Ertl and J. Küppers, *Low Energy Electrons and Surface Chemistry.* VCH, Weinheim, 1985.

[11] S. Hüfner, *Photoelectron spectroscopy.* Springer–Verlag, Berlin, 1995.

[12] C. Fadley, "Basic Concepts of X-ray Photoelectron Spectrocopy," in *Electron Spectroscopy: Theory, Techniques and Applications* (C. Brundle and P. Backer, eds.), vol. 2, pp. 2–156, Academic Press, London, 1978.

[13] C. Cohen-Tannoudji, B. Diu, and F. Laloë, *Quantenmechanik*, vol. 2. Walter de Gruyter, Berlin, 1999.

[14] G. Borstel, "Theoretical aspects of photoemission," *Applied Physics A*, vol. 38, pp. 193–204, 1985.

[15] W. Nolting, "Influence of electron correlations on auger electron – and appearance potential – spectra of solids," *Zeitschrift für Physik – Condensed Matter*, vol. 80, pp. 73–86, 1990.

[16] J. C. Fuggle, R. Lässer, O. Gunnarsson, and K. Schönhammer, "Plasmon Gains as a Monitor of Incomplete Relaxation, Interference Effects, and the Transition from Sudden to Adiabatic Limits in Electron Spectroscopies," *Physical Review Letters*, vol. 44, pp. 1090–1093, 1980.

[17] J. D. Lee, O. Gunnarsson, and L. Hedin, "Transition from the adiabatic to the sudden limit in core-level photoemission: A model study of a localized system," *Physical Review B*, vol. 60, pp. 8034–8049, 1999.

[18] T. Koopmans, "Über die Zuordnung von Wellenfunktionen und Eigenwerten zu den eizelnen Elektronen eines Atoms," *Physica*, vol. 1, pp. 104–113, 1933.

[19] R. J. Powell and W. E. Spicer, "Optical properties of NiO and CoO," *Physical Review B*, vol. 2, pp. 2182–2193, 1970.

[20] C. Powell, "Attenuation lenghts of low–energy electrons in solids," *Surface Science*, vol. 44, pp. 29–46, 1974.

[21] J. C. Shelton, "Inelastic mean free paths for electrons in bulk jellium," *Surface Science*, vol. 44, pp. 305–309, 1974.

[22] H. Bethe, "Zur Theorie des Durchgangs schneller Korpuskulastrahlung durch Materie," *Annalen der Physik*, vol. 5, pp. 325–400, 1930.

[23] S. Tanuma, C. J. Powell, and D. R. Penn, "Proposed formula for electron inelastic mean free paths based on calculations for 31 materials," *Surface Science*, vol. 192, pp. L849–L857, 1987.

[24] S. Tanuma, C. J. Powell, and D. R. Penn, "Calculations of inelastic mean free paths for 31 materials," *Surface and Interface Analysis*, vol. 11, pp. 577–589, 1988.

[25] J. C. Ashley, "Interaction of low–energy electrons with condensed matter: stopping powers and inelastic mean free paths from optical data," *Journal of Electron Spectroscopy and Related Phenomena*, vol. 46, pp. 199–214, 1988.

[26] S. Tanuma, C. J. Powell, and D. R. Penn, "Calculations of inelastic mean free paths: II. Data for 27 elements over 50–2000 eV range," *Surface and Interface Analysis*, vol. 17, pp. 911–926, 1991.

[27] S. Tanuma, C. J. Powell, and D. R. Penn, "Calculations of inelastic mean free paths: III. Data for 15 inorganic compounds over 50–2000 eV range," *Surface and Interface Analysis*, vol. 17, pp. 927–939, 1991.

[28] S. Tanuma, C. J. Powell, and D. R. Penn, "Calculations of electron inelastic mean free paths (IMFPs): IV. Evaluation of calculated of calculated IMFPs formula TPP–2 for electron energies between 50 and 2000 eV," *Surface and Interface Analysis*, vol. 20, pp. 77–89, 1993.

[29] S. Tanuma, C. J. Powell, and D. R. Penn, "Calculations of inelastic mean free paths: V. Data for 14 organic compounds over 50–2000 eV range," *Surface and Interface Analysis*, vol. 21, pp. 165–176, 1993.

[30] A. Jablonski, "Universal energy dependence of the inelastic mean free path," *Surface and Interface Analysis*, vol. 20, pp. 317–321, 1993.

[31] J. Pendry, "Theory of Photoemision," *Surface Science*, vol. 57, pp. 679–705, 1976.

[32] D. J. Spanjaard, D. W. Jepsen, and P. M. Marcus, "Effects of transmission factors and matrix elements on angular distribution of photoemission from Ag(111)," *Physical Review B*, vol. 15, pp. 1728–1737, 1977.

[33] T. Schlathölter, *Theorie der spinpolarisierten Core–Level Spektroskopie für Photo– und Auger–Elektronen*. PhD thesis, Universität Osnabrück, 1999.

[34] N. W. Ashcroft and N. D. Mermin, *Solid State Physics*. Rinehart & Winston, New York, 1976.

[35] V. I. Nefedof, N. P. Sergushin, I. M. Band, and M. B. Trzhaskovskaya, "Relative intensities in x–ray photoelectron spectra," *Journal of Electron Spectroscopy and Related Phenomena*, vol. 2, pp. 383–403, 1973.

[36] R. F. Reilman, A. Msezane, and S. T. Manson, "Relative intensities in x–ray photoelectron spectra," *Journal of Electron Spectroscopy and Related Phenomena*, vol. 8, pp. 389–394, 1975.

[37] J. H. Scofield, "Hartree–Slater subshell photoionization cross–section at 1254 and 1487 eV," *Journal of Electron Spectroscopy and Related Phenomena*, vol. 8, pp. 129–137, 1976.

[38] J. J. Yeh and I. Lindau, "Atomic subsell photoionization cross sections and asymmetry parameters: $1 \leq z \leq 103$," *Atomic Data and Nuclear Data Tables*, vol. 32, pp. 1–155, 1985.

[39] D. Briggs and J. C. Rivière, "Spectral Interpretation," in *Practical Surface Analysis by Auger and X-ray Photoelectron spectroscopy* (D. Briggs and M. P. Seah, eds.), vol. 1, pp. 87–140, John Wiley & Sons, Chichester, 1983.

[40] U. Gelius, "Binding Energies and Chemical Shifts in ESCA," *Physica Scripta*, vol. 9, pp. 133–147, 1974.

[41] V. Nefedov, *Photoelectron Spectroscopy of Solid Surfaces*. VSP, Utrecht, 1988.

[42] T. L. Barr, E. Hoppe, T. Dugall, P. Shah, and S. Seal, "XPS and bonding: when and why can relaxation effects be ignored," *Journal of Electron Spectroscopy and Related Phenomena*, vol. 99, pp. 95–103, 1999.

[43] P. S. Bagus, F. Illas, G. Pacchioni, and F. Parmigiani, "Mechanisms responsibe for chemical shifts of core–level binding energies and their relantionship to chemical bonding," *Journal of Electron Spectroscopy and Related Phenomena*, vol. 100, pp. 215–236, 1999.

[44] L. Hedin, "Many–Body Effects," in *X-Ray Spectroscopy* (L. V. Azároff, ed.), pp. 226–283, Mc Graw–Hill Book Company, New York, 1974.

[45] T. Novakov, "X–Ray Photoelectron Spectroscopy of Solids; Evidence of Band Structure," *Physical Review B*, vol. 3, pp. 2693–2698, 1971.

[46] G. Wertheim, R. Cohen, A. Rosencweig, and H. Guggenheim, "Multiplet splitting and two electron excitations in the trivalent rare–earths," in *Electron Spectroscopy* (D. A. Shirley, ed.), pp. 813–820, North–Holland, Amsterdam, 1972.

[47] K. Kim and R. Davis, "Electron Spectroscopy of Nickel–Oxygen System," *Journal of Electron Spectroscopy and Related Phenomena*, vol. 1, pp. 251–258, 1972.

[48] K. Kim, "X–ray–photoelectron spectroscopic studies of the electronic structure of CoO," *Physical Review B*, vol. 11, pp. 2177–2185, 1975.

[49] G. V. der Laan, C. Westra, C. Haas, and G. A. Sawatzky, "Satellite structure in photoelectron and auger spectra of copper dihalides," *Physical Review B*, vol. 23, pp. 4369–4380, 1981.

[50] B. Veal and A. Paulikas, "Final–state screening and chemical shifts in photoelectron spectroscopy," *Physical Review B*, vol. 31, pp. 5399–5416, 1985.

[51] S. Uhlenbrock, *Untersuchungen zur elektronischen Struktur einfacher Übergangsmetall–Oxide – unter besonderer Berücksichtigung des Nickel–Oxide*. PhD thesis, Universität Osnabrück, 1994.

[52] J. M. Hollas, *High resolution spectroscopy*. Butterworths & Co, London, 1982.

[53] G. D. Mahan, "Excitons in Metals: Infinite Hole Mass," *Physical Review*, vol. 163, pp. 612–617, 1967.

[54] P. Nozières and C. T. D. Dominicis, "Singularities in the X–Ray Absorption and Emission of Metals. III. One-Body Theory Exact Solution," *Physical Review*, vol. 178, pp. 1097–1107, 1969.

[55] S. Doniach and M. Šunjić, "Many–electron singularity in X–ray photoemission and X–ray line spectra from metals," *Journal of Physics C*, vol. 3, pp. 285–291, 1970.

[56] M. Cardona and L. Ley, *Photoemission in Solids I*. Springer Verlag, Berlin, Heidelberg, 1978.

[57] C. S. Fadley, D. A. Shirley, A. J. Freeman, P. S. Bagus, and J. V. Mallow, "Multiplet Splitting of Core–Electron Binding Energies in Transition–Metal Ions," *Physical Review Letters*, vol. 23, pp. 1397–1401, 1969.

[58] C. S. Fadley and D. A. Shirley, "Multiplet Splitting of Metal–Atom Electron Binding Energies," *Physical Review A*, vol. 2, pp. 1109–1120, 1970.

[59] J. C. Carver, G. K. Schweitzer, and T. A. Carlson, "Use of the X-Ray Photoelectron Soectroscopy to Study Bonding in Cr, Mn, Fe, and Co Compounds," *Journal of Chemical Physics*, vol. 57, pp. 973–982, 1972.

[60] G. K. Wertheim, S. Hüfner, and H. J. Guggenheim, "Systematics of Core–Electron Exchange Splitting in 3d–Group Transition–Metal Compounds," *Physical Review B*, vol. 7, pp. 556–558, 1973.

[61] J. H. V. Vleck, "The Dirac Vector Model in Complex Spectra," *Physical Review*, vol. 45, pp. 405–419, 1934.

[62] S. Hüffner and G. K. Wertheim, "Core–Electron Splittings and Hyperfine Fields in Transition-Metal Compounds," *Physical Review B*, vol. 7, pp. 2333–2336, 1973.

[63] F. R. McFeely, S. P. Kowalczyk, L. Ley, and D. A. Shirley, "Evidence for a localized magnetic moment in paramagnetic α–Mn from multiplet splitting," *Solid State Communications*, vol. 15, pp. 1051–1054, 1974.

[64] F. van Acker, Z. M. Stadnik, J. C. Fuggle, H. J. W. M. Hoekstra, K. H. J. Buschow, and G. Stroink, "Magnetic moments and x–ray photoelectron spectroscopy splittings in Fe 3s core levels of materials containing Fe," *Physical Review B*, vol. 37, pp. 6827–6834, 1988.

[65] P. S. Bagus, A. J. Freeman, and F. Sasaki, "Prediction of New Multiplet Structure in Photoemission Experiments," *Physical Review Letters*, vol. 30, pp. 850–853, 1973.

[66] E.-K. Viinikka and Y. Öhrn, "Configuration mixing in the 3s–hole state of transition-metal ions," *Physical Review B*, vol. 11, pp. 4168–4175, 1975.

[67] B. W. Veal and A. P. Paulikas, "X–Ray–Photoelectron Final–State Screening in Transition–Metal Compounds," *Physical Review Letters*, vol. 51, pp. 1995–1998, 1983.

[68] V. Kinsinger, I. Sander, P. Steiner, R. Zimmermann, and S. Hüfner, "Screening and exchange splitting in core level XPS," *Solid State Communications*, vol. 73, pp. 527–530, 1990.

[69] S. J. Oh, G. H. Gweon, and J. G. Park, "Origin of the 3s splittings in the Photoemission Spectra of Mn and Fe Insulation Compounds," *Physical Review Letters*, vol. 68, pp. 2850–2853, 1992.

[70] K. Okada and A. Kotani, "Interatomic and Intra-atomic Configuration Interactions in Core–Level X–Ray Photoemission Spectra of Late Transition–Metal Compounds," *Journal of the Physical Society of Japan*, vol. 61, pp. 4619–4637, 1992.

[71] K. Okada, A. Kotani, V. Kinsinger, R. Zimmermann, and S. Hüfner, "Photoemission from Cr 2p and 3s levels of CrF_2," *Journal of the Physical Society of Japan*, vol. 63, pp. 2410–2415, 1994.

[72] T. Uozumi, K. Okada, A. Kotani, R. Zimmermann, P. Steiner, S. Hüfner, Y. Tezuka, and S. Shin, "Theoretical and experimental studies on the electronic structure of M_2O_3 (M = Ti, V, Cr, Mn, Fe) compounds by systematic analysis of high–energy spectroscopy," *Journal of Electron Spectroscopy and Related Phenomena*, vol. 83, pp. 9–20, 1997.

[73] F. U. Hillebrecht, R. Jungblut, and E. Kisker, "Spin Polarization of the Metallic Fe 3s Photoemission Spectrum," *Physical Review Letters*, vol. 65, pp. 2450–2453, 1983.

[74] A. K. See and L. E. Klebanoff, "Spin–resolved nature of 3s photoemission from ferromagnetic iron," *Physical Review B*, vol. 51, pp. 7901–7904, 1995.

[75] Z. Xu, Y. Liu, P. D. Johnson, B. Itchkawitz, K. Randall, J. Feldhaus, and A. Bradshaw, "Spin polarized photoemission study of the Fe 3s multiplet," *Physical Review B*, vol. 51, pp. 7912–7915, 1995.

[76] W. J. Lademan and L. E. Klebanoff, "Investigation of satellites associated with Fe 3s photoemission," *Physical Review B*, vol. 55, pp. 6766–6769, 1997.

[77] F. U. Hillebrecht, T. Kinoshita, C. Roth, H. B. Rose, and E. Kisker, "Spin resolved Fe and Co 3s photoemission," *Journal of Magnetism and Magnetic Materials*, vol. 212, pp. 201–210, 2000.

[78] F. Parmigiani and L. Sangaletti, "Electronic correlation effects in the Ni 3s and Co 3s X–ray photoelectron spectra of NiO, CoO, K_2NiF_4 and K_2CoF_4," *Chemical Physics Letters*, vol. 213, pp. 613–618, 1993.

[79] L. Sangaletti, L. E. Depero, P. S. Bagus, and F. Parmigiani, "A proper Anderson Hamiltonian treatment of the 3s photoelectron spectra of MnO, FeO, CoO and NiO," *Chemical Physics Letters*, vol. 245, pp. 463–468, 1995.

[80] D. A. Shirley, "High–resolution X–ray photoemission spectrum of the valence band of gold," *Physical Review B*, vol. 5, pp. 4709–4714, 1972.

[81] S. Tougaard and P. Sigmund, "Influence of elastic and inelastic scattering on energy spectra of electrons emitted from solids," *Physical Review B*, vol. 25, pp. 4452–4466, 1982.

[82] S. Tougaard and B. Jørgensen, "Inelastic Background Intensities in XPS Spectra," *Surface Science*, vol. 143, pp. 482–494, 1984.

[83] S. Tougaard, "Low Energy Inelastic Electron Scattering Properties of Noble and Transition Metals," *Solid State Communications*, vol. 61, pp. 547–559, 1987.

[84] S. Tougaard, "Quantitative analysis of the inelastic background in surface electron spectroscopy," *Surface and Interface Analysis*, vol. 11, pp. 453–472, 1988.

[85] H. S. Hansen and S. Tougaard, "Separation of spectral components and depth profiling through inelastic background analysis of XPS spectra with overlapping peaks," *Surface and Interface Analysis*, vol. 17, pp. 593–607, 1991.

[86] S. Tougaard, "Universality classes of inelastic electron scattering cross–sections," *Surface and Interface Analysis*, vol. 25, pp. 137–154, 1997.

[87] S. Tougaard, H. S. Hansen, and M. Neumann, "Test on validity of recent formalism for quantitative XPS/XAS," *Surface Science*, vol. 244, pp. 125–134, 1991.

[88] S. Tougaard and C. Jansson, "Background correction in XPS: correction of validity of different methods," *Surface and Interface Analysis*, vol. 19, pp. 171–174, 1992.

[89] S. Tougaard and C. Jansson, "Comparison of validity and consistency of methods for quantitative XPS analysis," *Surface and Interface Analysis*, vol. 20, pp. 1013–1046, 1993.

[90] S. Lütkehoff, *Untersuchungen zur elektronischer Struktur Seltener Erdoxide mittels der Röntgenphotoelektronenspektroskopie*. PhD thesis, Universität Osnabrück, 1998.

[91] P. Auger, "Sur l'Effect Photoelectrique Commpose," *Le Journal de Physique et le Radium*, vol. 6, pp. 205–208, 1925.

[92] J. C. Riviére, "Surface Analytical Techniques," in *Monographs on the Physics and Chemistry of Materials* (H. Frölich, P. B. Hirsch, N. F. Mott, A. J. Heeger, and R. Brooke, eds.), pp. 53–64, Clarendon Press, Oxford, 1990.

[93] T. Albers, *Untersuchung ionenstoßinduzierter Effecte bei der Tiefenprofileanalyse an oxidischen Multischichtsystemen mittels Röntgenphotoelectronenspektroskopie*. PhD thesis, Universität Osnabrück, 1994.

[94] J. Cazaux, "Mechenisms of charging in electron spectroscopy," *Journal of Electron Spectroscopy and Related Phenomena*, vol. 105, pp. 155–185, 1990.

[95] J. Cazaux, "About the charging compensation of insulating samples in XPS," *Journal of Electron Spectroscopy and Related Phenomena*, vol. 113, pp. 15–33, 2000.

[96] P. J. Cumpson, M. P. Seah, and S. J. Spencer, "Calibration of Auger and X–ray photoelectron spectrometers for valid analytical measurements," *Spectroscopy Europe*, vol. 10/3, pp. 2–5, 1998.

[97] "MultiTechnique XPS/ESCA Operators's Reference, Version 5.2." Perkin Elmer, Physical Electronics Division.

[98] F. de Groot, "High–Resolution X–ray Emission and X–ray Absorption Spectroscopy," *Chemical Reviews*, vol. 101, pp. 1779–1808, 2001.

[99] A. Kotani, "Theory of resonant X–ray emission spectra in strongly correlated electron systems," *Journal of Electron Spectroscopy and Related Phenomena*, vol. 110–111, pp. 197–212, 2000.

[100] A. Kotani, "Resonant inelastic X–ray scattering spectra for electrons in solids," *Reviews of Modern Physics*, vol. 73, pp. 203–246, 2001.

[101] "High Resolusion und Flux for Materials and Surface Science · Beamline 8.0.1." Advanced Light Source, datasheet, 2000.

[102] "Soft X–ray Fluorescence Spectrometer · Beamline 8.0.1." Advanced Light Source, datasheet, 2000.

[103] P. S. Peercy, "The drive to miniaturization," *Nature*, vol. 406, pp. 1023–1026, 2000.

[104] M. C. Petty, M. R. Bryce, and D. Bloor, *Introduction to Molecular Electronics*. Edward Arnold, London, 1995.

[105] M. Verdaguer, "Molecular Electronics Emerges from Molecular Magnetism," *Science*, vol. 272, pp. 698–699, 1996.

[106] O. Kahn and C. J. Martinez, "Spin–Transition Polymers: From molecular materials toward memory devices," *Science*, vol. 279, pp. 44–48, 1998.

[107] A. Thiaville and J. Miltat, "Small is beautiful," *Science*, vol. 284, pp. 133–135, 1999.

[108] M. N. L. und D. Loss, "Quantum computing in molecular magnets," *Nature*, vol. 284, pp. 789–793, 2001.

[109] "IBM Travelstar^{TM} 80GN 2.5–inch hard disk drive." IBM, Travelstar 80GN Datasheet, June 2002.

[110] M. Albrecht, C. T. Moser, M. E. Beast, and B. D. Terris, "Recording performance of high–density patterned perpendicular magnetic media," *Applied Physics Letters*, vol. 81, pp. 2877–2878, 2002.

[111] "Fujitsu Develops HDD Read–Head Technology for 300Gb/in^2 Densities." Fujitsu Press Release, Tokyo, Japan, May 2002.

[112] J. S. Miller and A. J. Epstein, "Prescription for stabilization of ferromagnetic exchange in molecular solids via admixing of the ground state with virtual charge–transfer exited state," *Journal of the American Chemical Society*, vol. 109, pp. 3850–3855, 1987.

[113] J. S. Miller and A. J. Epstein, "Molecular/organic ferromagnets," *Science*, vol. 240, pp. 40–47, 1988.

[114] M. Kinoshita, P. Turek, M. Tamura, K. Nozava, D. Shiomi, Y. Nakazava, M. Ishikava, M. Takahashi, K. Awaga, T. Inabe, and Y. Maruyama, "An organic radical ferromagnet," *Chemistry Letters*, vol. 7, pp. 1225–1228, 1991.

[115] R. Sessoli, D. Gatteschi, A. Caneschi, and M. A. Novak, "Magnetic bistability in a metal ion cluster," *Nature*, vol. 365, pp. 141–143, 1994.

[116] M. A. Novak, R. S. A. Caneschi, and D. Gatteschi, "Magnetic properties of a Mn cluster organic–compound," *Journal of Magnetism and Magnetic Materials*, vol. 146, pp. 211–213, 1995.

[117] A. Caneschi, D. Gatteschi, C. Sangregorio, R. Sessoli, L. Sorace, A. Cornia, M. A. Novak, C. Paulsen, and W. Wernsdorfer, "The molecular approach to nanoscale magnetism," *Journal of Magnetism and Magnetic Materials*, vol. 200, pp. 182–201, 1999.

[118] O. Kahn, *Molecular Magnetism*. VCH, Weinheim, 1993.

[119] H. Lueken, *Magnetochemie*. B. G. Teubner, Stuttgart Leipzig, 1999.

[120] M. Verdaguer, A. Bleuzen, V. Marvaud, J. Vaissermann, M. Seuleiman, C. Desplanches, A. Scuiller, C. Train, R. Garde, G. Gelly, C. Lomenech, I. Rosenman, P. Veillet, C. Cartier, and F. Villain, "Molecules to build solids: high rmT_C molecule–based magnets by design and recent revival of cyano complexes chemistry," *Coordination Chemistry Reviews*, vol. 190, pp. 1023–1047, 1999.

[121] J. C. Goodwin, R. Sessoli, D. Gatteschi, W. Wernsdorfer, A. K. Powell, and S. L. Heath, "Towards nanostructured arrays of single molecule magnets: new Fe_19 oxyhydroxide clusters displaying high ground state spins and hysteresis," *Journal of the Chemical Society, Dalton Transactions*, pp. 1835–1841, 2000.

[122] B. Barbara, L. Thomas, F. Lionti, I. Chiorescu, and A. Sulpice, "Macroscopic quantum tunneling in molecular magnets," *Journal of Magnetism and Magnetic Materials*, vol. 200, pp. 167–181, 1999.

[123] P. Gütlich, A. Hauser, and H. Spiering, "Thermisch und optisch schaltbare Eisen(II)–Komplexe," *Angewande Chemie*, vol. 106, p. 2109, 1994.

[124] D. Gatteschi, "Molecular Magnetism : A Basis for New Materials," *Advanced Materials*, vol. 6, pp. 635–645, 1994.

[125] A. Jordan, P. Wust, H. Fähnling, W. John, A. Hinz, and R. Felix, "Inductive heating of ferrimagnetic particles and magnetic fluids: physical evaluat ion of their potential for hyperthermia," *International Journal of Hyperthermia*, vol. 9, p. 51, 1993.

[126] S. Gider, D. D. Awschalom, T. Douglas, S. Mann, and M. Chaprala, "Classical and quantum magnetic phenomena in natural and artificial ferritin proteins," *Science*, vol. 268, pp. 77–??, 1995.

[127] J. Schnack, "Magnetic properties of deposited Polyoxometalates." Talk at the Block seminar, Bramsche, Germany, October 2002.

[128] H. Koehler, A. Kolbe, and G. Lux, "Zur Struktur der Dicyanamide zweiwertiger 3d–Metalle $M(N(CN)_2)_2$," *Zeitschrift für Anorganische und Allgemeine Chemie*, vol. 428, pp. 103–112, 1977.

[129] M. Kurmoo and C. J. Kepert, "Hard magnets based on transition metal complexes with the dicyanamide anion, $N(CN)_2-$," *New Journal of Chemistry*, vol. 22, pp. 1515–1524, 1998.

[130] S. R. Batten, P. Jensen, B. Moubaraki, K. S. Murray, and R. Robson, "Structure and molecular magnetism of the rutile–related compounds $M(dca)_2$, $M = Co^{II}, Ni^{II}, Cu^{II}$, dca = dicyanamide, $N(CN)_2-$," *Chemistry Communications*, pp. 439–440, 1998.

[131] J. L. Manson, C. R. Kmety, , Q. Huang, J. W. Lynn, G. M. Bendele, S. Pagola, P. W. Stephens, L. M. Liable-Sands, A. L. R. A. J. Epstein, and J. S. Miller, "Structure and Magnetic Ordering of $M^{II}[N(CN)_2]_2$ $(M = Co, Ni)$," *Chemistry of Materials*, vol. 10, pp. 2552–2553, 1999.

[132] M. Kurmoo and C. J. Kepert, "Magnetic materials containing the dicyanamide anion, $N(CN)_2-$," *Molecular Crystals and Liquid Crystals*, vol. 334, pp. 693–702, 1999.

[133] C. R. Kmety, J. L. Manson, Q. Huang, J. W. Lynn, R. W. Erwin, J. S. Miller, and A. J. Epstein, "Collinear ferromagnetism and spin orientation in the molecule–based magnets $M[N(CN)_2]_2$ $(M = Co, Ni)$," *Physical Review B*, vol. 60, pp. 60–63, 1999.

[134] J. L. Manson, C. R. Kmety, A. J. Epstein, and J. S. Miller, "Spontaneous Magnetization in the $M[N(CN)_2]_2$ $(M = Cr, Mn)$ Weak Ferromagnets," *Inorganic Chemistry*, vol. 38, pp. 2552–2553, 1999.

[135] C. R. Kmety, Q. Huang, J. W. Lynn, R. W. Erwin, J. L. Manson, S. McCall, J. E. Crow, K. L. Stevenson, J. S. Miller, and A. J. Epstein, "Noncollinear antiferromagnetic structure of the molecule–based magnet $Mn[N(CN)_2]_2$," *Physical Review B*, vol. 62, pp. 5576–5588, 2000.

[136] M. Kurmoo, "Rutile and layered magnets based on transition metal complexes containing dicyanamide and tricyanomethanide," *Molecular Crystals and Liquid Crystals*, vol. 342, pp. 167–176, 2000.

[137] J. L. Manson, C. R. Kmety, F. Palacio, A. J. Epstein, and J. S. Miller, "Low–Field Remanent Magnetization in the Weak Ferromagnet $Mn[N(CN)_2]_2$. Evidence for Spin–Flop Behaviour," *Chemistry of Materials*, vol. 13, pp. 1068–1073, 2001.

[138] C. R. Kmety, J. L. Manson, S. McCall, J. E. Crow, K. L. Stevenson, and A. J. Epstein, "Low-temperature specific heat of the molecule-based magnet $M[N(CN)_2]_2$. (M = Co, Ni, Cu, Zn) series," *Journal of Magnetism and Magnetic Materials*, vol. 248, pp. 52–61, 2002.

[139] J. S. Miller and A. J. Epstein, "Organische und metallorganische molekulare magnetische materialien: Designer–Magnete," *Angewandte Chemie*, vol. 106, pp. 399–432, 1994.

[140] W. Plass, "Design magnetischer Materialien: Chemie der Magnete," *Chemie in unserer Zeit*, vol. 6, pp. 323–333, 1994.

[141] G. Beamson and D. Briggs, *High Resolution XPS of Organic Polymers: the Scienta ESCA300 Database*. Wiley, Chichester, 1992.

[142] F. Parmigiani and L. Sangaletti, "Fine structures in the X–ray photoemission spectra of MnO, FeO, CoO, and NiO single crystals," *Journal of Electron Spectroscopy and Related Phenomena*, vol. 98–99, pp. 287–302, 1999.

[143] M. van Veenendaal, *The theory of core–level line shapes beyond the impurity limit*. PhD thesis, Rijksuniversiteit Groningen, 1994.

[144] J. Zaanen, G. A. Sawatzky, and J. W. Allen, "Band gaps and electronic structure of transition–metal compounds," *Physical Review Letters*, vol. 55, pp. 418–421, 1985.

[145] T. Oguchi, K. Terakura, and A. R. Williams, "Band theory of the magnetic interaction in MnO, MnS, and NiO," *Physical Review B*, vol. 28, p. 64436452, 1983.

[146] V. I. Anisimov, J. Zaanen, and O. K. Andersen, "Band theory and Mott insulators: Hubbard U instead of Stoner I," *Physical Review B*, vol. 44, pp. 943–954, 1991.

[147] J. F. Moulder, W. F. Stickle, P. E. Sobol, and K. D. Bomben, *Handbook of X–ray Photoelectron Spectroscopy*. Perkin–Elmer Corporation, Eden Prairie, United States of America, 1992.

[148] V. R. Galakhov, S. Uhlenbrock, S. Bartkowski, A. V. Postnikov, M. Neumann, L. D. Finkelstein, E. Z. Kurmaev, A. A. Samokhvalov, and L. I. Leonyuk, "X–Ray Photoelectron 3s Spectra of Transition Metal Oxides." unpublished.

[149] J. Zaanen, C. Westra, and G. A. Sawatzky, "Determination of the electronic structure of transition–metal compounds: 2p x–ray photpelectron spectroscopy of nickel dihalides," *Physical Review B*, vol. 33, pp. 8060–8073, 1986.

[150] W. H. Press, S. A. Teukolsky, W. T. Vetterling, and B. P. Flannery, *Numerical Recipes in C: The Art of Scientific Computing*. Cambridge University Press, Cambridge, 1992.

[151] U. Korte and G. Meyer-Ehmsen, "Diffuse reflection high–energy electron diffraction," *Physical Review B*, vol. 48, pp. 8345–8355, 1993.

[152] M. R. Pederson, A. Y. Liu, T. Baruah, E. Z. Kurmaev, A. Moewes, S. Chiuzbăian, M. Neumann, C. R. Kmety, K. L. Stevenson, and D. Ederer, "Electronic structure of the molecule–based magnet $Mn[N(CN)_2]_2$ from theory and experiment," *Physical Review B*, vol. 66, pp. 014446:1–8, 2002.

[153] F. M. F. de Groot, J. C. Fuggle, B. T. Thole, and G. A. Sawatzky, "2p x–ray absorption of 3d transition–metal compounds: An atomic multiplet description including the crystal field," *Physical Review B*, vol. 42, pp. 5459–5468, 1990.

[154] A. S. Vinogradov, A. B. Preobrajenski, A. Knop-Gericke, S. L. Molodtsov, S. A. Krasnikov, S. V. Nekipelov, R. Szargan, M. Havecker, and R. Schlögl, "Observation of back–donation in 3d metal cyanide complexes through N K absorption spectra," *Journal of Electron Spectroscopy and Related Phenomena*, vol. 114–116, pp. 813–818, 2001.

[155] A. S. Chakravarty, *Introduction to the Magnetic Properties of Solids*. John Wiley & Sons, New York, 1980.

[156] M. A. Subramanian, A. P. Ramirez, and W. J. Marshall, "Structural Tuning of Ferromagnetism in a 3D Cuprate Perovskite," *Physical Review Letters*, vol. 99, pp. 1558–1561, 1999.

[157] A. H. Morrish, *The Physical Principles of Magnetism*. Robert E. Krieger Publishing Company, Inc. Huntington, New York, 1980.

[158] S. V. Vonsovskii, *Magnetism*. John Wiley & Sons, New York, 1974.

[159] P. W. Anderson, "Antiferromagnetism. Theory of Superexchange Interaction," *Physical Review*, vol. 79, pp. 350–356, 1950.

[160] P. W. Anderson, "Exchange in Insulators: Superexchange, Direct Exchange, and Double Exchange," in *Magnetism* (G. T. Rado and H. Suhl, eds.), vol. 1, ch. 3, pp. 25–85, Academic Press, New York, 1963.

[161] P. W. Anderson, "Theory of Magnetic Exchange Interactions: Exchange in Insulators and Semiconductors," in *Solid State Physics* (F. Seitz and D. Turnbull, eds.), vol. 14, pp. 99–214, Academic Press, New York, 1963.

[162] J. B. Goodenough, *Magnetism and the Chemical Bond*. Robert E. Krieger Publishing Company, Huntington, New York, 1976.

[163] A. Escuer, F. A. Mautner, N. Sanz, and R. Vicente, "Two New One–Dimensional Compounds with End–to–End Didyanamide as a Bridging Ligand: Syntheses and Structural Characterization of *trans*–$[Mn(4 - bzpy)_2(N(CN)_2)_2]_n$ and *cis*–$[Mn(Bpy)_2(N(CN)_2)_2]_n$, (4–bzpy = 4–benzoylpyridine; bpy = 2,2'–bipyrydyl," *Inorganic Chemistry*, vol. 39, pp. 1668–1673, 2000.

[164] E. Ruiz, J. Cano, S. Alvarez, and P. Alemany, "Magnetic Coupling in End–On Azido–Bridged Transition Metal Complexes: A Density Functional Study," *Journal of the American Chemical Society*, vol. 120, pp. 11122–11129, 1998.

[165] A. Escuer, R. Vicente, M. A. S. Goher, and F. A. Mautner, "Antiferromagnetic Alternating and Homogeneous Manganese–Azido Chains: Structural Characterization and magnetic Behavior of Two New One–Dimensional $[Mn(L)_2(\mu_{1,3} - N_3]_n$ Compounds (L = 3–Enthylpyridine and 2–Hydroxypyridine)," *Inorganic Chemistry*, vol. 37, pp. 782–787, 1998.

[166] M. A. S. Goher, M. A. M. Abu-Youssef, F. A. Mautner, R. Vicente, and A. Escuer, "Superexchange Interactions through Quasi–Linear End–to–End Azido Bridges: Structural and Magnetic Characterisation of a New Two–Dimensional Manganese-Azido System $[Mn(DENA)_2(N_3)_2]_n$ (DENA = diethylnicotinamide)," *European Journal of Inorganic Chemistry*, pp. 1819–1823, 2000.

[167] F. F. de Biani, E. Ruiz, J. Cano, J. J. Novoa, and S. Alvarez, "Magnetic Coupling in End–to–End–Bridged Copper and Nickel Binuclear Complexes: A Theoretical Study," *Inorganic Chemistry*, vol. 39, pp. 3221–3229, 2000.

[168] C. Kollmar and O. Kahn, "Ferromagnetic Spin Alignment in Molecular Systems: An Orbital Approach," *Accounts of Chemical Research*, vol. 26, pp. 259–265, 1993.

[169] P. J. Hay, J. C. Thibeault, and R. Hoffmann, "Orbital Interactions in Metal Dimer Complexes," *Journal of the American Chemical Society*, vol. 97, pp. 4884–4899, 1975.

[170] O. Kahn and B. Briat, "Exchange Interaction in popynuclear complexes. 1. Plrinciples, Model and Applications to binuclear complexes of chromium(III)," *Journal of the Chemical Society–Faraday Transactions II*, vol. 72, pp. 268–281, 1976.

[171] L. Noodleman, "Valence bond description of anti–ferromagnetic coupling in transition metal dimers," *Journal Chemical Physics*, vol. 74, pp. 5737–5743, 1981.

[172] J. M. Mouesca, "Quantitative harmonization of the three molecular orbital, valence bond, and broken symmetry approaches to the exchange coupling constant: Corrections and discussion," *Journal Chemical Physics*, vol. 113, pp. 10505–10511, 2000.

[173] V. A. Gubanov, A. I. Liechtenstein, and A. V. Postnikov, *Magnetism and the Electronic Structure of Crystals*. Spinger–Verlag, Berlin Heidelberg, 1992.

[174] J. Zaanen and G. A. Sawatzky, "The electronic structure and superexchange interactions in transition–metal compounds," *Canadian Journal of Physics*, vol. 65, pp. 1262–1271, 1987.

[175] J. Kanamori, "Superexchange Interaction and Symmetry Properties of Electron Orbitals," *Journal of Physics and Chemistry of Solids*, vol. 10, pp. 87–98, 1958.

[176] W. Geertsma and D. Khomskii, "Influence of side groups on 90° superexchange: A modification of the Goodenough–Kanamori–Anderson rules," *Physical Review B*, vol. 54, pp. 3011–3014, 1996.

[177] P. W. Anderson, "New Approach to the Theory of Superexchange Interactions," *Physical Review*, vol. 115, pp. 2–13, 1959.

[178] H. Weihe and H. U. Güdel, "Quantitative Interpretation of the Goodenough–Kanamori Rules: A Critical Analysis," *Inorganic Chemistry*, vol. 36, pp. 3632–3639, 1997.

[179] H. Weihe and H. U. Güdel, "Magneto–Structural Correlations in Linear and Bent Oxo–Bridged Transition–Metal Dimers: Comparisons, Interpretations, and Predictions of Ground–State Magnetic Properties," *Journal of the American Chemical Society*, vol. 120, pp. 2870–2879, 1998.

[180] R. Schenker, H. Weihe, and H. U. Güdel, "Exchange Interactions Derived from Electron Transfer Processes in $[Cr_2(OH)_3(tmtame)_2](NO_3)_3$," *Inorganic Chemistry*, vol. 38, pp. 5593–5601, 1999.

[181] H. Weihe, H. U. Güdel, and H. Toftlund, "Superexchange in Magnetic Insulators: An Interpretation of the Metal–Metal Charge Transfer Energy in the Anderson Theory," *Inorganic Chemistry*, vol. 39, pp. 1351–1362, 2000.

[182] M. Atanasov and S. Angelov, "Angular–overlap model parametrisation of Anderson's superexchange theory: I. A quantification of Goodenough–Kanamori rules," *Chemical Physics*, vol. 150, pp. 383–393, 1991.

[183] M. Atanasov, R. H. Potze, and G. A. Sawatzky, "Electronic Structure of Tetrahedral Iron(III)–Sulphur Clusters in Alkaline Thioferrates: An X–Ray Absorption Study," *Journal of Solid State Chemistry*, vol. 119, pp. 380–393, 1995.

[184] T. Schönherr, "Angular Overlap Model Applied To Transition Metal Complexes and d^N–Ions in Oxide Host Lattices," in *Electronic And Vibronic Spectra of Transition Metal Complexes II* (H. Yersin, ed.), vol. 191 of *Topics in Current Chemistry*, pp. 85–152, Springer Verlag, Berlin Heidelberg, 1997.

[185] K. Terakura, T. Oguchi, A. R. Williams, and J. Kübler, "Band theory of insulating transition–metal monoxides: Band–structure calculations," *Physical Review B*, vol. 30, pp. 4734–4747, 1984.

[186] L. Sangaletti, F. Parmigiani, and E. Ratner, "Resonant photoemission and correlated sattelites in K_2CoF_4," *Physical Review B*, vol. 57, pp. 10175—10182, 1998.

[187] O. Waldmann, J. Schülein, R. Koch, P. Müller, I. Bernt, R. W. Saalfrank, H. P. Andres, H. U. Güdel, and P. Allenspach, "Magnetic anisotropy of two cyclic hexanuclear Fe(III) clusters entrapping alkaline ions," *Inorganic Chemistry*, vol. 38, pp. 5879–5886, 1999.

[188] O. Waldmann, R. Koch, J. Schülein, P. Müller, I. Bernt, R. W. Saalfrank, F. Hampel, and E. Balthes, "Magnetic anisotropy of a cyclic octanuclear Fe(III) cluster and magneto-structural correlations in molecular ferric wheels," *Inorganic Chemistry*, vol. 40, pp. 2986–2995, 2001.

[189] R. W. Saalfrank, I. Bernt, and F. Hampel, "Template–mediated self assembly of six– and eight–membered iron coronates," *Angewandte Chemie*, vol. 36, pp. 2482–2485, 1997.

[190] R. W. Saalfrank, I. Bernt, F. Hampel, and G. B. M. Vaughan, "Ligand–to–metal ratio controlled assembly of tetra– and hexanuclear clusters towards single–molecule magnets," *Chemistry – A Europeean Journal*, vol. 7, pp. 2765–2769, 2001.

[191] K. Bärwinkel, H. J. Schmidt, and J. Schnack, "Structure and relevant dimension of the Heisenberg model and applications to spin rings," *Journal of Magnetism and Magnetic Materials*, vol. 212, pp. 240–250, 2000.

[192] K. Bärwinkel, H. J. Schmidt, and J. Schnack, "Ground–state properties of antiferromagnetic Heisenberg spin rings," *Journal of Magnetism and Magnetic Materials*, vol. 220, pp. 227–234, 2000.

[193] J. Schnack, "Properties of the first excited state of nonbipartite Heisenberg spin rings," *Physical Review B*, vol. 62, pp. 14855–14859, 2000.

[194] J. Schnack and M. Luban, "Rotational modes in molecular magnets with antiferromagnetic Heisenberg exchange," *Physical Review B*, vol. 63, p. 014418, 2001.

[195] O. Waldmann, R. Koch, S. Schromm, P. Müller, I. Bernt, and R. W. Saalfrank, "Butterfly hysteresis loop at nonzero bias field in antiferromagnetic molecular rings: Cooling by adiabatic magnetization," *Physical Review Letters*, vol. 89, p. 246401, 2002.

[196] H. Weihe and H. U. Güdel, "Angular and Distance Dependence of the Magnetic Properties of Oxo–Bridged Iron(III) Dimers," *Journal of the American Chemical Society*, vol. 119, pp. 6539–6543, 1997.

[197] V. R. Galakhov, A. I. Poteryaev, E. Z. Kurmaev, V. I. Anisimov, S. Bartkowski, M. Neumann, Z. W. Lu, B. M. Klein, and T.-R. Zhao, "Valence–band spectra and electronic structure of $CuFeO_2$," *Physical Review B*, vol. 56, pp. 4584–4591, 1997.

[198] S. G. Chiuzbaian, M. Neumann, O. Waldmann, B. Schneider, I. Bernt, and R. W. Saalfrank, "X–ray photoelectron spectroscopy of a cyclic hexanuclear cluster," *Surface Science*, vol. 482–485, pp. 1272–1277, 2001.

[199] A. C. Thompson, D. T. Attwood, E. M. Gullikson, M. R. Howells, J. B. Kortright, A. L. Robinson, and J. H. Underwood, *X–Ray Data Booklet*. Lawrence Berkeley National Laboratory, University of California, Berkeley, California, 2001.

[200] B. Schneider, *Untersuchungen zur elekronischen und geometrischen Struktur ausgwe¨hlter oxidischer und sulfidischer Materialien mittels Photoelectronen– und Röntgenspektroskopie*. PhD thesis, Universität Osnabrück, 2001.

[201] J. M. Soler, E. Artacho, J. D. Gale, A. Garcia, J. Junquera, P. Ordejon, and D. Sanchez-Portal, "The SIESTA method for ab initio order–N materials simulation," *Journal of Physics–Condensed Matter*, vol. 14, pp. 2745–2779, 2002.

[202] L. Schlapbach and A. Züttel, "Hydrogen–storage materials for mobile applications," *Nature*, vol. 414, pp. 353–358, 15 November 2001.

[203] K. H. J. Buschow, P. C. P. Bouten, and A. R. Miedema, "Hybrides of intermetallic compounds of two transition metals," *Reports on Progress in Physics*, vol. 45, pp. 937–1039, 1982.

[204] T. Sakai, M. Matsuoka, and C. Iwakura, "Rare earth intermetallics for metal-hydrogen batteries," in *Handbook on the Physics and Chemistry of Rare Earths* (J. K. A. Gschneider and L. Eyring, eds.), vol. 21, pp. 133–178, Elsevier Science B. V., Amsterdam, 1995.

[205] G. Sandrock, S. Sura, and L. Schlapbach, "Applications," in *Hydrogen in Intermetallic Compounds II* (L. Schlapbach, ed.), vol. 67 of *Topics in Applied Physics*, pp. 197–258, Springer Verlag, Berlin, 1995.

[206] C. J. Winter and J. Nitsch, eds., *Wasserstoff als Energieträger : Technik, Systeme, Wirtschaft.* Springer Verlag, Berlin, 1989.

[207] S. K. Malik, F. J. Arlinghaus, and W. E. Wallace, "Calculation of spin–polarized energy–band structure of $LaNi_5$ and $GdNi_5$," *Physical Review B*, vol. 25, pp. 6488–6491, 1982.

[208] M. Gupta, "Electronic properties of $LaNi_5$ and $LaNi_5H_7$," *Journal of Less Common Metals*, vol. 130, pp. 219–227, 1987.

[209] M. Gupta and L. Schlapbach, "Electronic properties," in *Hydrogen in Intermetallic Compounds I* (L. Schlapbach, ed.), vol. 63 of *Topics in Applied Physics*, pp. 139–217, Springer Verlag, Berlin, 1988.

[210] H. Nakamura, D. Nguyen-Manh, and D. G. Pettifor, "Electronic structure and energetics of $LaNi_5$, α–$La_2Ni_{10}H$ and β–$La_2Ni_{10}H_{14}$," *Journal of Alloys and Compounds*, vol. 281, pp. 81–91, 1998.

[211] E. Burzo and R. Lemaire, "On the magnetic behaviour of RCo_2 compounds where R is yttrium or a rare–earth," *Solid State Communications*, vol. 84, pp. 1145–1148, 1992.

[212] E. Burzo, E. Gratz, and V. Pop, "On the magnetic behaviour of ACo_2 (A = Y, Lu, Sr, Sc and Hf) compounds," *Journal of Magnetism and Magnetic Materials*, vol. 123, pp. 159–164, 1993.

[213] E. Burzo, D. Givord, and L. Chioncel, "Spin fluctuation in YCo_2–based compounds," *Journal of Applied Physics*, vol. 83, pp. 1779–1781, 1998.

[214] D. Ginoux, D. Givord, and A. del Moral, "Magnetic properties of $Gd_xY_{1-x}Ni_5$ alloys," *Solid State Communications*, vol. 19, pp. 891–894, 1976.

[215] J. Palleau and G. Chouteau, "Low Temperature Susceptibility of $LaNi_5$ hydrides.," *Journal de Physique Lettres*, vol. 41, pp. L227–L229, 1980.

[216] L. Schlapbach, "Magnetic properties of $LaNi_5$ and their variation with hydrogen absorption and desorption," *Journal of Physics F: Metal Physics*, vol. 10, pp. 2477–2490, 1980.

[217] J. C. Fuggle, F. U. Hillebrecht, R. Zeller, Z. Zolnierek, P. A. Bennett, and C. Freiburg, "Electronic structure of Ni and Pd alloys. I. X-ray photoelectron spectroscopy of the valence bands," *Physical Review B*, vol. 27, pp. 2145–2178, 1983.

[218] M. Sluiter, M. Takahashi, and Y. Kawazoe, "Theoretical study of phase stability in $LaNi_5$–$LaCo_5$ alloys," *Journal of Alloys and Compounds*, vol. 248, pp. 90–97, 1997.

[219] M. Gupta, "Electronic structure and stability of hydrides of intermetallic compounds," *International Journal of Quantum Chemistry*, vol. 293, pp. 190–201, 1999.

[220] M. Gupta, "Electronic structure of hydrogens storage materials," *International Journal of Quantum Chemistry*, vol. 77, pp. 982–990, 2000.

[221] V. Paul-Boncour, M. Gupta, J.-M. Joubert, A. Percheron-Guégan, P. Parent, and C. Laffon, "Inversigations on the electronic structure of substituted $LaNi_5$ compounds used as materials for batteries," *Journal of Materials Chemistry*, vol. 10, pp. 2741–2747, 2000.

[222] A. Szajek, M. Jurczyk, and W. Rajewski, "The electronic and electrochemical properties of $LaNi_5$, $LaNi_4Al$ and $LaNi_3AlCo$," *Journal of Alloys and Compounds*, vol. 307, pp. 290–296, 2000.

[223] A. Szajek, L. Smardz, M. Jurczyk, H. Smardz, and M. Nowak, "Electronic properties of $LaNi_5$–type alloys," *Czechoslovak Journal of Physics*, vol. 52, pp. A209–A212, 2002.

[224] K. Tatsumi, I. Tanaka, H. Inui, K. Tanaka, M. Yamaguchi, and H. Adachi, "Atomic structures and energetics of $LaNi_5$–H solid solution and hydrides," *Physical Review B*, vol. 64, p. 184105, 2001.

[225] L. Schlapbach, "XPS/UPS study of the oxidation of La and $LaNi_5$ and of the electronic structure of $LaNi_5$," *Solid State Communications*, vol. 38, pp. 117–123, 1981.

[226] F. U. Hillebrecht, J. C. Fuggle, P. A. Bennett, and Z. Zolnierek, "Electronic structure of ni and pd alloys. ii. x–ray photoelectron core–level spectra," *Physical Review B*, vol. 27, pp. 2179–2193, 1983.

[227] H. Züchner, J. Kintrup, R. Dobrileit, and I. Untiedt, "Chemical structure and bonding characteristics of metal hydrogen systems studied by the surface analytical techniques SIMS and XPS," *Journal of Alloys and Compounds*, vol. 293–295, pp. 202–212, 1999.

[228] J. H. Weaver, A. Franciosi, W. E. Wallace, and H. K. Smith, "Electronic structure and surface oxidation of $LaNi_5$, Er_6Mn_{23} and related systems," *Journal of Applied Physics*, vol. 51, pp. 5847–5851, 1983.

[229] W. E. Wallace and F. Pourarian, "Photoemission studies of $LaNi_5Cu_x$ Alloys and Relation to Hydride Formation," *Journal of Physical Chemistry*, vol. 86, pp. 4958–4961, 1982.

[230] M. H. Mendelsohn, D. M. Gruen, and A. E. Dwight, "$LaNi_{5-x}Al_x$ is a versatile alloy system for metal hydride applications," *Nature*, vol. 269, pp. 45–47, 1974.

[231] T. Takeshita, S. K. Malik, and W. E. Wallace, "Hydrogen Absorption in RNi_4Al (R = rare–earth) ternary compounds," *Journal of the Solid State Chemistry*, vol. 23, pp. 271–274, 1978.

[232] A. Percheron-Guégan, J. C. Achard, J. Sarradin, and G. Bronoël, "Electrode material based on lanthanum and nickel, electrochemical uses of such materials," *U.S. Patent 688537*, 1978.

[233] W. Zhang, J. Cimato, and A. J. Goudy, "The hydriding and dehydriding kinetics of some $LaNi_{5-x}Al_x$ alloys," *Journal of Alloys and Compounds*, vol. 201, pp. 175–179, 1993.

[234] E. Burzo, A. Chelkovski, and H. R. Kirchmayr, *Compounds between rare–earth elements and 3d, 4d and 5d elements*, vol. III/19d2 of *Landolt Börnstein Handbook*. Springer Verlag, Berlin, 1990.

[235] J. C. Achard, C. Lavetegue, A. Percheron-Guégan, A. J. Dianoux, and F. Tasset, "Hydrogen mobility in $lani_5$ hydride and its aluminum–substituted and magnanese–substituted hydrides," *Journal of Less Common Metals*, vol. 88, pp. 89–96, 1982.

[236] J. C. Achard, A. J. Dianoux, C. Lartigue, A. Percheron-Guégan, and F. Tasset in *The Rare Earth in Modern Science and Technology* (G. J. McCarthy, J. J. Rhyne, , and H. B. Silver, eds.), vol. 3, p. 481, Plenum Press, New York, 1988.

[237] M. Latroche, J.-M. Joubert, A. Percheron-Guegan, and P. H. L. Notten, "Crystal Structure of Nonstoichiometric Copper–Substituted $La(Ni_{1-z}Cu_z)_x$ Compounds Studied by Neutron and Synchrotron Anomalous Powder Diffraction," *Journal of Solid State Chemistry*, vol. 146, pp. 313–321, 1999.

[238] Y. N. Grin', Y. P. Yarmolyuk, and V. K. Pecharskij, "Composition and structure of RGa_xNi_{5-x} phases in rare earth metals – Ga – Ni Systems," *Russian Metallurgy, translated from Izvestiya Akademii Nauk SSSR, Metally*, vol. 3, pp. 187–189, 1983.

[239] B. Šorgić, A. Drasner, and Ž. Blažina, "On the structural and hydrogen sorption properties of the $GdNi_{5-x}Al_x$ system," *Journal of Alloys and Compounds*, vol. 221, pp. 169–173, 1995.

[240] B. Šorgić, A. Drasner, and Ž. Blažina, "On the structural and thermodynamic properties of the $DyNi_{5-x}Al_x$–hydrogen system," *Journal of Physics: Condensed Matter*, vol. 7, pp. 7209–7215, 1995.

[241] J.-L. Bobet, S. Pechev, B. Chevalier, and B. Darriet, "Structural and hydrogen sorption properties of $NdNi_{5-x}Al_x$ and $GdNi_{5-x}Al_x$," *Journal of Alloys and Compounds*, vol. 221, pp. 169–173, 1995.

[242] L. Bates, *Modern Magnetism*. Cambridge University Press, Cambridge, 1951.

[243] O. K. Andersen, "Linear methods in band theory," *Physical Review B*, vol. 12, pp. 8–15, 1975.

[244] O. K. Andersen and O. Jepsen, "Explicit, First–Principles Tight–Binding Theory," *Physical Review Letters*, vol. 53, p. 25712574, 1984.

[245] O. K. Andersen, O. Jepsen, and D. Glötzel in *Highlights of Condensed–Matter Theory* (F. Bassani, F. Fumi, and M. P. Tosi, eds.), North-Holland, New York, 1985.

[246] A. Kotani and H. Ogasawara, "Theory of core–level spectroscopy of rare–earth oxides," *Journal of Electron Spectroscopy and Related Phenomena*, vol. 60, pp. 257–299, 1992.

[247] B. V. Crist, *Handbook of Monochromated XPS Spectra*. XPS International, Inc., 1999.

[248] W. D. Schneider and C. Laubschat, "Binding energies and work-function changes in $Eu_xLa_{1-x}Al_2$ compounds studied by x–ray photoelectron spectroscopy," *Physical Review B*, vol. 20, pp. 4416–4422, 1979.

[249] E. Burzo, S. G. Chiuzbăian, L. Chioncel, and M. Neumann, "Magnetic and electronic properties of the $LaNi_{5-x}Cu_x$ system," *Journal of Physics: Condensed Matter*, vol. 12, pp. 5897–5904, 2000.

[250] E. Burzo, S. G. Chiuzbăian, M. Neumann, and L. Chioncel, "Magnetic and electronic properties of the $LaNi_{5-x}Al_x$ system," *Journal of Physics: Condensed Matter*, vol. 14, pp. 8057–8065, 2002.

[251] W. Pauli, "Über Gasentartung und Paramagnetism," *Zeitschrift für Physik*, vol. 41, pp. 81–102, 1927.

[252] E. C. Stoner, "Collective electron ferromagnetism," *Proceedings of the Royal Society of London Series A*, vol. 165, pp. 372–414, 1938.

[253] J. H. Van Vleck, "Models of Exchange Coupling in Ferromagnetic Media," *Reviews of Modern Physics*, vol. 25, pp. 220–227, 1953.

[254] P. W. Anderson, "Localized Magnetic States in Metals," *Physical Review*, vol. 124, pp. 41–53, 1961.

[255] J. Friedel, G. Leman, and M. Olstewski, "Metals and alloys – On nature of magnetic couplings in transition metals," *Journal of Applied Physics*, vol. 32, p. 325S, 1961.

[256] B. T. Matthias and R. M. Bozorth, "Ferromagnetism of a Zirconium–Zinc Compound," *Physical Review*, vol. 109, pp. 604–605, 1958.

[257] B. T. Matthias, A. M. Clogston, H. J. Williams, E. Corenzwit, and R. C. Sherwood, "Ferromagnetism in Solid Solutions of Scandium and Indium," *Physical Review Letters*, vol. 7, pp. 7–9, 1961.

[258] T. Moriya, *Spin Fluctuations in Itinerant Electron Magnetism*, vol. 56 of *Springer Series in Solid–State Sciences*. Springer–Verlag, Berlin Heilderberg, 1985.

[259] T. Moriya, "A Unified Picture of Magnetism," in *Metallic Magnetism* (H. Capellmann, ed.), vol. 42 of *Topics in Current Physics*, pp. 15–56, Springer–Verlag, Berlin Heilderberg, 1987.

[260] D. Gignoux and D. Schmidt, "Magnetic Properties of Intermetallic Compounds," vol. 20 of *Handbook on the physics and chemistry of rare–earths*, pp. 293–424, Elsevier, Amsterdam, 1995.

[261] E. Burzo *Private communication.*, 2001.

[262] M. T. Béal-Monod and J. M. Lawrence, "Paramagnon picture of the low–temperature susceptibility of some intermediate–valence compounds," *Physical Review B*, vol. 21, pp. 5400–5409, 1980.

[263] M. T. Béal-Monod, "Field effects in strongly enhanced paramagnets," *Physica B & C*, vol. 109–110, pp. 1837–1848, 1982.

[264] S. Misawa, "Susceptibility maximum as a Fermi–liquid effect in paramegnetic Fermi liquids," *Physica B & C*, vol. 149, pp. 162–168, 1988.

[265] A. I. Lichtenstein, M. I. Katsnelson, and G. Kotliar, "Finite–Temperature Magnetism of Transition Metals: An ab initio Dynamical Mean–Field Theory," *Physical Review Letters*, vol. 87, p. 067205, 2001.

[266] A. Georges, G. Kotliar, W. Krauth, , and M. J. Rozenberg, "Dynamical mean–field theory of strongly correlated fermion systems and the limit of infinite dimensions," *Review of Modern Physics*, vol. 68, p. 13125, 1996.

[267] R. Clauberg, W. Gudat, E. Kisker, E. Kuhlmann, and G. M. Rothberg, "Nature of the Resonant 6–eV Satellite in Ni: Photoelectron Spin–Polarization Analysis," *Physical Review Letters*, vol. 47, pp. 1314–1317, 1981.

[268] B. Sinkovic, L. H. Tjeng, N. B. Brookes, J. B. Goedkoop, R. Hesper, E. Pellegrin, F. M. F. de Groot, S. Altieri, S. L. Hulbert, E. Shekel, and G. A. Sawatzky, "Local Electronic and Magnetic Structure of Ni below and above T_C: A Spin–Resolved Circularly Polarized Resonant Photoemission Study," *Physical Review Letters*, vol. 79, pp. 3510–3513, 1997.

[269] M. Sawada, A. Kimura, and A. Kakizaki, "Helicity dependence of the spin polarization of Ni 6 eV satellite," *Journal of the Physical Society of Japan*, vol. 69, pp. 1891–1894, 2000.

Curriculum Vitae

I was borned in Vişeu de Sus, Maramureş county, Romania on March 4^{th}, 1975. In 1997 I graduated the Faculty of Physics at the Babeş–Bolyai University in Cluj–Napoca, Romania and I obtained the Diploma (Romanian: Diploma de Licenţă). One year later I also obtained a further degree at the same university (Romanian: Diploma de Studii Aprofundate). Since October 1998 I have worked in the group Photoelectron Spectroscopy advised by apl. Prof. Dr. Manfred Neumann.

List of publications

V. Simon, R. Pop, S. G. Chiuzbaian, M. Neumann, M. Coldea and S. Simon, Structural changes induced by Fe_2O_3 addition to $4Bi_2O_3 \cdot PbO$ glass matrix, *Materials Letters* **57** 2044–2048 (2003)

E. Burzo, S. G. Chiuzbăian, M. Neumann, M. Valeanu, L. Chioncel, and I. Creanga, Magnetic and Electronic Properties of $DyNi_{5-x}Al_x$ Compounds, *Journal of Applied Physics* **92** 7362–7368 (2002)

G. Cerbanic, I. Burda, S. G. Chiuzbaian, M. Neumann and S. Simon, Carriers lifetime distribution in CdSe epitaxial layers impurified with iodine and chlorine investigated by photoconductive frequency resolved spectroscopy, *Modern Physics Letters B* **16** 807–814 (2002)

E. Burzo, S. G. Chiuzbăian, M. Neumann and L. Chioncel, Magnetic and electronic properties of the $LaCu_{5-x}Al_x$ system, *Journal of Physics: Condensed Matter* **242** 8057–8065 (2002)

M. R. Pederson, A. Y. Liu, Tunna Baruah, E. Z. Kurmaev, A. Moewes, S. Chiuzbăian, M. Neumann, C. R. Kmety, K. L. Stevenson and D. Ederer, Electronic structure of the molecule–based magnet $Mn[N(CN)_2]_2$ from theory and experiment, *Physical Review B* **66** 014446 (2002)

I. R. Shein, A. L. Ivanovskii, E. Z. Kurmaev, A. Moewes, S. Chiuzbaian, L. D. Finkelstein, M. Neumann, R. A. Ren, G. C. Che, Effect of Co doping on the electronic structure of $MgCNi_3$, *Physical Review B* **66** 024520 (2002)

E. Z. Kurmaev, A. Moewes, S. G. Chiuzbaian, L. D. Finkelstein, M. Neumann, S. S. Turner and P. Day, Valence-band spectra of BEDT–TTF and TTF–based magnetic charge-transfer salts, *Physical Review B* **65** 235106 (2002)

M. Coldea, V. Pop, M. Neumann, S. G. Chiuzbaian and D. Todoran, X–ray photoelectron spectroscopy and magnetism of $GdNi_3Al_{16}$, *Journal of Magnetism and Magnetic Materials* **242** 864–866 (2002)

A. Ślebarski, A. Wrona, T. Zawada, A. Jezierski, A. Zygmunt, K. Szot, S. Chiuzbaian and M. Neumann, Electronic structure of some Heusler alloys based on aluminum and tin, *Physical Review B* **65** 144430 (2002)

V. Simon, R. Pop, M. Neumann, S. G. Chiuzbaian, M. Coldea and S. Simon, Iron oxidation states and distribution in the $4Bi_2O_3 \cdot PbO$ glass matrix, *Modern Physics Letters B* **16** 41–46 (2002)

V. Pop, M. Coldea, M. Neumann, S. Chiuzbaian and D. Todoran, X–ray photoelectron spectroscopy and magnetism of Gd_3Ni_8Al, *Journal of Alloys and Compounds* **333** 1–3 (2002)

S. G. Chiuzbaian, M. Neumann, O. Waldmann, B. Schneider, I. Bernt and R. W. Saalfrank, X–ray photoelectron spectroscopy of a cyclic hexanuclear cluster, *Surface Science* **482–485** 1272–1277 (2001)

V. Simon, S. G. Chiuzbăian, M. Neumann, D. Eniu, E. Indrea, A. Török–Kiss and S. Simon, Photoelectron spectroscopy on iron containing $CaO-SiO_2-P_2O_5$ glass ceramics, *Modern Physics Letters B* **14** 767–772 (2000)

L. Chioncel, E. Burzo and S. G. Chiuzbaian, Induced transition metal moments in rare–earth compounds, *Bulgarian Journal of Physics* **27** 1–12 (2000)

M. Coldea, S. G. Chiuzbaian, M. Neumann, D. Todoran, M. Demeter, R. Tetean and V. Pop, Magnetic and Electronic Properties of $GdNi_{5-x}Al_x$ Intermetallic Compounds, *Acta Physica Polonica A* **98** 629–632 (2000)

A. Ślebarski, M B. Maple, E. J. Freeman, C. Sirvent, D. Tworuszka, M. Orzechowska, A. Wrona, A. Jezierski, S. Chiuzbaian and M. Neumann, Weak ferromagnetism induced by atomic disorder in Fe_2TiSn, *Physical Review B* **62** 3296–3299 (2000)

E. Burzo, S. G. Chiuzbăian, L. Chioncel and M. Neumann, Magnetic and electronic properties of $LaNi_{5-x}Cu_x$ system, *Journal of Physics: Condensed Matter* **12** 5897–5904 (2000)